EPI International Journal of Engineering
Editorial Board

Foreword

Our sincere gratitude for the successful publication of the EPI International Journal of Engineering (EPI-IJE) Volume 5 Number 2 August 2022. Following the previous edition, in this last edition in 2022 also only consists of 10 (ten) manuscripts. We are glad that 3 (three) out of these 10 (ten) manuscripts are contributed by foreign authors.

The first manuscript applied Javascript code to detect the similarity of student web programming assignments. The next manuscript evaluated the urban eco-drainage system in the Makassar area. It is followed by a manuscript that studied the adaptive vibration control of smart structures using deep reinforcement learning. The fourth manuscript is also about vibration which developed a vibration measurement system using a microcontroller.

The fifth manuscript investigated the effect of spot welding parameters for dissimilar materials which are mild steel and galvanized steel. The next manuscript developed an energy-saving driving concept for a flexible manipulator by utilizing fiber composite material. The seventh manuscript also developed a system to facilitate the students' presence by using QR codes based on the Android application. The last 3 (two) manuscripts studied the effect of Mg and Zn composition on surface characteristics and flexural strength by powder metallurgy method, the effect of normalizing treatment and galvanic pack carburizing process on mechanical properties of low carbon steel and the last research about the export potential of mining commodities of indonesia.

We are grateful to all authors and reviewers for their contribution to this edition. Our sincere appreciation also to all other people and parties for their ongoing support for the EPI journal publication. We always hope the published manuscripts will have a positive contribution to the future development of science and technology.

Warm regards,

Dr. Faisal Mahmuddin
Editor-in-Chief of EPI-IJE

TABLE OF CONTENTS

Application of JavaScript Code Similarity Detection for Assessment of Web Programming Assignment 81-85

Muhammad Niswar (Universitas Hasanuddin, Indonesia)

The Evaluation of Urban Eco Drainage System in Makassar……………………………..86-91

Andi Subhan Mustari (Universitas Hasanuddin, Indonesia)
Riswal Karamma (Universitas Hasanuddin, Indonesia)
Evi Aprianti (Universitas Hasanuddin, Indonesia)

Adaptive Vibration Control of Smart Structure using Deep Reinforcement Learning 92-97

Shinya Honda (Hokkaido University, Japan)
Yuta Imura (Hokkaido University, Japan)
Katsuhiko Sasaki (Hokkaido University, Japan)
Ryo Takeda (Hokkaido University, Japan)

Development of Vibration Measurement System using a Microcontroller 98-103

Koji Sekine (Kushiro College, Japan)
Keigo Hayakawa (Kushiro College, Japan)

The Effect of Spot Welding Parameters for Dissmilar Material Mild Steel and Galvanized Steel on Nugget Size and Mechanical Strength 104-109

La Ode Al Muslim (Hasanuddin University, Indonesia)
Ahmad Yusran Aminy (Hasanuddin University, Indonesia)
Azwar Hayat (Hasanuddin University, Indonesia)

Energy-Saving Driving for a Flexible Manipulator by Utilizing Micro Fiber Composite 110-116

Akira Abe (National Institute of Technology, Asahikawa College)

Development of a Presence System for Students using QR Code based on Android Application 117-122

Mar'atuttahirah (Institut Teknologi B.J. Habibie, Indonesia)
Mardhiyyah Rafrin (Institut Teknologi B.J. Habibie, Indonesia)
Mahdaniar (Universitas Negeri Makassar, Indonesia)
Putri Ayu Maharani (Institut Teknologi B.J. Habibie, Indonesia)

Effect of Mg and Zn Composition Variations on Surface Characteristics and Flexural Strength of Biodegradable Mg-Zn-Ca Alloys by Powder Metallurgy Method 123-127

Yuliana Simon (Hasanuddin University, Indonesia)
Onny S. Sutresman (Hasanuddin University, Indonesia)
Hairul Arysad (Hasanuddin University, Indonesia)

Application of JavaScript Code Similarity Detection for Assessment of Web Programming Assignment

Muhammad Niswar[a,*]

[a]Department of Informatics, Faculty of Engineering, Universitas Hasanuddin. Email: niswar@unhas.ac.id

Abstract

Students tend to copy programming assignments from their classmates in programming courses. Students copy codes in various ways, such as changing variable names and code structure order. Lecturers spend much time checking programming assignments, especially when the number of students enrolled in the course is large. They must check whether students have completed their programming assignments individually or copied their classmates' assignments. We developed a JavaScript code similarity detection application for web programming coursework using lexical analysis and Jero Winkler's Algorithm. Our application can detect the level of the students' programming assignment similarity and assist the lecturer in deciding on plagiarism.

Keywords: Similarity detection; javascript; tokenizer; Jaro-Winkler algorithm; web programming

1. Introduction

Lecturers spend much time checking the students' programming assignments for programming courses, especially if the number of students enrolled in the class is large. They must check whether students have completed their programming assignments independently or copied their classmates' assignments. Students burdened with many tasks from other courses usually tend to copy and modify the source code of their classmates so that plagiarism is not detected. Moreover, the nature of many computer science assignments is that there is an ideal solution for each question; consequently, the best answers will be highly similar [1]. To reduce student cheating in programming courses, the author in [2] proposed to change the grading policy by reducing the weight of the assessment of the programming assignment and increasing the weight of the quiz assessment. This solution may burden the lecturers with other assessments, such as quizzes and presentations, to determine whether students do their programming assignments individually.

Generally, students modify the source code by changing the lexical and the code structure. There has been some research on attempts to detect programming code similarities to assist lecturers in checking programming assignments. Reference [3] proposed a tool called CODESIGHT to detect the similarity of programming source code using modified Greedy String Tiling algorithms. The CODESIGHT analyzes a source code collection and identifies the fragments' similarities at the lexical and syntactic levels. Reference [4] proposed similarity detection using the Karp-Rabin Greedy-String-Tiling algorithm and the Winnowing algorithm for Java source code. The proposed method can detect the similarity when various lexical or structural modifications are applied to plagiarized source code. Reference [5] proposed a cross-language source similarity detection (CLCSD) based on a code flowchart and compared it with the standardized code flowchart (SCFC).

Reference [6] proposes a similarity detection technique that uses richer structural information than normal while maintaining a reasonable execution time. The technique generates the syntax trees of program code files, extracts directly connected n-gram structure tokens from them, and performs the subsequent comparisons using an algorithm from information retrieval, cosine correlation in the vector space model. Reference [7] discusses a system designed to test the independence of source codes submitted by students participating in programming competitions. It highlights the challenges in programming education and the benefits of systematic programming and competition participation. The article also addresses the issue of plagiarism and suggests an algorithm utilizing the Levenshtein edit distance and similarity to detect plagiarized code.

Reference [8] presents a method for detecting similarities in language independent source code using standard Unix filter. Reference [9] introduces an approach to identify plagiarism by analyzing the sequence of code submission made by a single student. References [10] examines several name matching techniques and provides a comparative analysis of their effectiveness. Reference [11] introduces Deckard, a tree-based approach for detecting code clones.

*Corresponding author. Tel.: +62-852-5642-8572
Jalan Poros Malino km. 6, Bontomarannu, Gowa
Sulawesi Selatan, Indonesia

Reference [12] presents a novel approach called WASTK (Weighted Abstract Syntax Tree Kernel for detecting source code plagiarism in compter science education. The approach involves converting source code into abstract syntax trees and calculating the tree kernel to determine similarity between two abstract syntax trees. Reference [13]focuses on identifying code fragments that exhibit similar API usage patterns, which can indicate potential code clones. The authors propose an efficient technique that leverages API call sequences to detect such clones without relying on detailed syntax or semantics of the code.

In this research, we developed an application to detect the similarity of JavaScript code to determine plagiarism. JavaScript is a programming language used in building web applications. Initially, Javascript was intended to build front-end applications, but now JavaScript is also used to build back-end applications, i.e., node.js. We use the JavaScript programming language to teach internet and web programming courses. In this course, we give students a programming assignment that takes much time to review to ensure that the students completed the programming assignment correctly and individually. Therefore, we developed an application to assist the lecturers in detecting the similarity of students' programming assignments.

2. Methods

We developed an application that allows students to conduct unit testing of their programming assignment before submission, and the lecturer can detect ad classify the similarity of students' Javascript programming assignments using the Jaro-Winkler algorithm. Our proposed solution uses the ESPRIMA [14] library for lexical analysis (tokenizing) and the Jaro Winkler Algorithm to check the level of similarity. Generally, programming tasks have ideal solutions so that the solutions for student programming tasks have high similarity. Therefore, we assume the student has committed plagiarism when the similarity is more than 90%. This application aims to assist lecturers in evaluating students' programming assignments.

The workflow of this application consists of four stages, as shown in Fig. 1. First, the application retrieves student assignments from the database. Each student's assignment is compared with one another.
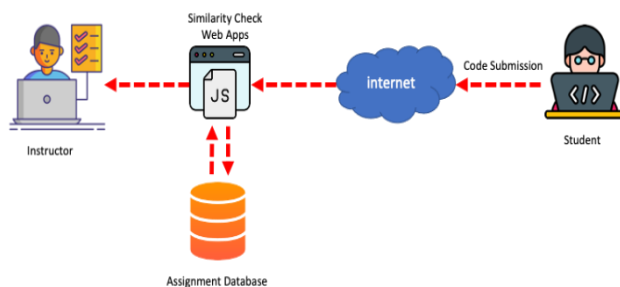

Figure 1. Code similarity check application

The application carries out a lexical analysis using the ESPRIMA method. Then it compares the results of ESPRIMA with the Jaro-Winkler algorithm and, finally, groups the data by the system. Lexical analysis and similarity detection algorithm will be explained as follows:

2.1. Lexical analysis (Tokenizer)

Lexical analysis also referred to as tokenization, transforms a series of characters, such as programming code or web pages, into a series of tokens. Tokens are strings that are identified and carry specific meanings within the context. We use ESPRIMA, a tool used to perform syntactic analysis and lexical analysis in JavaScript programs. The main function of ESPRIMA is to parse the Javascript program code. ESPRIMA will take a string value that contains a valid JavaScript program, and then from the program, and code will be made a syntax tree (syntax tree), an orderly tree that describes the syntactic structure of the program. From the results of this decomposition, the resulting syntax tree can be used for various purposes, ranging from program transformation to static program analysis.

2.2. Similarity detection algorithm

In our application, we used the Jaro-Winkler algorithm to detect the similarity of source codes. According to [9], the Jaro-Winkler algorithm performs better than other algorithms in personal name matching. Jaro-Winkler distance is an extension of the Jaro distance metric, an algorithm to measure the similarity between two strings. Usually, this algorithm is used in duplicate detection. It measures the similarity between two strings by considering both the number of matching characters and the positions of those characters. It provides a score between 0 and 1, where 0 indicates no similarity and 1 indicates an exact match. The Jaro-Winkler distance algorithm has a time complexity of quadratic runtime complexity, which is very effective on short strings and can work faster than the edit distance algorithm.

The Jaro-Winkler algorithm uses several formulas to calculate the similarity score between two strings. First, Jaro-Similarity score is calculated between two strings, s1 and s2. It calculates the length of the strings s1 and s2 and then finds the number of matching characters in the two strings being compared. It also calculates the number of transpositions, i.e., the number of adjacent characters that are out of order or swapped between two compared strings. Jaro's algorithm defines matching character as a character in both strings that are the same and characters are no exceeds the value of the following equation:

$$\left\lfloor \frac{max(|s_1|,|s_2|)}{2} \right\rfloor - 1 \tag{1}$$

Jaro's Algorithm calculate the similarity score using the following equation:

$$d_j = \frac{1}{3} \times \frac{m}{|s_1|} + \frac{m}{|s_2|} + \frac{m-t}{m} \qquad (2)$$

where,

m = the matching characters of the two strings being compared

s_1 = string length 1

s_2 = string length 2

t = number of transposition

d_j = Jaro distance score between string 1 and string 2

Jaro-Winkler distance uses a prefix scale (p) which gives a higher level of assessment, and a prefix length (l) which states the length of the prefix, which is the length of the same character from the string being compared until an inequality is found. If the strings s1 and s2 are compared, then the Jaro-Winkler distance (d_w) is:

$$d_w = d_j + \left(lp(1 - d_j) \right) \qquad (3)$$

where,

d_j = Jaro distance for strings s_1 and s_2

l = the length of the common prefix at the beginning of the string, the maximum value is four characters (the length of the same character before the inequality is found, max 4)

p = constant scaling factor. The standard value for this constant, according to Winkler, is p = 0.1

d_w = Jaro Winkler Distance score

For instance, let's compare two strings "HELLO" and "HLELO" using the Jaro-Winkler algorithm.

- Number of matching characters = 4 ("H","L","L", and "O")
- Number of transpositions = 1 ("E" and "L").
- Length of string1 = 5 and string2 = 5

So, we can calculate the Jaro similarity score = (4/5 + 4/5 + (4 - 1)/2) / 3 = 0.867. Then we can obtain the Jaro distance = 1 – 0.867 = 0.133. After that, it calculates the prefix scale factor by counting the number of matching characters at the beginning of the strings until a specified prefix length. The default prefix length in the Jaro-Winkler algorithm is 4. Here, the matching characters at the beginning are "H" and "L". Prefix scale factor. (p) = 0.1 * (number of matching characters at the beginning) = 0.1 * 2 = 0.2. Now, we can calculate the Jaro-winkler similarity score = 0.867 + (1 - 0.133) * 0.2 = 0.926. Therefore, the Jaro-Winkler similarity score between "HELLO" and "HLELO" is 0.926. This score indicates a relatively high similarity between the two strings, despite the transposition of the "E" and "L" characters.

2.3. Web application for similarity detection

We developed a web application for similarity detection using Hackathon Starter Pack Framework [15] to help instructor to assess the students' web programming assignments. It provides a basic foundation and structure for building web applications using JavaScript as the programming language. The Hackathon Starter Pack

Framework is built using JavaScript frameworks and libraries such as Node.js, Express.js, and MongoDB. It includes pre-configured settings, file structures, and example code to help developers kickstart their projects without having to set up everything from scratch.

Algorithm 1 and 2 show the pseudocode of calculating Jaro and Jaro-Winkler Similarity score, respectively. We implemented the Jaro and Jaro-Winkler algorithms into JavaScript code. Algorithms 3 shows the pseudocode of similarity check function. In this implementation, the *similarity_check* function takes an array of student objects as input. It iterates over the students and compares the exercises' code using the Jaro-Winkler algorithm. The result is stored in the *similarTask* array, which contains objects specifying the names of the two students and their similarity scores.

ALGORITHM 1 : JARO DISTANCE
1 BEGIN PROCEDURE JARO DISTANCE (STR1, STR2)
2 IF STR1 = STR2 THEN
3 OUTPUT1
4 ENDIF
5 LEN1 ← LEN(STR1)
6 LEN2 ← LEN(STR2)
7 IF LEN1=0 OR LEN2=0 THEN
8 OUTPUT0
9 ENDIF
10 max_dist ← floor(max(len1,len2) / 2) - 1
11 match ← 0
12 CREATE ARRAY HASH_STR1 HAVING SIZE = LEN(STR1)
13 CREATE ARRAY HASH_STR2 HAVING SIZE = LEN(STR1)
14 FOR I IN 0 TO LEN1
15 FOR J IN MAX(0,I-MAX_DIST) TO MIN(LEN2, I+MAX_DIST+1)
16 IF str1[I] = str2[J] and hash_str2 = 0 THEN
17 hash_str1[I] ← 1
18 hash_str2[I] ← 1
19 BREAK
20 ENDIF
21 ENDFOR
22 ENDFOR
23 IF MATCH = 0 THEN
24 OUTPUT0
25 ENDIF
26 T ← 0
27 Point ← 0
28 FOR I IN TO LEN1
29 IF HAS_STR1[I] = 1 THEN
30 WHILE(hash_str2[point] = 0)
31 POINT ← POINT + 1
32 DO
33 IF STRING1[I] !=STRING2[POINT++] THEN
34 T ← T + 1
35 ENDIF
36 T ← T/2
37 ENDIF
38 ENDFOR
39 OUTPUT ((match / len1)+(match/len2)+((match-t)/ match)) / 3
40 END PROCEDURE

ALGORITHM 2 : JARO WINKLER	
1	BEGIN PROCEDURE JAROWINKLER(STRI,STR2)
2	JARO DIST JARO_DISTANCE(STR1,STR2)
3	IF JARO_DIST> 0.7 THEN
4	PREFIX -0
5	FOR INOTO MIN(LEN(STRI), LEN(STR2))
6	IF STRING] [I] = STRING2[I] THEN
7	PREFIX - PREFIX+1
8	ELSEIF
9	BREAK
10	ENDIF
11	ENDFOR
12	PREFIX - MIN(4,PREFIX)
13	JARO_DIST - JARODIST+(0.1*PREFIX*(1-JARO_DIST))
14	ENDIF
15	OUTPUT JARO DIST
16	END PROCEDURE

ALGORITHM 3 : SIMILARITY CHECK	
1	BEGIN PROCEDURE SIMILARITY CHECK(STUDENT)
2	CREATE ARRAY SIMILARTASK
3	FORU IN 0 TO LEN(STUDENT)
4	FOR N IN (U +1) TO LEN(STUDENT)
5	ANALYZECODE1 ← TOKENIZE(STUDENTS[U].EXERCISES)
6	ANALYZECODE2 ← TOKENIZE(STUDENTS[N].EXERCISES)
7	RESULT ← JARO_WINKLER(ANALYZECODE1,ANALYZECODE2)
8	ENDFOR
9	END PROCEDURE

Determining the threshold of similarity at which two source codes are considered cheating is subjective and can vary depending on the context and specific guidelines set by the instructor. In this study, since the programming assignments have strict constraints and requirements that limit the possible solution approaches, the best answers will likely be more similar because they must adhere to the specified constraints. Therefore, we consider an acceptable similarity percentage is 90%. Anything beyond that is considered a high probability of cheating.
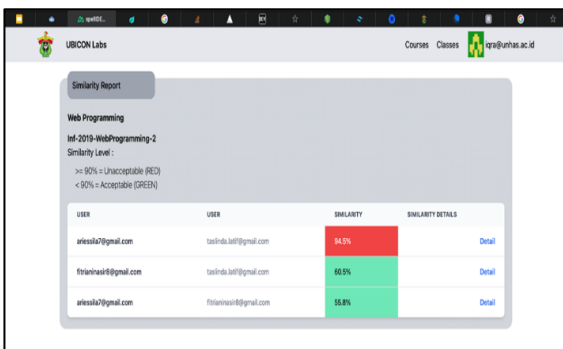

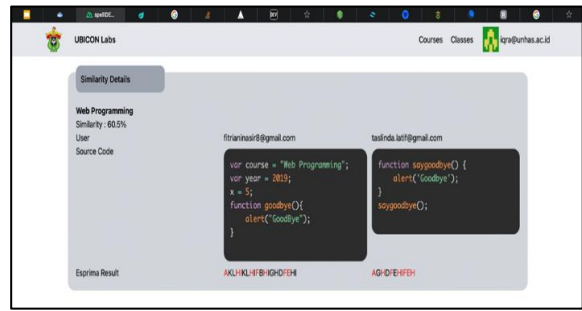Figure 2. Web interface of similarity report

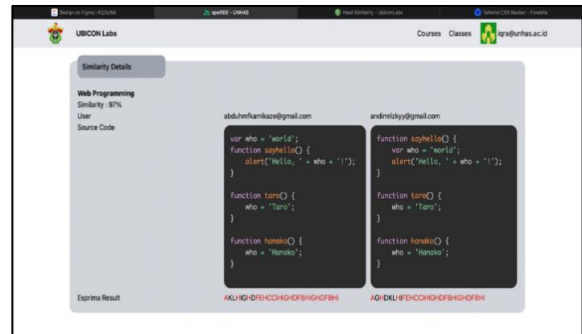Figure 3. Similarity Details with Similarity percentage of 60.5%

Figure 4. Similarity Details with Similarity percentage of 97%

3. Results and Discussion

The application has tested on JavaScript programming assignments in a web programming class in Department of Informatics, Faculty of Engineering, Hasanuddin University. Figure 2 shows a user interface display that compares student assignments with one another and presents their similarities. Lectures can see the similarity of the code by pressing the detail button, which will display the complete code of the two students' assignments, as shown in Fig. 3 and 4. Figure 3 compares two JavaScript codes of student assignments with a similarity percentage of 60.5%. On the other hand, Figure 4 compares two JavaScript codes of student assignments with a 97% similarity percentage. These two students are considered plagiarizing if the similarity is above 90%. From the experiments, typically, students change the lexical and coding structures of the source code. Students alter variable names, function names, and comments to make the code appear different from the original. They use synonyms, abbreviations, or entirely different names for identifiers. Students might change the overall structure of the code, such as reordering or restructuring functions, loops, conditionals, or statements. This helps in making the code visually distinct from the original

4. Conclusions

The issue of students copying programming assignments from their classmates is a common occurrence in programming courses. With a large number of students enrolled in the course, manually checking each programming assignment becomes time-consuming and inefficient. To address this problem, we have developed a JavaScript code similarity detection application specifically designed for web programming coursework. Our application utilizes lexical analysis using the

ESPRIMA method and Jaro-Winkler Algorithm to assess the similarity level of students' programming assignments. By analyzing factors such as variable names and code structure order, the application can provide insights into potential cases of plagiarism. The primary objective of our application is to assist lecturers in making informed decisions regarding plagiarism. It offers a more efficient and reliable approach to identify instances of code similarity, enabling lecturers to focus their attention on potential cases that require further investigation. By automating the detection process, lecturers can allocate their time and resources more effectively, ensuring fairness and maintaining the integrity of the assessment process.

References

[1] R. Fraser and D. Cheriton, "Collaboration, Collusion, and Plagiarism in Computer Science Coursework," *Informatics Educ.*, vol. 13, no. 2, pp. 179–195, 2014.

[2] J. Sukhodolsky, "How to Reduce Cheating in an Introductory Computer Programming Course?," *Int. J. Comput. Sci. Educ. Sch.*, vol. 1, no. 4, 2017.

[3] A. Bejarano, L. García, and E. Zurek, "Detection of Source Code Similitude in Academic Environments," *Comput. Appl. Eng. Educ.*, vol. 23, no. 1, pp. 13–22, 2015.

[4] Z. Đurić and D. Gasevic, "A Source Code Similarity System for Plagiarism Detection," *Comput. J.*, vol. 56, pp. 70–86, 2013.

[5] Z. Feng, L. Guofan, L. Cong, and Q. Song, "Flowchart-Based Cross-Language Source Code Similarity Detection," *Sci. Program.*, pp. 1–15, 2020.

[6] O. Karnalim and Simon, "Syntax Trees and Information Retrieval to Improve Code Similarity Detection," in *ACE20: Proceedings of the Twenty-Second Australasian Computing Education Conference*, 2020, pp. 48–55.

[7] Z. Gniazdowski and M. Boniecki, "Detection of a Source Code Plagiarism in a Student Programming Competition," *Zesz. Nauk. WWSI*, vol. 13, no. 21, pp. 74–94, 2018.

[8] J. Petrík, D. Chuda, and B. Steinmuller, "Source code plagiarism detection: The Unix way," in *2017 IEEE 15th International Symposium on Applied Machine Intelligence and Informatics (SAMI)*, 2017.

[9] N. Tahaei and D. Noelle, "Automated Plagiarism Detection for Computer Programming Exercises Based on Patterns of Resubmission," in *ICER18: Proceedings of the 2018 ACM Conference on International Computing Education Research*, 2018, pp. 178–186.

[10] P. Christen, "A Comparison of Personal Name Matching: Techniques and Practical Issues," *Jt. Comput. Sci. Tech. Reports Ser.*, 2006.

[11] L. Jiang, Z. Zhang, and Z. Su, "Deckard: Scalable and accurate tree-based detection of code clones," in *Proceedings of the 29th International Conference on Software Engineering (ICSE'07)*, 2007, pp. 96–105.

[12] D. Fu, Y. Xu, H. Yu, and B. Yang, "WASTK: An Weighted Abstract Syntax Tree Kernel Method for Source Code Plagiarism Detection," 2017.

[13] E. Kodhai and S. Kanmani, "Method-level code clone detection through LWH (Light Weight Hybrid) approach," *J. Softw. Eng. Res. Dev.*, vol. 2, no. 12, pp. 1–29, 2014.

[14] Anonim, "ESPRIMA Release Master." 2018. Accessed: Jan. 30, 2022. [Online]. Available: https://readthedocs.org/projects/esprima/downloads/pdf/latest/

[15] Sahat, "Hackathon Starter." 2022. [Online]. Available: https://github.com/sahat/hackathon-starter

The Evaluation of Urban Eco Drainage System in Makassar

Andi Subhan Mustari[a,b,*], Riswal Karamma[c], Evi Aprianti[d]

[a]Department of Civil Engineering, Faculty of Engineering, Universitas Hasanuddin, Gowa, South Sulawesi, Indonesia. Email:subhanmustari@gmail.com
[b]Engineering Professional Study Program, Faculty of Engineering, Universitas Hasanuddin, Gowa, South Sulawesi, Indonesia.
[c]Department of Civil Engineering, Faculty of Engineering, Universitas Hasanuddin, Gowa, South Sulawesi, Indonesia. Email:riswalk@unhas.ac.id
[d]Department of Transportation Engineering, Graduate School, Universitas Hasanuddin, Makassar, South Sulawesi, Indonesia. Email:eviaprianti@unhas.ac.id

Abstract

The objective of this study is to find solution to reduce runoff in low-lying areas that are prone to flooding. The concept of environmentally friendly drainage is the right choice to be applied in reducing the potential for flooding and sediment buildup, especially in areas with small water absorption. The quantitative method used to analyze hydrological and flood discharge then evaluated canal capacity in urban area. Rainfall data and population development for 10 years are used to determine the planned discharge with a certain return period according to actual conditions. The result showed that from the 4 types of primary canals, an average of 1.03 m^3/sec can be obtained. while the evaluation results for the secondary channel obtained 7 channels with a reduced average inundation discharge of 1.97 m^3/s. It can be concluded that the application of infiltration wells is quite effective to be used as an alternative solution in reducing inundation of urban area.

Keywords: Flooding effects; infiltration wells; heavy rainfall; drainage revitalization; filtration wells

1. Introduction

Sustainable development can be applied in all construction sectors without exception in the field of drainage systems. Drainage is a rainwater distribution system that has an important role in creating a healthy environment, especially in densely populated areas such as cities [1]. In the implementation of drainage management in Indonesia, it is generally still using the old or conventional paradigm which is limited to the concept of channeling excess water as quickly as possible to water bodies. The main problem that occurs is the problem of flooding because it drains excess water faster, so the opportunity for water to enter the ground is reduced [2], [3]. Therefore, the condition of infrastructure during the dry season is drought and conversely, floods occur during the rainy season. Flood disasters must be encountered by finding alternative solutions to sustainable drainage systems in urban area.

Several previous studies stated that conventional drainage systems have many drawbacks, including the occurrence of stagnant water which is no longer due to extreme natural factors, but the catchment area is decreasing caused by high population growth [4]–[7]. Newman et al., [8] found that population, landscape and drainage system is one set. Population growth will cause the increase of demand for housing and caused clogged drainage due to the improper functioning of the garbage disposal system and regular

dredging of the canals. Furthermore, Tony and Lin [9] found that a drainage system that is not integrated will make the flow accumulate in lower areas, especially sedimentation and accumulation of garbage so that the drainage channels become damaged over time. Subsequently, Amatya et al., [10] also stated that the paradigm of an environmentally sound drainage system is a good alternative, so this innovation must be developed in planning a sustainable drainage system that utilizes rainwater, stores runoff, allows water to seep, precipitates sediment and absorbs pollutants to dispose of them slowly into water bodies. Environmental drainage system is an effort to manage excess water by naturally absorbing as much water as possible into the soil or flowing it into the river without exceeding the capacity of the river [4], [11]. The simulated advanced technology by using EPA storm as One of the latest technologies for managing excess water by using infiltration wells is shown in Fig. 1.

Rainwater infiltration wells are a means of collecting rainwater and seeping into the ground, either in the form of wells, ditches, or infiltration garden plots. In addition, infiltration wells are useful to increase the volume of groundwater and efforts to overcome the effects of drought natural disasters [5], [8].

---

*Corresponding author. Tel.: +6281291043885
Jalan Poros Malino km. 6 Bontomarannu
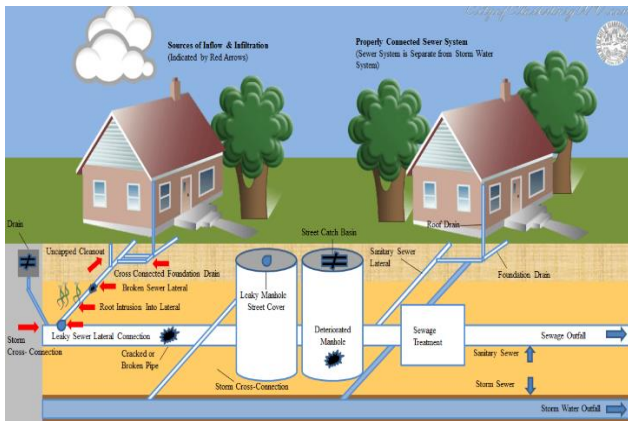*Gowa, South Sulawesi,*
Indonesia

Figure 1. The simulated the DRWH by using the EPA Storm Water Management Model (SWMM) [11]

Infiltration wells are used effectively because as flood and inundation controllers, infiltration wells can absorb abundant rainwater and are also useful for conserving groundwater and reducing the rate of erosion. Therefore, reducing the amount of surface water runoff is supposed to minimize the risk of downstream flooding and pollution to urban water bodies. Based on previous studies, infiltration wells are one of the solutions that can be implemented in Makassar as an urban area. The objective of the study is to reduce surface water runoff in low-lying areas that potentially occurred flooding in Makassar.

2. Literature Review

The amount of water on earth will always remain constant and its existence is absolute, it's just that its form can change according to the nature of water [12], [13]. The source of water flow will always flow from one high place to a lower place, water also changes from one phase to another which is also called the hydrological cycle. The hydrological cycle is very influential in drainage planning where there are various processes in changing the form of water, moves from one reservoir to another such as from river to sea or from sea to atmosphere through evaporation, condensation, precipitation, infiltration, surface runoff and subsurface flow [11]. Figure 2 shows the ideal drainage system considered.
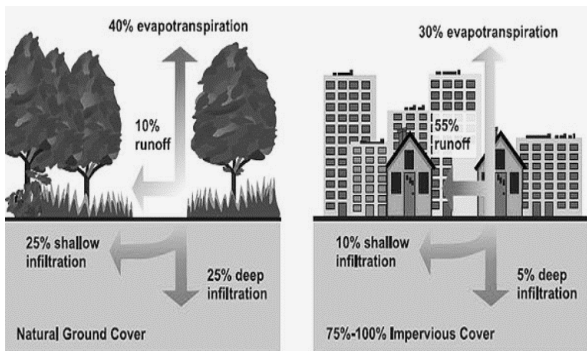
Figure 2. The difference between natural ground cover and impervious cover [14]
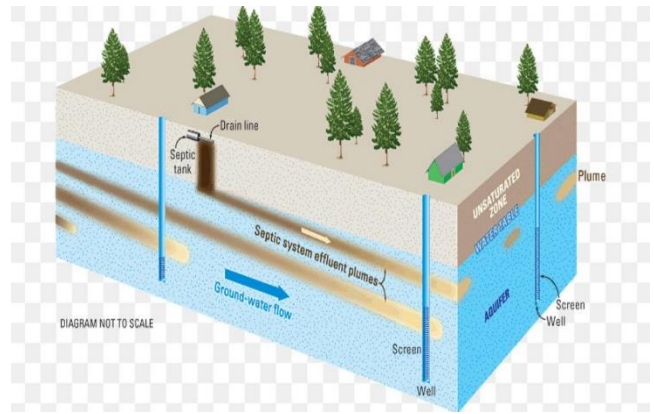
Figure 3. Infiltration wells system [15]

In the drainage system, the hydrological cycle process is very concerned to improve the drainage function as it should [14]–[16]. Ideally in a drainage system water that comes into the ground as much as possible to increase water reserves during droughts. As can be seen in Fig. 2, in the natural ground cover section water can be absorbed by the ground very well.

It can be caused in differential evapotranspiration, infiltration and surface runoff resulting from the rapid development causing the surface cover to become impermeable. There is a significant difference, therefore a hydrological analysis is needed to estimate the right method for planning the performance of a drainage system. Figure 3 shows the structure of infiltration wells in urban area. The shape and type of the infiltration well structure can be made rectangular or cylindrical with a certain depth and the bottom of the well is located above the groundwater level.

Figure 4. The Flowchart of the study

3. Research Methodology

The research location is in Panakukang District, Makassar City, South Sulawesi Province. Administratively, Makassar City has an area of approximately 175.77 km^2 consisting of 15 sub-districts and 153 sub-districts. Based on the geographical location, Makassar City is located at 5º8'6'19" South Latitude and 119º24'1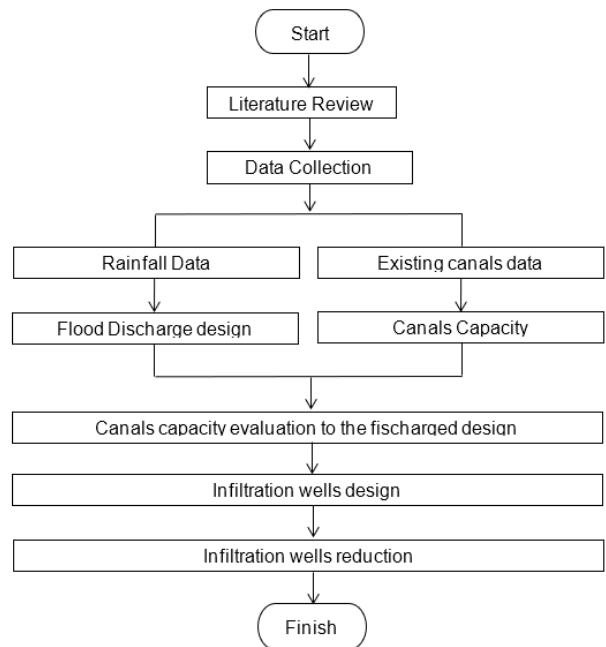738" East Longitude. Data collection is done by collecting secondary data from existing data providers. The data sources used are rainfall data for twenty years starting from 2010 to 2019 and existing canals data in Panakukang District. The flow chart of the study can be seen in Fig. 4.

4. Result and Discussion

4.1. Hydrology analysis

Rainfall is used to determine the planned discharge with a certain return period according to actual conditions. Design rainfall analysis aims to obtain the amount of design rainfall at each specified return period. The maximum planned rainfall with a certain return period can be determined by analyzing the maximum daily rainfall data. Table 1 shows the analysis of hydrology.

To determine the appropriate method, the magnitude of the statistical parameter must first be calculated. The parameters to be measured include the calculated average ($\overline{X}$), standard deviation (Sx), slope coefficient of skewness (Cs), coefficient of variation (Cv), and kurtosis coefficient (Ck). Of the several types of distribution, it is necessary to calculate and choose one type of distribution, before carrying out the calculation for selecting the type of distribution, a parameter calculation for the statistical distribution test is carried out which can be seen in Table 2.

From the results of the statistical distribution test parameters in Table 2, the appropriate type of distribution is then determined.

Table 1. The rainfall data for 20 years

No	Years	Average (mm)	No	Years	Average (mm)
1	1999	243.133	12	2010	299.333
2	2000	223.392	13	2011	242.042
3	2001	324.575	14	2012	187.250
4	2002	198.108	15	2013	276.333
5	2003	174.517	16	2014	197.433
6	2004	180.900	17	2015	232.633
7	2005	192.125	18	2016	235.342
8	2006	181.133	19	2017	276.792
9	2007	234.525	20	2018	231.192
10	2008	219.125	21	2019	215.450
11	2009	181.042			

Table 2. The Statistical parameters

NO	YEAR	X	X^2	(X1-X)	(X1-X)^3	(X1-X)^4
1	1999	243.133	59113.8	17.115	5014	85813.56
2	2000	223.392	49903.8	-2.626	-18.113	47.567
3	2001	324.575	105348	98.557	957336	94352284.5
4	2002	198.108	39246.912	-27.910	-21739.887	606749.89
5	2003	174.517	30456.1	-51.501	-136600.34	7035080.52
6	2004	180.900	32724.8	-45.118	-91842.9	4143752.991
7	2005	192.125	36912.1	-33.893	-38933.6	1319570.9
8	2006	234.525	55001.9	-44.885	-90425.3	5237.64
9	2007	219.125	48015.8	8.907	615.675	2257.8
10	2008	181.042	32776.1	-6.891	-327.490	28892334.9
11	2009	242.042	89600.4	8.507	-90980.4	65926.9
12	2010	187.250	58584.2	-8.77	-394082.3	667611.6
13	2011	276.633	35062.6	9.324	-4114.3	1915.334
14	2012	235.23	76360.1	6.615	-58266.03	7557.420
15	2013	276.333	55385.7	50.774	127381	6645979.5
16	2014	197.333	534423.45	-10.005	289.523	716.542
17	2015	232.633	65221.1	7.823	-23355.700	12472.334
18	2016	235.192	103248	8.993	-1180.214	5324.67
19	2017	215.450	38979.2	10.342	810.520	4091953.314
20	2018	226.018	39223.1	-23.554	138.494	124733.45
	AVERAGE	226.018				160664044.4

In determining the type of distribution, it will be carried out by means of dispersion measurements. In these measurements, the distribution test factors must be known as follows:

- Standard Deviation (Sx)

$$Sx = \sqrt{\frac{\Sigma\,(Xi - X)^2}{(n-1)}} = \sqrt{\frac{34117.085}{20}} = 41.3019 \qquad (1)$$

- Coefficient of Skewness (Cs)

$$Cs = \frac{n\,.\,\Sigma\,(Xi - X)^3}{(n-1)\,.\,(n-2)\,Sx^3} = \frac{22407114}{26772965.45} = 0.837 \qquad (2)$$

- Sharpness/Kurtosis Coefficient (Ck)

$$Ck = \frac{n^2\,.\,\Sigma\,(Xi - X)^4}{(n-1)\,.\,(n-2)\,.\,(n-3)\,Sx^4} = 0.064 \qquad (3)$$

- Coefficient of Variation (Cv)

$$Cv = \frac{Sx}{Xi} = \frac{41.3019}{226.018} = 0.17 \qquad (4)$$

The result show that Cs = 0.837 and Ck = 0.064, the analysis will use the Pearson Log Distribution III, based on a comparison of distribution requirements and frequency distribution tests. Furthermore, from the results of the statistical analysis of the parameters using the Pearson Log III, it is possible to calculate the design rainfall analysis for various return periods. The results of the calculation of rainfall with the Pearson Log Type III method, are as follows:

- Average ($Log\ \bar{X}$)

$$Log\ \bar{X} = \frac{\Sigma x}{n} = \frac{49.2998}{21} = 2.3476 \qquad (5)$$

- Standard Deviation (Sx)

$$Sx = \sqrt{\frac{\Sigma\ (\ Log\ Xi - Log\ \bar{X}\ )^2}{(\ n-1\ )}} = \sqrt{\frac{0.1163}{20}} = 0.0762 \qquad (6)$$

- Coefficient Skewness (Cs)

$$Cs = \frac{n\ .\ \Sigma\ (\ Log\ Xi - Log\ \bar{X}\ )^3}{(\ n-1\ ).(\ n-2\ )Sx^3} = \frac{22407114}{26772965.45} = 0.4984 \qquad (7)$$

Furthermore, the results of the statistical parameter analysis using the Pearson Log III, can be calculated from the design rainfall analysis for various return periods can be seen in Table 3.

4.2. Flood discharged analysis

In the calculation of rainwater discharge, the rational method is used. The magnitude of the runoff coefficient (C) is influenced by the topography of the land. The C value is taken from the average runoff coefficient value of each land use designation in Panakukang District.

- catchment area, A = 0.19 km^2
- runoff coefficient, C = 0.81 with length of canals, L = 2951.81 m
- Slope, S = 0.00023
- Flow velocity in the channel, v = 0.98 m/s
- Surface flow time,
  - t_o = 0.0195 $L_o^{0.77}$ $S^{-0.385}$
  -     = 0.0195 $67.37^{0.77}$ $0.00023^{-0.385}$
  -     = 12.47 minute
- Stream time in the channel,
  - t_s = L / v x 60
  -     = 2951.81 / 0.98 x 60
  -     = 50.20 minute
- Concentration time,
  - t_c = t_o + t_s
  -     = 12.47 +   50.20
- Design rain intensity, I = 202.3 mm/hrs
- Rainwater Runoff Debit (Q_1)
  - = 0.2778 x C x I x A
  - = 0.2778 x 0.81 x 202.38 x 0.19 = 8.67 m^3/s

Table 3. The rainfall design

T (Period)	k	$Log\ \bar{X}$	Sx	Rainfall design (mm)
2	-0.083	2.3476	0.0762	219.43
5	0.808	2.3476	0.0762	256.58
10	1.323	2.3476	0.0762	280.86
15	1.714	2.3476	0.0762	300.86
25	1.910	2.3476	0.0762	311.32
50	2.310	2.3476	0.0762	334.01
100	2.685	2.3476	0.0762	356.72

- Average Domestic Effluent Debit (Q_2)
  - = 0.00000139 x Pn
    - ➔ with Total population (Pn) = 317.68 ppl
  - = 0.000442 m^3/s

Design flood discharge (Q_{design}) is rainwater discharge (Q_1) plus domestic discharge water discharge (Q_2), where the Rain Return Period (PUH) used is 5 years for secondary drainage channels and Rain Return Period (PUH) 10 years for drainage channels that can be seen in Figs. 5 and 6. The following is an example of design discharge analysis on the Urip Sumohardjo 1 Primary Canal (SP. US1):

Q_{design} = Q1 + Q2 = 8.67 + 0.000442 = 8.67 m^3/second

Downspouts and gutter systems are a structure's first defense against over-saturation from stormwater. They are often drained into an aluminum extension, buried drainpipe, rain barrel, or other solution. The evaluation of the capacity of the drainage channel is to analyze the capacity of the existing drainage channel to accommodate the design flood. If the channel is unable to accommodate the design flood discharge, inundation will occur due to excess runoff.
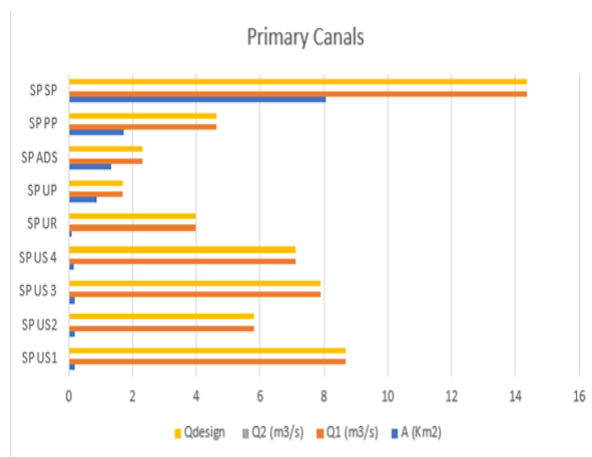

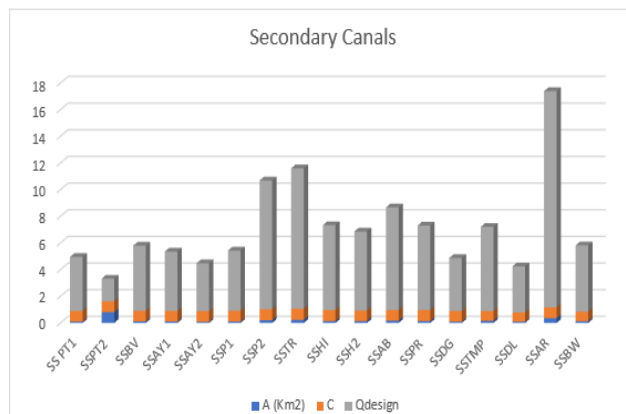Figure 5. The Flood discharge design for primary canals

Figure 6. The Flood discharge design for secondary canals

The inundation that occurs is the difference between the design flood discharge (Qranc) and the channel capacity (Qsal). Table 4 shows the comparison of Q_{design} and Q_{canals}. A drainage system consists of piping that conveys sewage, rainwater, or other liquid waste to a point of disposal, either in the sewer system or septic tank. Its main objective is to collect and remove wastewater and keep sewer gases out of the building.

It can be said that there are several canals is not fulfilling the requirements. Therefore, infiltration wells are planned in several locations that experience inundation, where the Q_{canals} does not meet the Q_{design}. The volume of the infiltration well can be calculated using the cylinder volume formula.

$$V = 1/4 \, \pi \, d^2 \, x \, h \qquad (8)$$

where, V = Infiltration well volume; d = Diameter of the infiltration well; h = depth of infiltration well. The amount of reduction that can be carried out by infiltration wells is shown in Table 5.

From Table 5, infiltration wells are quite effective as an alternative solution in reducing inundation that occurs in Panakukang District. These findings are in line with the statement from previous research that said that soakaways & infiltration wells provide stormwater attenuation and thus groundwater recharge. The main benefit is that it offers minimal net land take with a good volume reduction and peak flow attenuation. Easy to build and operate, they can be grouped and linked together to drain large areas including highways [10], [15], [16]. An accurate estimate of infiltration rate is crucial in hydrology, agricultural and civil engineering, irrigation design, and soil and water conservation. Infiltration is the vector for solutes into the soil profile and is a determining factor for their concentration in the runoff.

Table 5. The amount of reduction of inundation in Makassar

Code of Canals	Q_{design}	Qcanals	Vinfiltration	Reduction of Inundation
PRIMARY CANALS				
SP.US1	8.68	6.21	2.36	-0.11
SP.US3	7.91	6.77	2.36	1.22
SP.US4	7.12	5.38	2.36	0.61
SP.UR	3.99	2.89	2.36	1.27
SECONDARY CANALS				
SS.PTY1	4.04	2.47	2.36	0.80
SS.P1	4.51	4.17	2.36	2.02
SS.P2	9.66	9.31	2.36	2.01
SS.TR	10.54	10.40	2.36	2.22
SS.DL	3.45	3.24	2.36	2.15
SS.AR	16.22	16.11	2.36	2.25
SS.BW	4.97	4.86	2.36	2.25

5. Conclusion

The term "flood" refers to any episode entailing the overflowing of water or flowing of water in areas usually not submerged. In urban areas, two main phenomena are generally related to the occurrence of flooding: the overflow of watercourses (fluvial or overbank flooding) and the generation of stormwater during precipitation events (flash flooding). The result showed that from the 4 types of primary canals, an average of 1.03 m^3/sec can be obtained. while the evaluation results for the secondary channel obtained 7 channels with a reduced average inundation discharge of 1.97 m^3/s. It can be concluded that from nine primary canals and 17 secondary canals that were studied, over four primary canals and seven secondary canals need to build infiltration wells due to they do not meet the requirements $Q_{canals} > Q_{design}$.

References

[1] S. Wenying, "Retain the common ground: implications of research on fringe belt and urban green infrastructure for urban landscape revitalisation, a case of Quanzhou," *Landsc. Res.*, pp. 64–87, 2022.

[2] Y. Cheng *et al.*, "Impacts of water bodies on microclimates and outdoor thermal comfort: Implications for sustainable rural revitalization," *Front. Environ. Sci.*, vol. 10, pp. 1–13, 2022.

[3] C. Bae and D. K. Lee, "Effects of low-impact development practices for flood events at the catchment scale in a highly developed urban area," *Int. J. Disaster Risk Reduct.*, vol. 44, no. 2, 2019.

[4] S. Yang *et al.*, "Feasibility of a combined solubilization and eluent drainage system to remove Cd and Cu from agricultural soil," *Sci. Total Environ.*, vol. 807, no. 2, 2022.

[5] I. B. Lourenço, L. F. Guimarães, M. B. Alves, and M. G. Miguez, "Land as a sustainable resource in city planning: The use of open spaces and drainage systems to structure environmental and urban needs," *J. Clean. Prod.*, vol. 276, 2020.

[6] D. La Rosa and V. Pappalardo, "Planning for spatial equity-A performance based approach for sustainable urban drainage systems," *Sustain. Cities Soc.*, vol. 53, 2020.

[7] Y. Andung, S. Suripin, and B. H. Setiadji, "Design of Sustainable Road Drainage System Model," *J. Sustain. Eng. Proc. Ser.*, vol. 1, no. 1, pp. 35–45, 2019.

[8] G. Newman, L. Dongying, Z. Rui, and R. Dingding, "Resilience through regeneration: The economics of repurposing vacant land with green infrastructure," *Landsc. Archit. Front.*, vol. 6, no. 6, 2019.

[9] M. A. Tony and L. S. Lin, "Iron coated-sand from acid mine drainage waste for being a catalytic oxidant towards municipal wastewater remediation," *Int. J. Environ. Res.*, vol. 15, pp. 191–201, 2021.

[10] D. M. Amatya, G. M. Chescheir, T. M. Williams, R. W. Skaggs, and S. Tian, "Long-term water table dynamics of forested wetlands: drivers and their effects on wetland hydrology in the southeastern Atlantic coastal plain," *Wetlands*, vol. 40, no. 6, 2019.

[11] A. Palla, I. Gnecco, and P. La Barbera, "The impact of domestic rainwater harvesting systems in storm water runoff mitigation at the urban block scale," *J. Environ. Manage.*, vol. 191, pp. 297–305, 2017.

[12] X. Dong, H. Guo, and S. Zeng, "Enhancing future resilience in urban drainage system: Green versus grey infrastructure," *Water Res.*, vol.

124, pp. 280–289, 2017.

[13] M. Saadat Foomani and B. Malekmohammadi, "Site selection of sustainable urban drainage systems using fuzzy logic and multi-criteria decision-making," *Water Environ. J.*, vol. 34, no. 4, pp. 584–599, 2020.

[14] C. R. Thorne, E. C. Lawson, C. Ozawa, S. L. Hamlin, and L. A. Smith, "Overcoming uncertainty and barriers to adoption of Blue-Green Infrastructure for urban flood risk management," *J. Flood Risk Manag.*, vol. 11, pp. S960--S972, 2018.

[15] I. E. de Graaf *et al.*, "A global-scale two-layer transient groundwater model: Development and application to groundwater depletion," *Adv. Water Resour.*, vol. 102, pp. 53–67, 2017.

[16] M. I. Rodríguez-Rojas, F. Huertas-Fernández, B. Moreno, G. Martínez, and A. L. Grindlay, "A study of the application of permeable pavements as a sustainable technique for the mitigation of soil sealing in cities: A case study in the south of Spain," *J. Environ. Manage.*, vol. 205, pp. 151–162, 2018.

Adaptive Vibration Control of Smart Structure Using Deep Reinforcement Learning

Shinya Honda,[a,*], Yuta Imura[b], Katsuhiko Sasaki[c], Ryo Takeda[d]

[a]Faculty of Engineering, Hokkaido University. Email: honda@eng.hokudai.ac.jp
[b]Faculty of Engineering, Hokkaido University. Email: imu0004@eis.hokudai.ac.jp
[c]Faculty of Engineering, Hokkaido University. Email: katsu@eng.hokudai.ac.jp
[d]Faculty of Engineering, Hokkaido University. Email: r.takeda@eng.hokudai.ac.jp

Abstract

In this research, the authors developed an adaptive control method using deep reinforcement learning which is a kind of machine learning to suppress the vibration of smart structures. This method just requires information about the control response and input, and does not require numerical models for the controlled object to design the controller. We experimented to verify the effectiveness of this method. In this experiment, a smart structure fabricated by an aluminum plate and a piezoelectric actuator was used as a controlled object. Three kinds of reinforcement learning algorithms are employed, Deep Q Network (DQN), Deep Deterministic Policy Gradient (DDPG), and Twin Delayed DDPG (TD3), and the control performance is compared. As a result, we succeeded in reducing the H_∞ norm of the frequency response to impulse disturbance by up to about 40 dB compared to the uncontrolled case. This demonstrates the applicability of the control method using deep reinforcement learning to adaptive vibration control.

Keywords: Adaptive control; reinforcement learning; smart structure; vibration control

1. Introduction

Vibration control of mechanical structures is an important technology to prevent unexpected behavior and damage caused by vibration. In recent years, it has become difficult to achieve the desired vibration characteristics only by structural design due to the increasing performance of mechanical structures, and the importance of active vibration control technology has increased. Therefore, various control theories, such as classical control theory and modern control theory, have been developed and used in practice. However, many of these methods have problems such as the need to model the control target precisely and the deterioration of control performance when the surrounding environment or the system to be controlled changes.

As the potential use of artificial intelligence (AI) is widely discussed in many research fields [1], control utilizing machine learning, a type of AI technology, has also been attracting attention as a new control method that solves these problems. Machine learning is an analytical technique that uses a computer to learn a large amount of data to find useful patterns in the data [2]. By utilizing this technology for vibration control, it is possible to control an unknown control target by learning, without modeling the target. In addition, continuous learning is expected to suppress the degradation of control performance due to

changes in the environment, including changes in the surrounding environment and the control target. The following are examples of research on vibration control methods using machine learning. Yang et al. performed vibration control of smart structures using multi-neural networks [3]. Honda et al. conducted adaptive vibration control using self-organizing maps [4].

In this study, we investigated vibration control using deep reinforcement learning in machine learning. Reinforcement learning is a technique in which a computer learns and acquires the optimal behavior for performing a task from experience by interacting with a dynamic environment in a trial-and-error manner [5]. In particular, deep reinforcement learning, which utilizes deep learning for conventional reinforcement learning, is characterized by its ability to handle complex problems with nonlinearities and has demonstrated performance that can beat human players in the field of games such as chess [6]. However, although there are some examples of applications of deep reinforcement learning in control, such as control of an inverted pendulum by reinforcement learning [7], [8] and parameter tuning of PID control [9], [10], there are few examples of vibration control of continuous bodies by reinforcement learning. Mu et. al. proposed flutter suppression method based on machine learning [11], and Samaitis et. al., evaluated adhesive bond quality based on machine learning and pulse-echo immersion data [12]. Therefore, to develop an adaptive vibration control method using deep reinforcement

*Corresponding author. Tel.: +81-11-706-6415
Kita-13, Nishi-8, Kita-ku
Sapporo, Hokkaido, Japan, 060-8628

learning, this study proposed and compared several vibration control methods using different reinforcement learning algorithms.

To demonstrate that the reinforcement learning methods is effective vibration control method for the smart structure with continuous body, a smart structure consisting of a thin aluminum plate and piezoelectric actuators was employed as the control target. We applied a control method using deep reinforcement learning to this structure and conducted vibration control experiments to verify the effectiveness of this method. As a result, the controller was successfully constructed by learning without using any information about the control target, thus demonstrating the applicability of the method to adaptive vibration control.

2. Controller Configuration using Deep Reinforcement Learning

2.1. Reinforcement learning overview

Reinforcement learning is a machine learning technique. In this method, a computer learns the best way to solve a problem by collecting information through interaction with its environment. A schematic diagram of reinforcement learning is shown in Fig. 1. In reinforcement learning, the subject that interacts with the environment is called an agent, which selects an action according to its own action selection rule (policy) based on the observed state of the environment (state) and acts against the environment. The agent then receives an evaluation of its action as a reward from the environment. The goal of reinforcement learning is to maximize this reward by learning and improving the strategy through interaction with the environment and to obtain the optimal strategy.
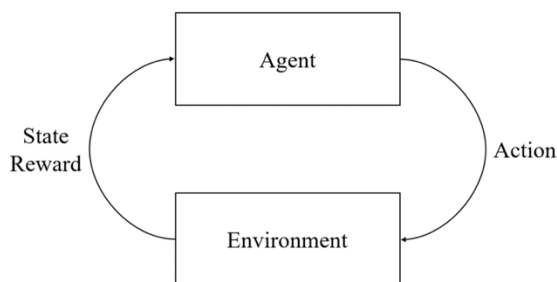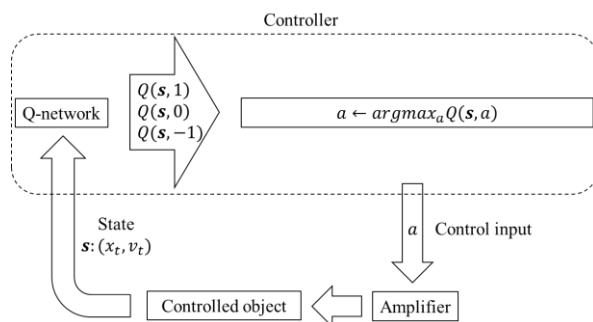

Figure 1. Diagram of reinforcement learning

Figure 2. DQN controller

By applying reinforcement learning methods to vibration control, it is possible to adjust appropriate control inputs through learning, making model-free control possible. It is also possible to construct a system that can respond to changes in the control target and environment. However, since the control system is not designed using a detailed dynamic model of the controlled object, its control performance may be inferior to that of conventional models.

The method that utilizes deep learning for reinforcement learning is called deep reinforcement learning. This method uses Deep Neural Networks (DNNs) to process information about states observed in the environment and to represent policies, and DNNs make it possible to store and update these models more efficiently. Widely used three types of deep reinforcement learning algorithms were used in this study: Deep Q Network (DQN), Deep Deterministic Policy Gradient (DDPG), and Twin Delayed DDPG (TD3).

DQN is a deep reinforcement learning algorithm developed by DeepMind, Inc. in 2013 [13]. The algorithm uses a Q-network to learn an action-value function (Q-function), which represents the value of each possible action in each state of the environment. After learning, the agent selects the action that maximizes the value of the Q-network according to the observed state and maximizes the reward. Due to the algorithm of selecting the action that maximizes the Q-function from multiple actions, the number of actions handled is finite, so the action space becomes a discrete value.

DDPG is proposed by Lillicrap et al. in 2015 [14]. This algorithm uses two networks for learning: an Actor-network, which outputs actions based on the state observed from the environment as input, and a Critic network, which evaluates the Actor-network. The agent's behavior is determined by the output of the Actor-network. Therefore, unlike DQN, the action space becomes continuous.

TD3 is an improved method of DDPG [15]. The basic method is the same as DDPG, but three additional methods called Clipped Double Q learning, Target Policy Smoothing, and Delayed Policy Update are added to stabilize the learning process.

2.2. Controller configuration with DQN

The smart structure that is the control object in this study is measured by its velocity and displacement by non-contact sensors. Since a piezoelectric actuator is attached as the control device, the control input becomes the voltage. The controller shown in Fig. 2 was configured using a Q-network for vibration control by DQN. The state s given to the Q-network is set to $s = (x_t, v_t)$ where x_t is the displacement observed by the sensor and v_t is the velocity. The action space A, which represents the set of actions that can be selected by the agent, is set to $A = \{-1, 0, 1\}$. The observed state $s = (x_t, v_t)$ and the selectable actions $a \in A$ are used as inputs to the Q-network, and the value of the Q function $Q(s, a)$ is computed for all a. Then, the value a that maximizes

$Q(\boldsymbol{s}, a)$ is input to the actuator through an amplifier as the control input voltage.

The reward r given to the agent during learning is set to $r = -|x_{t+1}| - 0.05|a_t|$ where a_t is the agent's control input and x_{t+1} is the displacement at the next time step after the control input. The constant 0.05 was determined by trial and error by numerical experiment. From the first term, the reward increases as the absolute value of x_{t+1} decreases. This means that the agent learns to select control inputs that reduce the absolute value of x_{t+1}, and as a result, vibration suppression can be expected. In addition, the second term is smaller than the first term, so energy-saving and efficient control can also be expected. When learning and updating the controller, the Q-network is learned and updated based on the DQN algorithm using the above $\boldsymbol{s}, a$, and r.

2.3. Controller configuration with DDPG and TD3

The controller shown in Fig. 3 is constructed using the Actor network for DDPG/TD3. The state $\boldsymbol{s}$ input to the network is set to $\boldsymbol{s} = (x_t, v_t)$ as in the DQN case. The controller inputs $\boldsymbol{s}$ observed from the target to the Actor network and calculates the output $\mu(\boldsymbol{s})$. In this case, $-1 < \mu(\boldsymbol{s}) < 1$ becomes continuous values. The output a from the controller is $a = \mu(\boldsymbol{s})$. This a is input to the actuator through an amplifier as the control input voltage. The reward r given to the agent during learning is defined as $r = -|x_{t+1}| - 0.05|a_t|$ as in the DQN case. The above $\boldsymbol{s}$, a, and r are used to train and update the Actor-network based on the DDPG/TD3 algorithm, and the controller is trained and updated.
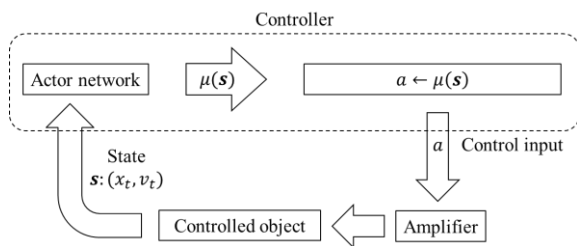

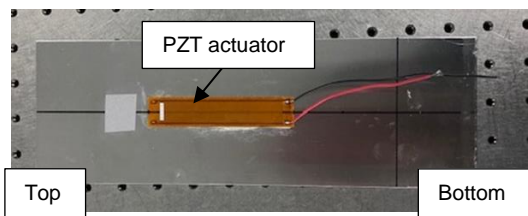
Figure 3. DDPG and TD3 controller

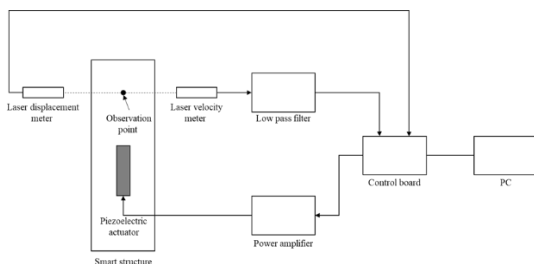Figure 4. Smart structure composed of Al plate and PZT actuator
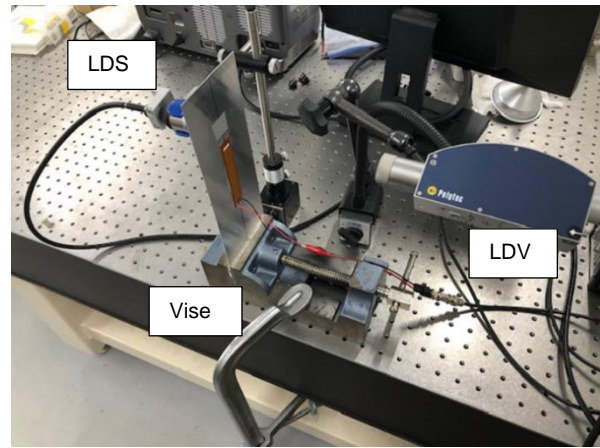

Figure 5. Diagram of the experimental system

Figure 6. Experimental set-up

3. Experiments

3.1. Experimental setup

The smart structure shown in Figure 4 was employed as the control object. In this study, we define a structure equipped with actuators that can generate control forces as a smart structure. Therefore, the structure consists of a piezoelectric actuator (PZT) attached to a flat aluminum plate. The dimensions of the aluminum plate are 300 mm long, 100 mm wide, and 1 mm thick. The piezoelectric actuator was glued to one side of the plate from 80 mm to 180 mm from the top edge on the center line. The piezoelectric actuator M8514-P1 (Smart Materia) is employed here.

A schematic diagram and picture of the experimental setup is shown in Figures 5 and 6. In this system, the smart structure is clamped by a vise attached to a vibration-isolation table up to 50 mm from the bottom edge. A laser displacement senser (LDS) and a laser doppler vibrometer (LDV) were installed in front of and behind the smart structure to observe the displacement and velocity in the thickness direction at the center of the structure at a position 60 mm from the top edge. The observed displacement and the velocity are sent to the control PC through a low-pass filter and control board. The control PC calculates the control input according to the observed displacement and velocity and sends the signal to the power amplifier through the control board. The control input voltage is amplified by the power amplifier and applied to the piezoelectric actuator for control. The sampling frequency and the frequency of the control input are set at 100 Hz.
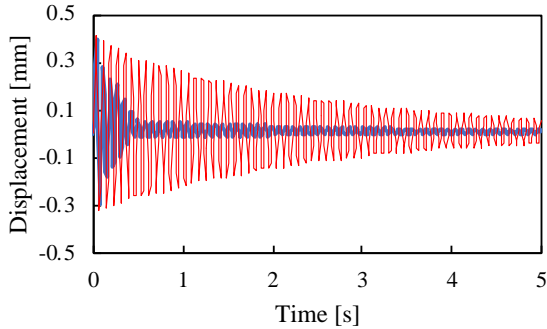
3.2 Vibration control for impulse disturbance

A voltage was applied to the piezoelectric actuator for 0.01 s (one-time step) to simulate impulse excitation and vibrate the structure. After that, vibration control was performed using a controller for 5 seconds. Next, the controller was trained and updated based on the DQN, DDPG, and TD3 algorithms using measured displacement and velocity data. Vibration control experiments were then conducted again using the updated controllers. This was repeated 100 times for one episode. After that, vibration control experiments were conducted using the controllers

that had been trained throughout the 100 episodes to verify the control performance.
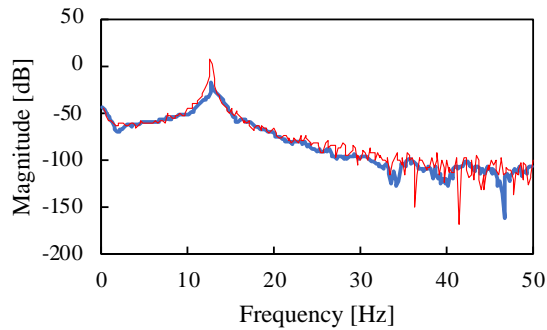
3.3 Vibration control for random disturbance

Vibration control experiments were also conducted for random disturbances to confirm the control performances under more realistic environments.

(a) Time response
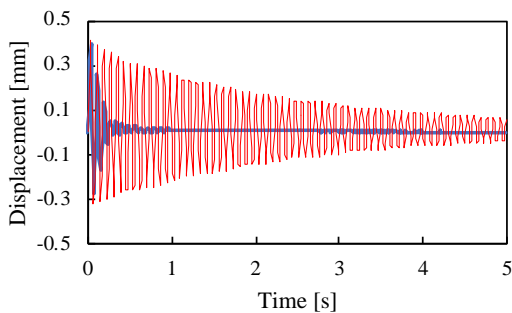

(b) Frequency response

Figure 7. Control response to impulse disturbance (DQN).

Table 1. Control result for impulse disturbance.

	Displacement [mm]	H_∞ norm [dB]
DQN	11.95	-18.67
DDPG	5.27	-35.55
TD3	5.47	-33.85
W/O control	51.02	5.41
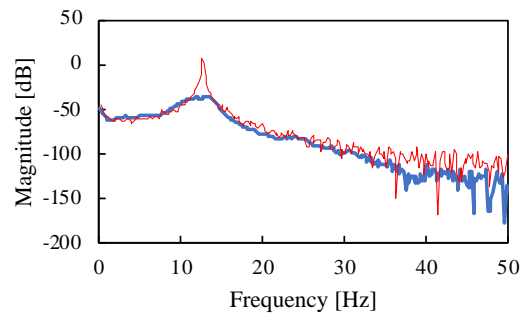
(a) Time response

(b) Frequency response

Figure 8. Control response to impulse disturbance (DDPG).
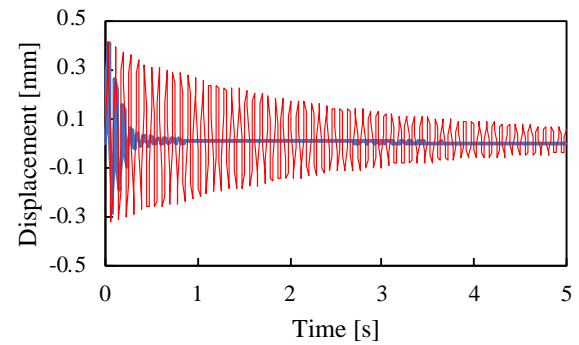
(a) Time response
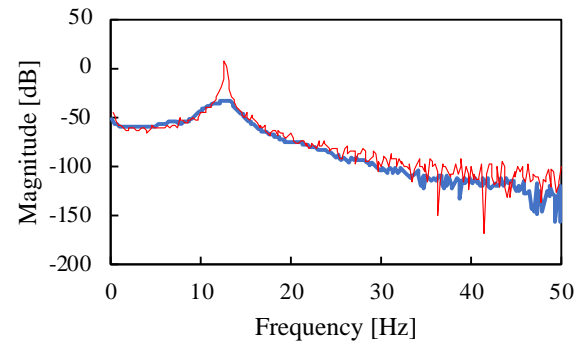
(b) Frequency response

Figure 9. Control response to impulse disturbance (TD3).

In this experiment, TD3 was used as the algorithm for control and controller training. To apply the random disturbance, a piezoelectric actuator for the disturbance was attached to the back side of the smart structure. The voltage signal following uniform random numbers was applied to the actuator for a period of 5 seconds. The controller was then trained for 100 episodes as in the vibration control experiment for impulse disturbances.
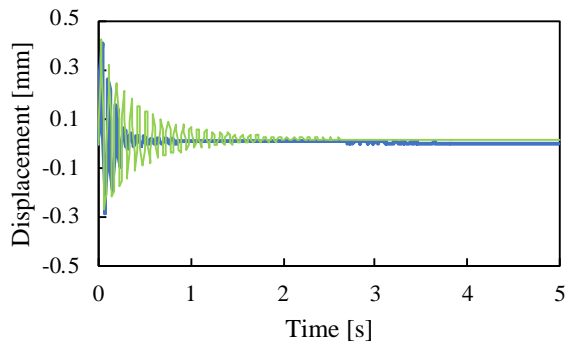
(a) Time response
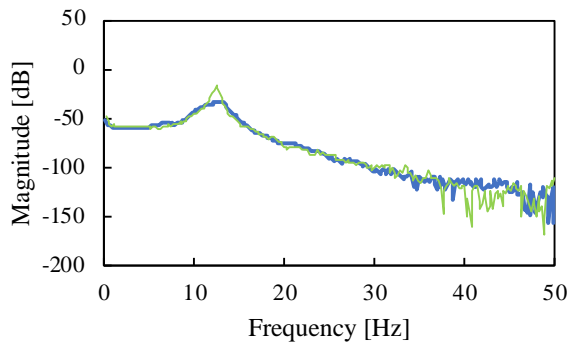
(b) Frequency response

Figure 10. Comparison of TD3 with proportional control

Table 2. Control results for random disturbance

	Displacement [mm]	H_∞ norm [dB]
TD3	13.82	-34.78
W/O control	102.91	20.34

4. Result and Discussion

4.1 Results for impulse disturbance

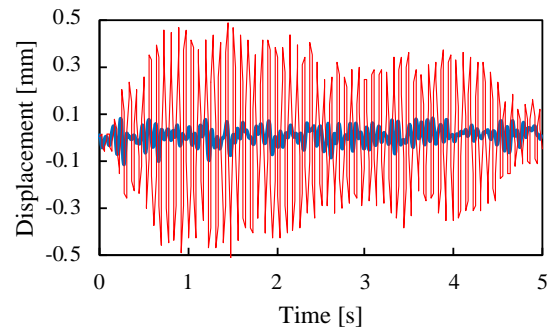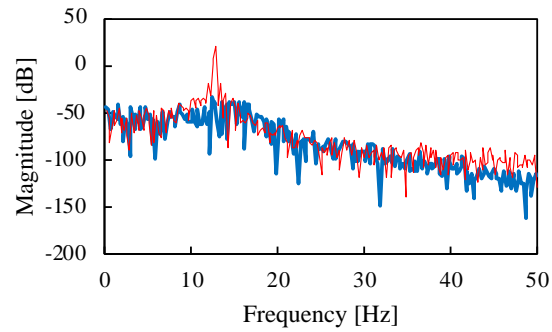Figures 7-9 show the time and frequency responses of displacement when using controllers configured with the DQN, DDPG, and TD3 algorithms, respectively. The amplitude of vibration for each method is much smaller than that for the uncontrolled method, indicating that the vibration was successfully controlled by the control method. The total displacement and H_∞ norm of the displacement are listed in Table 1. From the table, the control performance using DDPG and TD3 are higher than that using DQN. This is because the control input of DQN is discrete, whereas DDPG/TD3 has a continuous control input, providing a more optimal control input.

On the other hand, there was no significant difference in control performance between DDPG and TD3. This is because the two algorithms are similar, and the problem treated in this study was relatively simple, so the advantages of TD3, such as its high learning stability, were not fully utilized.

(a)Time response

(b) Frequency response

Figure 11. Control response to random disturbance

Figure 10 compares the time and frequency responses of displacement when using the controller with TD3 and using the simple proportional controller. The gain of the proportional controller was set so that the maximum value of the control input matches that of the controller using reinforcement learning. From Figure 10, it is known that the TD3 control method achieves faster vibration damping and lower peak than the proportional control method. Therefore, it can be said that the TD3 control method indicates higher control performance than the simple proportional control.

4.2 Results for random disturbance

The time and frequency responses of the displacements with the TD3 controller, after learning against the random disturbance was completed, are shown in Figure 11. The total displacement and the H_∞ norm of the displacement are listed in Table 2. The vibration amplitude is significantly suppressed compared to the uncontrolled case, and the H_∞ norm is reduced by about 55 dB. This indicates that the present controller is effective to suppress the vibration caused by random disturbances.

5. Conclusions

In this study, we proposed a controller configuration method for an unknown control target based on three different deep reinforcement learning algorithms. Vibration control experiments were conducted on a smart structure consisting of an aluminum plate and

piezoelectric actuators to verify the learning and control performance of these methods. Since the method is model-free, it is applicable to other continuum smart structures.

Vibration control experiments against impulse disturbances were conducted using controller configuration methods based on the DQN, DDPG, and TD3 algorithms. As a result, the H_∞ norm of the response of the controller with the DQN was about 24 dB lower than that without control, and the controllers with the DDPG and TD3 algorithm were about 40 dB lower than that without control.

Vibration control experiments against random disturbances were also conducted to verify the performance assuming under more realistic conditions. The controller based on TD3 was used. As a result, the H_∞ norm of the frequency response was successfully reduced by about 55 dB after the controller completed training compared to the uncontrolled case. This result confirms that the proposed method is applicable to random disturbances.

References

[1] M. Soori, B. Arezoo, and R. Dastres, "Artificial intelligence, machine learning and deep learning in advanced robotics, a review," *Cogn. Robot.*, vol. 3, pp. 54–70, 2023.

[2] S. Raschka, *Python Machine Learning, 2nd Edition*. Packt Publishing, 2017.

[3] S. M. Yang and Y. J. Lee, "Vibration Control of Smart Structures by Using Neural Networks," *J. Dyn. Syst. Meas. Control*, vol. 119, no. 1, pp. 34–39, 1997.

[4] S. Honda, Y. Narita, and N. Kida, "Adaptive control for vibration suppression by using self-organization map," *10th Asian Control Conf.*, 2015.

[5] Y. Li, *Deep Reinforcement Learning: An Overview*. 2017.

[6] D. Silver *et al.*, "A general reinforcement learning algorithm that masters chess, shogi, and Go through self-play," *Science*, vol. 362, no. 6419, pp. 1140–1144, 2018.

[7] W. Linglin, L. Yongxin, and Z. Xiaoke, "Design of reinforce learning control algorithm and verified in inverted pendulum," *34th Chinese Control Conf.*, 2015.

[8] G. Puriel-Gil, W. Yu, and H. Sossa, "Reinforcement Learning Compensation based PD Control for Inverted Pendulum," *15th Int. Conf. Electr. Eng. Comput. Sci. Autom. Control*, 2018.

[9] X. Wang, Y. Cheng, and W. Sun, "A Proposal of Adaptive PID Controller Based on Reinforcement Learning," *J. China Univ. Min. Technol.*, vol. 17, no. 1, pp. 40–44, 2007.

[10] Y. Qin, W. Zhang, J. Shi, and J. Liu, "Improve PID controller through reinforcement learning," *IEEE CSAA Guid. Navig. Control Conf.*, 2018.

[11] X. Mu, R. Huang, Q. Zou, and H. Hu, "Machine learning-based active flutter suppression for a flexible flying-wing aircraft," *J. Sound Vib.*, vol. 529, 2022.

[12] V. Samaitis, B. Yilmaz, and E. Jasiuniene, "Adhesive bond quality classification using machine learning algorithms based on ultrasonic pulse-echo immersion data," *J. Sound Vib.*, vol. 546, 2023.

[13] V. Mnih *et al.*, *Playing Atari with Deep Reinforcement Learning*. 2013.

[14] T. P. Lillicrap *et al.*, *Continuous control with deep reinforcement learning*. 2015.

[15] S. Fujimoto, H. van Hoof, and D. Meger, *Addressing Function Approximation Error in Actor-Critic Methods*. 2018.

Development of Vibration Measurement System using a Microcontroller

Koji Sekine[a,*], Keigo Hayakawa[b]

[a]Field of Mechanical Engineering, Department of Creative Engineering, National Institute of Technology, Kushiro College. Email: sekine@kushiro-ct.ac.jp
[b]Advanced Course of Construction and Manufacturing System Engineering, National Institute of Technology, Kushiro College.

Abstract

It is important to interpret resonance in the design to reduce the vibration of mechanical structures, and to verify this resonance phenomenon by experiments and theoretical approach. In the measurement for the vibration of a continuous system, the experience and skill of the observer affect the measurement accuracy of the natural frequencies and vibration modes. Therefore, in this study, a vibration measurement system is developed to stably and quantitatively verify the natural vibration of the beams using a microcontroller and an ultrasonic sensor. The vibration measurement system consists of a microcontroller, a vibration motor and an ultrasonic sensor. The accuracy and validity of the natural frequencies of the beams measured by the system are discussed, and the performance of present system is evaluated on the basis of the measurement results of the natural frequencies and the natural vibration waveforms.

Keywords: Vibration measurement; natural vibration; continuous system; microcontroller; ultrasonic sensor

1. Introduction

Resonance phenomenon is an important issue in the design on the fields of machinery, construction, aerospace, and civil engineering. In order to reduce and control the vibration of the mechanical structures, it is important to comprehend the mechanism of vibration and verify the resonance phenomenon by experimental and theoretical means.

For years, the vibration of the beam as a continuous system has been studied widely and actively. Dickey [1] discussed the free vibration and dynamic buckling of the beams under axial force by describing the solution of the equations of system. Thambiratnam and Zhuge [2] investigated the free vibration analysis of a stepped beam on an elastic foundation by using the finite element method. Tsai et al. [3]indicated the vibration analysis for a beam with distributed internal viscous damping by applying Timoshenko beam theory. Capozucca [4] treated the analysis of vibration of cantilever beams consist of dameged carbon fiber reinforced plastics. Wu et al. [5] proposed a method of analyzing beam vibration by tracking a laser stripe as non-contact measurement technique for vibration of the beams. Lee [6] presented free vibration analysis of a laminated beam with delaminations using a layerwise theory.

Lin [7] presented the eigensolutions for an arbitrary number of cracks of a beam with various boundary conditions. Della et al. [8] solved analytically the vibration of beams with double delaminations without resorting to numerical approximation. Lee [9] analyzed mathematically the vibration characteristics of four parallel and uniform beams. Kerboua [10] presented the control and reducion the vibration of beams using smart materials. Sepehri-Amin et al. [11] investigated the vibration response of functionally graded and viscoelastic damped beams.

On the other hand, the researches using a microcontroller have been actively reported in various engineering fields recently. Priohutomo et al. [12] discussed the design of maneuver controls using a microcontroller to avoid the ship from the collision. Sitanayah et al. [13] designed and implemented a low-cost wireless system to count the number of cars and motorcycles in a parking lot using the microcontroller. In addition, Putra et al. [14] showed the design and development of a simulator that can represent the earthquakes using a microcontroller, the hydraulic actuator and the three-axis accelerometer.

In general, the vibration measurement of a continuous system requires an integrated system consists of such as accelerometers, vibrators, analyzers, oscillators and amplifiers. In addition, a system that supports to measure simply and comprehend intuitively the natural frequencies

*Corresponding author. Tel.: +81-154-57-7294
Otanoshike-Nishi 2-32-1, Kushiro, Hokkaido,
Japan, 084-0916

and vibration modes of a continuous system is valid in the acquisition for the fundamental of vibration phenomenon.

Therefore, in this study, a vibration measurement system consists of a microcontroller, a vibration motor and an ultrasonic distance sensor was developed to visualize and comprehend intuitively the natural frequencies and vibration modes of beams, which are one of continuous system.

In particular, the natural vibration waveforms in time series for a cantilever beam have been measured by using the present system. Based on the comparison between the measured results and theoretical ones for the natural frequencies of the aluminum beams, the performance of the present system is evaluated and discussed.

2. Test Piece and Modules

2.1. Test piece (Cantilever beam)

Figure 1 shows an aluminum beam applied for vibration measurement on present system. Since the beam is flexible, it is appropriate for the detection of the amplitude (vibration displacement), and it is suitable for the verification of natural frequency and vibration mode of the beams. In addition, since a beam is thin form, it is able to observe the vibration displacement even if the excitation force is not powerful.

2.2. Microcontroller

Arduino microcontroller demonstrates a superiority in developing the systems that use DC motor, stepper motor, LED diode, piezoelectric sounder and various sensors, etc. Therefore, as shown in Fig. 2, Arduino UNO having 16MHz ceramic resonator has been adopted in this study.

2.3. Ultrasonic sensor

Figure 3 shows the ultrasonic distance sensor adapted on present system measuring the vibration displacement of the beam. The sensor has characteristics of operating frequency 40kHz and a measuring distance range from 2cm to 400cm. The ultrasonic sensor enables the non-contact measurement of a beam vibration displacement.

2.4. Vibration motor

Figure 4 shows the vibration motor adapted on present system exciting the beam at the resonance frequency. The motor exhibits maximum driving frequency 200Hz and an acceleration 1G at a rated voltage of 3V, and is characterized by its small size and large excitation force. The vibration motor has been mainly used to excite the second-order natural vibration of the beam.

2.5. Motor driver

By using the DC motor driver with a bipolar type linear integrated circuit shown in Fig. 5, the vibration motor speed can be controlled using a variable resistor.
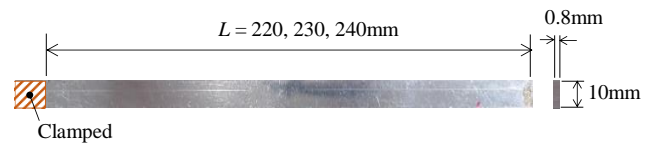

Figure 1. Geometry of an aluminum cantilever beam

Figure 2. Microcontroller (Arduino UNO)

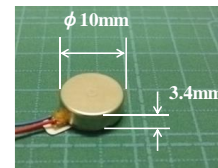Figure 3. Ultrasonic distance sensor (HC-SR04)

Figure 4. Vibration motor (Uxcell DC micromotor)

Figure 5. Motor driver (Toshiba TA7291P)

3. Vibration Measurement System

3.1. System for exciting the beam

Figure 6 presents the block diagram of system for exciting a beam. A vibration motor shown in Fig. 4 has been used for exciting the second-order natural vibration, and a DC motor with a reducer has been applied to induce the fundamental natural vibration of a beam. A program code to control the motor rotation speed (driving frequency) has been developed and applied to Arduino microcontroller. Present system can control the driving (excitation) frequency of the motor with a variable resistor. Also, the excitation frequency [Hz] of the motor can be indicated on the PC monitor. Furthermore, Figure 7 shows the circuit of the system for exciting a beam.
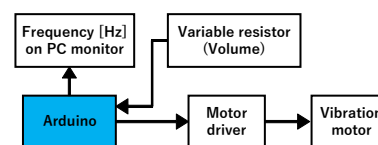

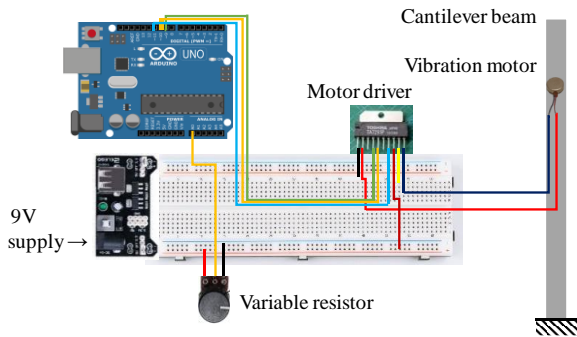Figure 6. Block diagram of system for exciting a beam

Figure 7. Circuit diagram of system for exciting a beam

3.2. System for measuring the vibration displacement

Figure 8 gives the block diagram of system for measuring vibration displacement of a beam. Two ultrasonic sensors shown in Fig. 3 have been located to measure simultaneously the vibration displacement of a beam at multiple points. A program code to take in the vibration displacement of a beam has been developed and applied to Arduino microcontroller. The acquired displacement data are represented on the PC monitor. Figure 9 shows the circuit diagram for measuring vibration displacement of a beam. Ultrasonic distance sensors have been located near the amplitude of an excited beam, and the vibration displacement data have been acquired in time series. Also, the maximum frequency that can be measured with this system is around 100Hz. It is possible to observe up to the second-order vibration mode with aluminum beam length L= 220mm to 240mm.

3.3. Setting position of sensors and motor

Figure 10 illustrates the setting position of the ultrasonic distance sensors and the vibration motor. Sensor-A and B have been located at the center and near the free end of the beam, respectively. In addition, the vibration motor has been attached with adhesive tape.
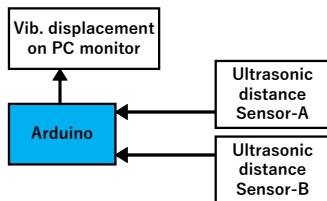

Figure 8. Block diagram of system for measuring vibration displacement of a beam
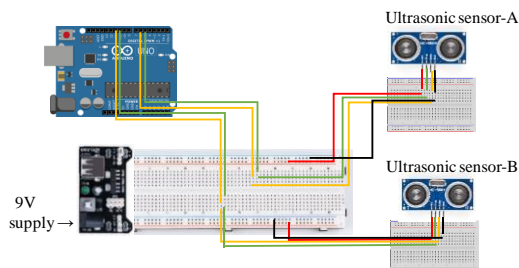

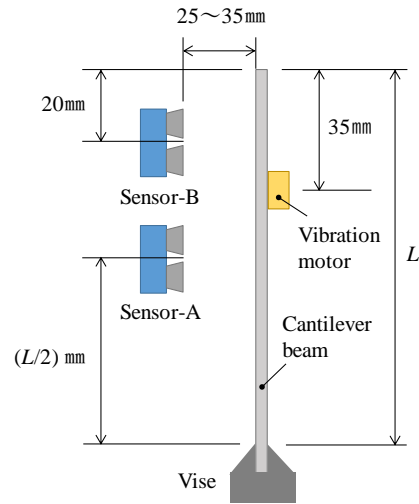Figure 9. Circuit diagram of system for measuring vibration displacement of a beam

Figure 10. Position of ultrasonic sensor and vibration motor
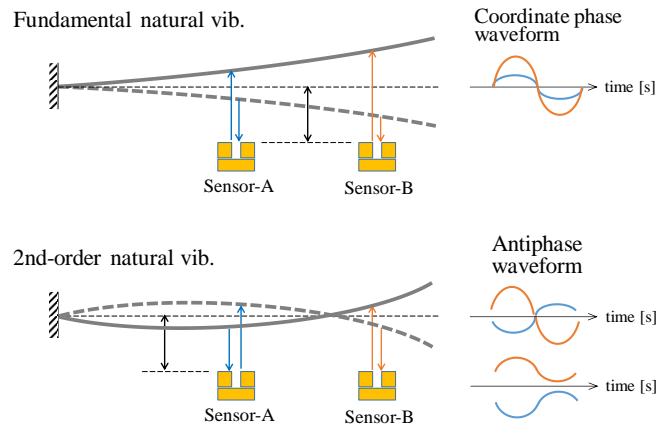
Figure 11. Discrimination for vibration mode of cantilever beam

3.4. Discrimination of vibration mode

Figure 11 demonstrates the concept of discrimination of vibration mode of the beam. Considering the natural vibration mode shapes of cantilever beam, the fundamental and second-order natural vibration can be distinguished from type of waveform having the coordinate phase or antiphase.

3.5. Discrete Fourier transform

The frequency spectrum of natural vibration displacement in time-series can be analyzed by the discrete Fourier transform (DFT) written in Eq. (1).

Also, a program code for numerical calculation of the frequency spectrum was developed according to the flow chart of the DFT processing shown in Fig. 12.

Sampling No.: $n\ (0 \sim N-1)$
Sampling number: N
Sampling period: Δt
Frequency: $f_k = k/(N\Delta t)\quad (k=0 \sim N/2-1)$
Imaginary unit: $i = \sqrt{-1}$

Vibration displacement in time series: $h(t_n) \equiv h_n$
Frequency spectrum: $|H(f_k)| \equiv |H_k|$

100

$$H_k = \sum_{n=0}^{N-1} h_n \, e^{-i\frac{2\pi nk}{N}} = \sum_{n=0}^{N-1} h_n \left(\cos\frac{2\pi nk}{N} - i \sin\frac{2\pi nk}{N} \right)$$

$$= \sum_{n=0}^{N-1} h_n \cos\frac{2\pi nk}{N} + i \left(-\sum_{n=0}^{N-1} h_n \sin\frac{2\pi nk}{N} \right)$$

$$= \text{Re}(H_k) + i \cdot \text{Im}(H_k)$$

$$|H_k| = \sqrt{\{\text{Re}(H_k)\}^2 + \{\text{Im}(H_k)\}^2} \tag{1}$$

3.6. Experiment procedures and setting

Experiment procedures for exciting and measuring of the beam by the present system are as follows:
- Adjust the variable resistor to drive the vibration motor and induce the natural vibration mode of the beam.
- Observe and save the sampling data of the vibration displacement measured by the ultrasonic sensor on the PC monitor.
- Analyze the frequency spectrum (natural frequency) of the beam by applying the Fourier transform to the vibrational displacements in time-series.

4. Measurement Results and Discussion

In this section, the measurement results for the natural vibration of a cantilever beam acquired by present system are illustrated, and the performance of the system will be evaluated.

Figure 13 gives the fundamental and second-order natural vibration displacements in time-series of the cantilever beam obtained by using present system. The vibration displacement waveforms measured by sensor-A and B show "Coordinate phase" in the case of fundamental natural vibration. Also, the vibration displacement waveforms show "Antiphase" in the case of second-order natural vibration. This phenomenon follows the concept of discrimination of vibration mode of a cantilever beam shown in Fig. 11.
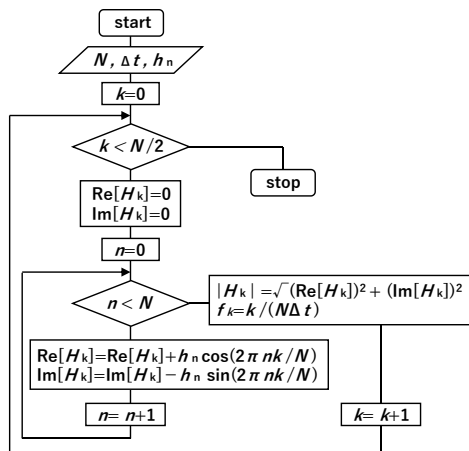
Figure 12. Flowchart of DFT processing

Figure 14 presents the results of the spectrum analysis by the discrete Fourier transform (DFT) for the natural vibration waveform in time-series shown in Fig. 13. The spectrum components of the fundamental and second-order natural frequencies detected by DFT analysis are 12.9Hz and 78.3Hz at L=220mm, 11.9Hz and 73.8Hz at L=230mm, 10.8Hz and 71.8Hz at L=240mm, respectively. As can be clearly seen in Fig. 14, each frequency spectrum components (natural frequencies) of the cantilever beam are expressly extracted even though there are countless noise frequency components.

(a) L=220mm
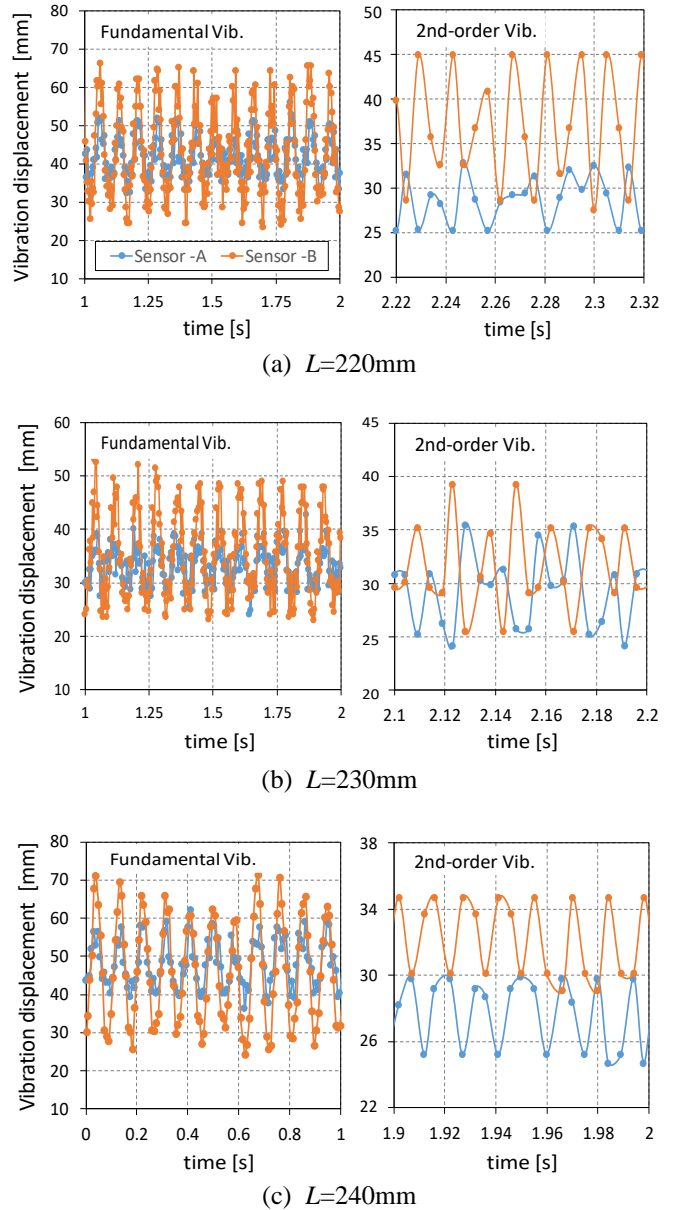
(b) L=230mm

(c) L=240mm

Figure 13. Natural vibration displacements of cantilever beams
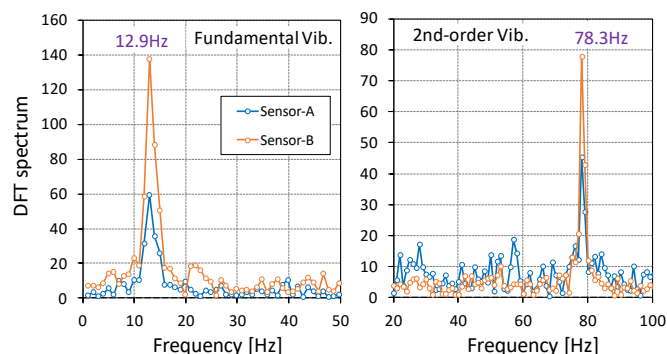
(a) *L*=220mm

(b) *L*=230mm

(c) *L*=240mm

Figure 14. Spectrum analysis for natural vibration displacements of cantilever beams

Table 1 demonstrates comparisons of natural frequencies for cantilever beams. Theoretical(exact) solutions for natural frequencies of a cantilever beam are given in Ref. [15], and Young's modulus 70GPa and the volume density 2700kg/m^3 have been employed as the material constants of the aluminum beam in the exact solutions. It is observed that the measured(DFT) results agree well with theoretical(exact) solutions, because the maximum re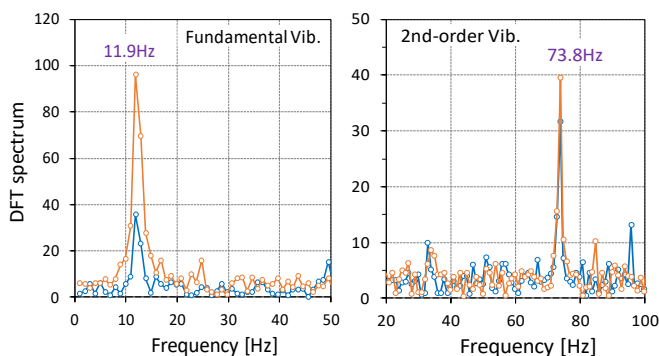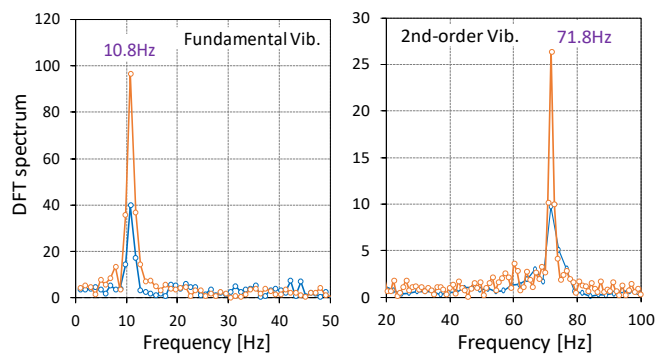lative difference between the measured results and exact solution is 8.1%. As can be seen, the accuracy and validity of the measured results can

be confirmed from the view point of the results for these comparisons between the natural frequencies.

Figure 15 indicates variations of natural frequencies with respect to the length of the cantilever beams. The exact solutions don't include the axial elongation and contraction, the transverse shear deformation of the beam and the mass effect of the vibration motor attached the beam. Therefore, the exact solutions tend to be higher than the measured results. Also, it can be seen that the natural frequencies decrease as the length of the beam increases. In fundamental natural vibration, there is almost no effect of variation of beam length on the relative difference between the measured results and the exact solutions.

Regarding second-order natural vibration, the relative difference between the measured results and the exact solutions seems to be larger for the shorter beam. From this tendency, it is guessed that the measured value is smaller than the exact solution, because the effect of transverse shear deformation is more pronounced for the shorter beam in the case of second-order natural vibration.

5. Conclusions

In this paper, the vibration measurement system for a cantilever beam has been presented, which consists of a vibration motor, a microcontroller and an ultrasonic distance sensor. The natural vibration waveforms in time series for a cantilever beam have been measured by using the present system. Also, the fundamental and second-order natural frequencies, which are the spectrum components of natural vibration waveforms of the cantilever beam have been detected by applying the discrete Fourier transform (DFT).

Comparisons between the measured results and the theoretical(exact) solutions for the natural frequencies of cantilever beams have been demonstrated and discussed. The measured results agreed well with the theoretical solutions, and the accuracy and validity for the natural frequencies of the beams measured by the present system have been confirmed. Also, if the mass of the attached vibration motor could be included as locally point mass in the beam theoretical model, the theoretical solutions would be closer to the experimental results and more accurate.

Table 1. Comparisons of natural frequencies for cantilever beams

Beam length [mm]	Mode No.	Meas. [Hz] (DFT)	Theory [Hz] (Exact)	Diff.
220	1	12.9	13.6	-5.1%
	2	78.3	85.2	-8.1%
230	1	11.9	12.4	-4.0%
	2	73.8	78.0	-5.4%
240	1	10.8	11.4	-5.3%
	2	71.8	71.6	0.3%

Diff. [%] = { (Meas. − Theory) / Theory }×100

In addition, taking into account the identity taken from the comparisons of natural frequencies, the validity for the performance and the function with respect to the present vibration measurement system using a microcontroller has been evaluated.

Present system has proposed a non-contact measurement technique of vibration displacement. It is expected that the measurement of higher-order natural frequencies of the beam will become possible if more sampling data for the vibration displacement can be acquired with microcontroller having high specification.

The use of this system will be expanded if the measured vibration displacement data can be displayed on the PC monitor in real time, or if a communication module can be connected to the microcontroller to monitor remotely the measured data.
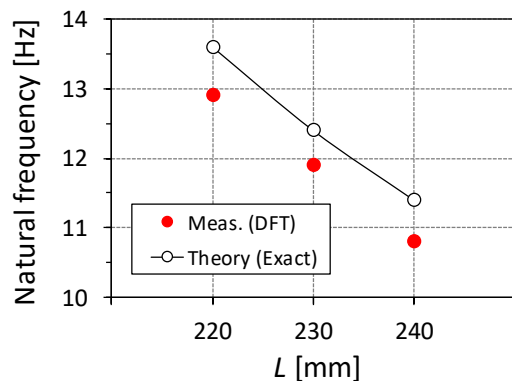
(a) Fundamental natural vibration
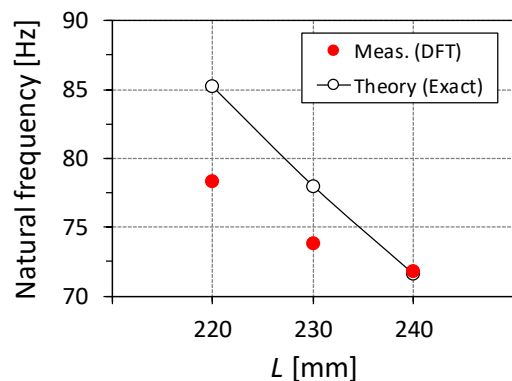
(b) Second-order natural vibration

Figure 15. Variations of natural frequencies versus the length of cantilever beams

References

[1] R. W. Dickey, "Free vibrations and dynamics buckling of the extensible beam," *J. Math. Anal. Appl.*, vol. 29, no. 2, pp. 443–454, 1970.

[2] D. Thambiratnam and Y. Zhuge, "Free vibration analysis of beams on elastic foundation," *Comput. Stuctures*, vol. 60, no. 6, pp. 971–980, 1996.

[3] T. C. Tsai, J. H. Tsau, and C. S. Chen, "Vibration analysis of a beam with partially distributed internal viscous damping," *Int. J. Mech. Sci.*, vol. 51, no. 11–12, pp. 907–914, 2009.

[4] R. Capozucca, "Vibration of CFRP cantilever beam with damage," *Compos. Stuctures*, vol. 116, pp. 211–222, 2014.

[5] T. Wu, L. Tang, P. Du, N. Liu, Z. Zhou, and X. Qi, "Non-contact measurement method of beam vibration with laser stripe tracking based on tilt photography," *Measurement*, vol. 187, 2022.

[6] J. Lee, "Free vibration analysis of delaminated composite beams," *Comput. Stuctures*, vol. 74, no. 2, pp. 121–129, 2000.

[7] H. P. Lin, S. C. Chang, and J. D. Wu, "Beam vibrations with an arbitrary number of cracks," *J. Sound Vib.*, vol. 258, no. 5, pp. 987–999, 2002.

[8] C. N. Della and D. Shu, "Vibration of beams with double delaminations," *J. Sound Vib.*, vol. 282, no. 3, pp. 919–935, 2005.

[9] K. T. Lee, "Analytic solutions for vibration characteristics of a multi-beam structure," *Int. J. Mech. Sci.*, vol. 52, no. 7, pp. 952–969, 2010.

[10] M. Kerboua, A. Megnounif, M. Benguediab, K. H. Benrahou, and F. Kaoulala, "Vibration control beam using piezoelectric-based smart materials," *Compos. Stuctures*, vol. 123, pp. 430–442, 2015.

[11] S. Sepehri-Amin, R. T. Faal, and R. Das, "Analytical and numerical solutions for vibration of a functionally graded beam with multiple fractionally damped absorbers," *Thin-Walled Struct.*, vol. 157, 2020.

[12] K. Priohutomo, A. A. Masroeri, and C. Permana, "Maneuver control system for collision avoidance based on experimental study," *EPI Int. J. Eng.*, vol. 1, no. 2, pp. 65–69, 2018.

[13] L. Sitanayah, A. Angdresey, and J. W. Utama, "A low-cost vehicle counting system based on the internet of things," *EPI Int. J. Eng.*, vol. 4, no. 1, pp. 14–20, 2021.

[14] N. A. I. E. Putra, R. Syam, I. Renreng, T. Harianto, and N. R. Wibowo, "The development of earthquake simulator," *EPI Int. J. Eng.*, vol. 4, no. 2, pp. 134–139, 2021.

[15] I. H. Shames and C. L. Dym, *Energy and finite element methods in structural mechanics*. Taylor & Francis, 1985.

The effect of Spot Welding Parameters for Dissimilar Material Mild Steel and Galvanized Steel on Nugget Size and Mechanical Strength

La Ode Al Muslim[a], Ahmad Yusran Aminy[b], Azwar Hayat[c,*]

[a]Department of Mechanical Engineering, Engineering Faculty, Hasanuddin University. Email: laodealm@gmail.com
[b]Department of Mechanical Engineering, Engineering Faculty, Hasanuddin University. Email: ahmadyusran179@gmail.com
[c]Department of Mechanical Engineering, Engineering Faculty, Hasanuddin University. Email: azwar.hayat@unhas.ac.id

Abstract

The objective of this research was to analyze the effect of spot welding parameters on the size of the weld nugget and the maximum shear strength on dissimilar material mild steel and galvanized steel. The Taguchi and ANOVA methods were used to determine the welding parameters' contribution to joint quality. Experimental design using Minitab-19 software with Taguchi method of 3 level 3 factor with L27 runs. Specimen size and dimensions were made using ASTM D1002 standard, with a plate thickness of 0.8 mm. Taguchi analysis S/N ratio data mean for weld nugget diameter with three levels of current used, 4 kA, 6 kA, and 8kA, shows the most influential on the diameter of the weld nugget was at 8 kA. The three levels of welding time used, 2s, 4s, and 6s, show the most influential on the diameter of the nugget the weld was at the third level for 6 seconds. It found that there was no significant difference in the size nugget at the three electrode pressure levels of 30 Ppsi, 40 Psi, and 50 Psi. Based on the tensile test and Taguchi analysis, the lowest shear strength was found in a weld nugget size of 3.15 mm at a welding current of 4 kA, a welding time of 2 seconds, an electrode pressure of 30 Psi, with a shear tensile strength of 300.19 N. Along with an increase in the size weld nugget correlated to an increase of shear strength. The highest shear tensile strength was found in the nugget size of 4.16 mm, with a welding current of 8 kA, welding time of 2 seconds, electrode pressure of 50 Psi, with a shear tensile strength of 3383.43 N. From the ANOVA, it found that the three factors of spot welding parameters were used, the most influential parameter in the formation of weld nuggets was welding current with a contribution of 84.86% then followed by welding time with a contribution of 14.86% and electrodes force with a contribution of 0.13%. Then from the three factors of spot welding parameters that were used the most influential parameter on the maximum shear tensile strength was the welding current with a contribution of 95.86 % then followed by welding time with a contribution of 0.52% and electrodes force with a contribution of 0.05%.

Keywords: Spot welding; weld nugget diameter; tensile-shear

1. Introduction

Spot welding is a method of joining sheet plates in the automotive industry [1]. The spot welding process occurs during a certain cycle time in the welding current, welding time, and electrode force are the most important parameters [2]. Spot welding is used in the automotive industry for car bodies or frameworks. There are about 5000 spot welds in modern vehicles [3].

Spot welding is a method of joining metals by providing electrical resistance as a heat source on two or more metal surfaces so that nuggets are formed in the welding area [4]. The connection is done by pressing the surface of the plate to be connected with the two electrodes. At the same time, an electric current flows to the electrodes so that the two metal surfaces are hot and melt due to electrical resistance [5].

The spot welding method has the advantages of being easy to operate since it does not require special skills like other welding methods, the time is shorter, so it will increase the speed of mass production, and the heat supply provided is sufficient [6].

Control of welding parameters greatly affects the characteristics of the weld results, its affects the quality of the mechanical properties of the weld results, such as tensile strength, hardness, and microstructure. One of crutial thing is controlling the electric current. If the welding current used is too low, the heat that occurs is not enough to melt the material, resulting in a small area of weld metal and lack of penetration, conversely, if the welding current is too high, the melting of the base metal is too fast and produces a wide area of weld metal. as well as deep penetration resulting in low tensile strength and increased brittleness [7].

Variations in electric voltage (V) and pressing time (dt) affect the shear strength of the weld. The higher the stress used, the higher the value of the shear stress strength. When the pressure or welding time is long, the value of the shear stress strength is higher and if the welding time is not constant, the welding results will be damaged [8]. It takes sufficient heat input to form a good

nugget structure so as to produce maximum joint strength. The welding pressure time must be adjusted in order to get the results of the weld joint and good tensile strength [9].

The size of the nugget diameter increases with increasing stress which causes a pullout failure mode. The size of the nugget diameter decreases after the pre-strain is applied to the test specimen and creates an interfacial failure mode [10]. Research effects of holding time on microstructure and shear strength of resistance spot-welded joints between mild steel and aluminum with zinc powder filler. The materials used are 0.9 mm thick mild steel, 1.2 mm thick 3000 series aluminum, and 200 mesh zinc powder. The tensile test results showed that applying an electric current of 8000 A, welding time of 0.5 s, and holding time of 1 s produced the joint with the weakest shear strength of 130 N. The highest joint shear strength of 790 N is obtained with the condition: electric current of 9000 A, welding time of 0.5 s, and holding time of 5 s [11].

This research uses several variations of parameters that can affect the characteristics of mechanical properties, in order to improve the quality of the welded joints. Research on spot welding with variations in the parameters of welding current, welding time, electrode force, and its mechanical properties are the focus of the study.

2. Research Method

2.1. Materials and tools

Materials used for this study were Mild steel and Galvanized steel. The chemical composition of both materials can be seen in Table 1.

The tool that would be used in this research was spot welding to joints galvanized steel and mild steel materials with an electric current capacity of 1 to 8 kA and an electrode pressure capacity of 10 to 50 Psi, grinding machine. To determine the mechanical strength of a material, a Tensile test was conducted to spot welded 0.8 mm thick of mild steel iron plate and 0.8 mm thick of galvanized steel plate. The process of making specimens follow ASTM D1002 standards.

The process of selecting welding parameters selected based on the capacity of the tool to be used was then designed using Minitab-19 software, the Taguci 3 level 3 factor method with L27 runs, and further analyzed with ANOVA.

Table 1. Chemical composition of materials (wt %)

Chemical Composition	Mild steel	Galvanized steel
Cu	0.0067	0.053
Fe	99.3	
Si	0.16	0.009
Cr	0.0093	0.01
Mn	0.192	0.40
Ti	0.0015	
S	0.0035	0.017
C	0.114	0.065
P	0.0073	0.018

2.2. Specimen making

The process of making specimens was by cutting mild steel and galvanized steel plates, with specimen dimensions according to ASTM D1002 standards with a thickness of 0.8 mm, a length of 100 mm, and a width of 25.4 mm as shown in Fig. 1. The connection method was made overlapping (lap joints).

2.3. Specimen welding

In the process of welding the specimens of this research would be used of 3 (three) welding parameters, namely welding time, welding current, and electrode pressure. Three welding parameters have three different levels of variation were used, namely, welding currents of 4, 6, and 8 kA, welding times of 2, 4, and 6 seconds, and electrode pressures of 30, 40, and 50 Psi.
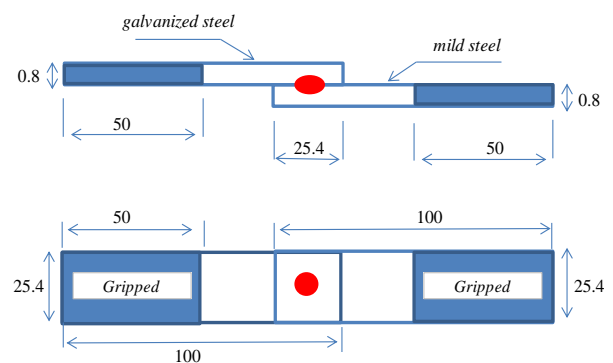
Figure 1. Specimen sizes based on ASTM D1002 [12]

Table 2. Taguchi design welding parameters

Runs	Welding current (kA)	welding time (seconds)	electrode force (Psi)
1	4	2	30
2	4	2	30
3	4	2	30
4	4	4	40
5	4	4	40
6	4	4	40
7	4	6	50
8	4	6	50
9	4	6	50
10	6	2	40
11	6	2	40
12	6	2	40
13	6	4	50
14	6	4	50
15	6	4	50
16	6	6	30
17	6	6	30
18	6	6	30
19	8	2	50
20	8	2	50
21	8	2	50
22	8	4	30
23	8	4	30
24	8	4	30
25	8	6	40
26	8	6	40
27	8	6	40

Figure 2. Schematic of the stages of the welding process

Schematic of the stages of the welding process according to Fig. 2 are as follows;

- Stage 1 was the initial condition where the two materials have not been clamped by the two electrodes.
- Stage 2 was the stage where welding began.
- Stages 2 and 3 were the welding stages where at this stage an electric current of 4, 5, and 8kA flowed through the electrode to the workpiece, and the electrode pressure force of 30, 40, and 50 Psi was maintained for 2, 4 and 6 seconds to produce heat and form weld nuggets.
- Stage 4 was the final stage where the electric current is turned off and the electrode pressure was lifted when the weld nugget has been formed.

3. Results and Discussion

3.1. Weld nugget

The nugget was an area of welded metal that has melted and then solidified. The size of the weld nugget is the most important parameter in determining the mechanical behavior of the spot welding joint since its predominantly determined by the shape and size of the weld nugget [13].

From Table 3, it could be seen that the relationship between each welding parameter and the diameter of the welding nugget varies. Where the measurement results showed that for every increase in electric current, there was also an increase in the size of the nugget as well as an increase in the level of time there was an increase in the size of the weld nugget. From the calculation data, the smallest average nugget diameter was found in the parameter of welding current of 4 kA, welding time of 2 seconds, and electrode pressure of 30 Psi with a value of 3.15 mm.

The largest nugget size was found in the parameters of a welding current of 8 kA, welding time of 6 seconds, and electrode pressure of 40 Psi with a value of 4.75 mm.

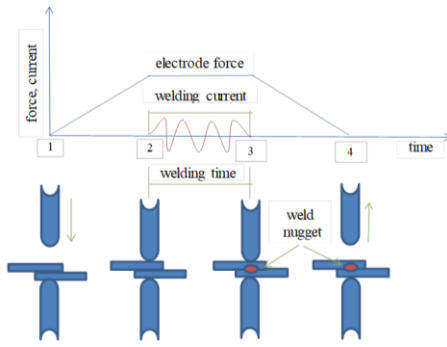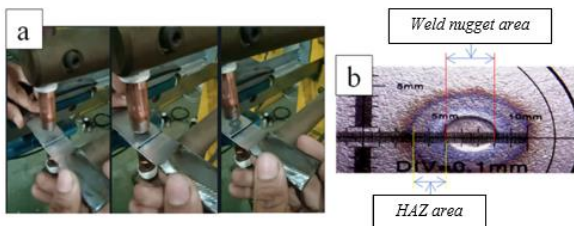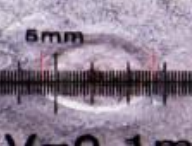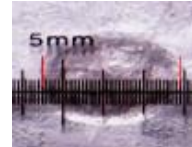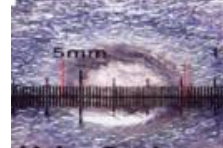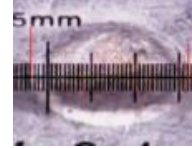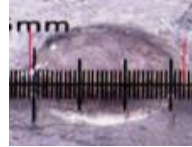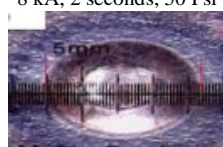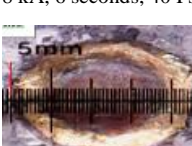Figure 3. (a) Spot welding process and (b) weld nugget measurement area

Table 3. Measurement results of weld nugget diameters

No	Figure of mild steel nugget	Figure of galvanized steel nugget
1	4 kA, 2 seconds, 30 Psi	4 kA, 2 seconds, 30 Psi
2	4 kA, 4 seconds, 40 Psi	4 kA, 4 seconds, 40 Psi
3	4 kA, 6 seconds, 50 Psi	4 kA, 6 seconds, 50 Psi
4	6 kA, 2 seconds, 40 Psi	6 kA, 2 seconds, 40 Psi
5	6 kA, 4 seconds, 50 Psi	6 kA, 4 seconds, 50 Psi
6	6 kA, 6 seconds, 30 Psi	6 kA, 6 seconds, 30 Psi
7	8 kA, 2 seconds, 50 Psi	8 kA, 2 seconds, 50 Psi
8	8 kA, 4 seconds, 30 Psi	8 kA, 4 seconds, 30 Psi
9	8 kA, 6 seconds, 40 Psi	8 kA, 6 seconds, 40 Psi
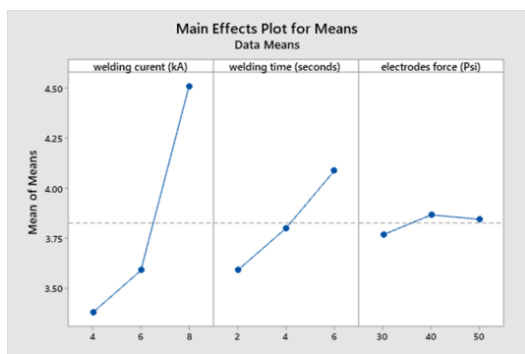
Figure 4. Taguchi Analysis S/N ratio data means for weld nugget diameter

Figure 5. Taguchi Analysis S/N ratio data means for tensile- maximum shear

Taguchi Method Software Minitab-19 weld nugget diameters are shown in Fig. 4. From Fig. 4 It could be seen that of the three current levels used that the most influential on the diameter of the weld nugget was at the third level of 8 kA, then of the three levels of welding time using the most influential the diameter of the weld nugget was at the third level of 6 seconds three levels of electrode pressure there was no significant difference.

Analysis of ANOVA in Minitab-19 weld nugget diameters can be seen in Table 4. From Table 4 ANOVA in Minitab-19 software could be seen from the three factors of spot welding parameters that were used the most influential parameter in the formation of welding nuggets was welding current with a contribution of 84.86% then followed by welding time with a contribution of 14.86%. and electrode force with a contribution of 0.13%.

3.2. Shear tensile testing

Tensile testing was carried out to determine the most influential parameter on shear tensile strength from three factors of welding current, welding time, and electrode pressure, three levels of variation of welding current 4 kA, 6 kA, and 8 kA. Welding time is 2 seconds, 4 seconds, and 6 seconds. Electrode pressure 30 Psi, 40 Psi, and 50 Psi.

Table 4. Analysis of Variance software Minitab-19 weld nugget diameter

Source	DF	Seq SS	Contribution	Adj SS	Adj MS	F-Value	P-Value
welding current (kA)	2	2.05358	84.86%	2.05358	1.02679	545.38	0.002
welding time (seconds)	2	0.35951	14.86%	0.35951	0.17975	95.48	0.010
electrodes force (Psi)	2	0.00321	0.13%	0.00321	0.00160	0.85	0.540
Error	2	0.00377	0.16%	0.00377	0.00188		
Total	8	2.42006	100.00%				

Table 5. The average value of the tensile shear test results

No	Welding current (kA)	Welding time (second)	Eletrda force (Psi)	tensile- shear maximum (N)
1	4	2	30	300.19
2	4	4	40	543.96
3	4	6	50	595.56
4	6	2	40	703.56
5	6	4	50	592.38
6	6	6	30	1094.38
7	8	2	50	3383.43
8	8	4	30	3042.53
9	8	6	40	3130.70
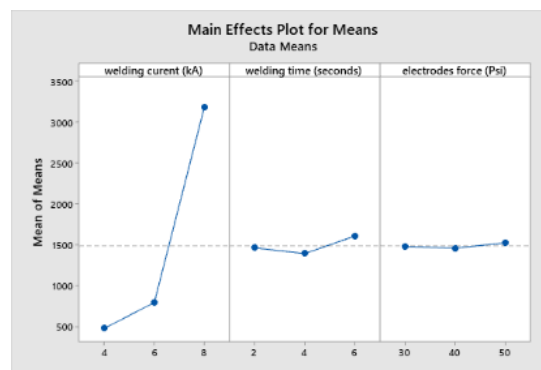
Taguchi Method Software Minitab-19 tensile-shear maximum is shown in Fig. 5. From Fig. 5 Taguchi Analysis S/N ratio data means for tensile-shear maximum. Of the three levels of welding current used, the most influential on the maximum tensile-shear is at the third level, 8 kA, of the three levels of welding time used, there was no level that significantly affects the maximum tensile-shear, which could be analyzed from Table 5. The welding time was adjusted according to the current used. And of the three electrode pressure levels there was no significant value affecting the maximum tensile-shear.

From Table 6 ANOVA in Minitab-19 software could be seen from the three factors of the spot welding parameter which was used the most influential parameter on the maximum shear tensile strength was the welding current with a contribution of 95.86% then followed by welding time with a contribution of 0.52% and electrodes force with a contribution of 0.05%. In line with research conducted by Sukarman et al which has the most effect on welding current than welding time [14].

Table 6. Analysis of Variance software Minitab-19 tensile-shear maximum

Source	DF	Seq SS	Contribution	Adj SS	Adj MS	F-Value	P-Value
welding current (kA)	2	39381750	95.86%	39381750	19690875	268.62	0.000
welding time (seconds)	2	214384	0.52%	214384	107192	1.46	0.255
electrodes force (Psi)	2	19600	0.05%	19600	9800	0.13	0.876
Error	20	1466053	3.57%	1466053	73303		
Lack-of-Fit	2	520316	1.27%	520316	260158	4.95	0.019
Pure Error	18	945737	2.30%	945737	52541		
Total	26	41081786	100.00%				

Table 7. The average value of the results of nugget diameter measurements and maximum tensile shear testing

No	Welding current (kA)	Welding time (second)	Electrode force (Psi)	Diameter nugget (mm)	Tensile- Shear Maximum (N)
1.	4	2	30	3.15	300.19
2.	4	4	40	3.40	543.96
3.	4	6	50	3.60	595.56
4.	6	2	40	3.30	703.56
5.	6	4	50	3.55	592.38
6.	6	6	30	3.73	1094.38
7.	8	2	50	4.16	3383.43
8.	8	4	30	4.46	3042.53
9.	8	6	40	4.75	3130.70
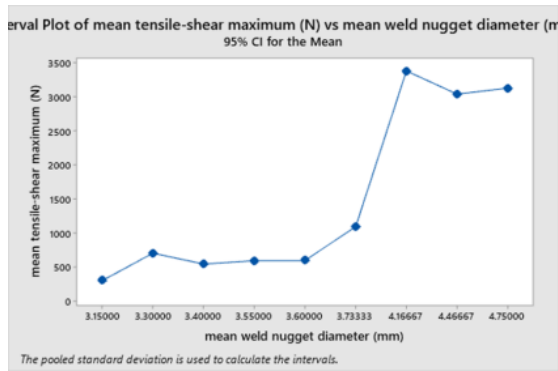
Figure 6. Mean tensile-shear maximum versus mean weld nugget diameter

From Table 7 and Fig. 6, it could be seen that the lowest shear tensile strength was found in the weld nugget size 3.15 mm at a welding current of 4 kA, welding time of 2 seconds, electrode pressure of 30 Psi, with a shear tensile strength of 300.19 N as the size increases The shear strength of weld nuggets increased and the highest shear strength was found in the size of the weld nugget 4.16 mm, with a welding current of 8 kA, welding time of 2 seconds, electrode pressure of 50 Psi, with a shear tensile strength of 3383.43 N. This gave knowledge about the effect of weld nugget size on spot welding shear tensile strength.

There was a decrease in shear tensile strength on the weld nugget size 4.46 mm, with a welding current of 8 kA, a welding time of 4 seconds, an electrode pressure of 30 Psi, and a weld nugget size of 4.75 mm, with a welding current of 8 kA, a welding time of 6 seconds, electrode pressure 40 Psi. This was because the higher the welding current and the longer the welding time, the greater the heat input that occurs [15].
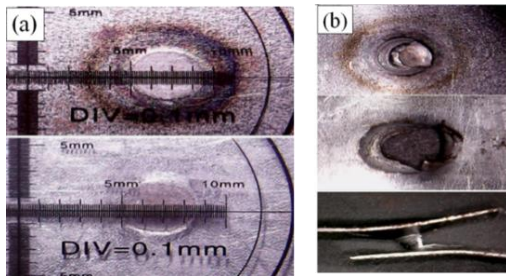
Figure 7. Type of failure of the tensile shear test results

From Fig. 7 It could be seen that the type of material failure resulting from the tensile shear test in Figure (a) was the result of the test with the lowest shear tensile strength of 300.19 N at a welding current of 4 kA, a welding time of 2 seconds, an electrode pressure of 30 Psi, with an interfacial failure mode failure type and in figure (b) was the highest shear tensile strength test result, namely 3383.43 N at a welding current of 8 kA, a welding time of 2 seconds, an electrode pressure of 50 Psi, with a pull-out failure mode failure type.

Table 8. The average value of the tensile shear test is mild steel with mild steel and galvanized steel with galvanized steel

Welding current (kA)	Welding time (seconds)	Eletroda force (Psi)	Tensile-shear maximum (N) mild steel	Tensile-shear maximum (N) galvanized steel
4	2	30	1731.07	195.14
8	2	50	3770.9	2765.47
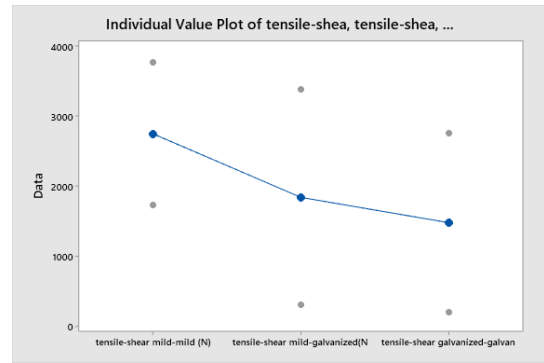
Figure 8. Comparative graph of the tensile-shear test results of mild steel with mild steel, galvanized steel with galvanized steel, and mild steel with galvanized steel

From Fig. 8, tt can be seen that the decrease in tensile-shear strength in the joints of mild steel with galvanized steel and galvanized steel with galvanized steel is caused by a galvanic coating on the material. in line with Sukarman et al decreased weldability due to zinc coating on the metal surface [14].

3.3. Micro structure
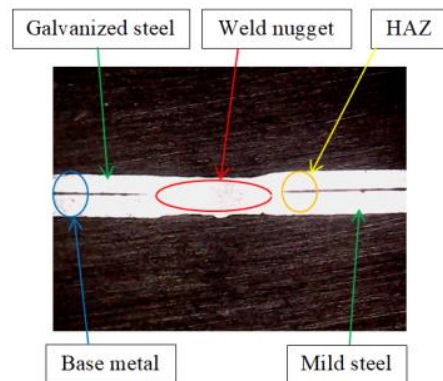
Figure 9. Microstructure observation area
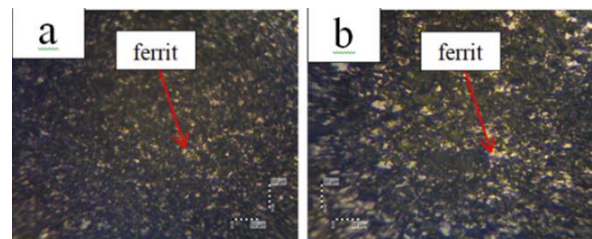
Figure 10. Structure midro base metal (a) galvanized steel (b) mild steel. It could be seen that the pearlite microstructure consists of layers of black cementite and white ferrite
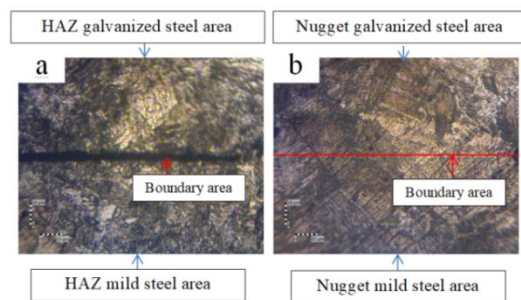
Figure 11. Microstructure 4 kA, 2 sec, 30 Psi, (a) HAZ area, and (b) nugget area

108
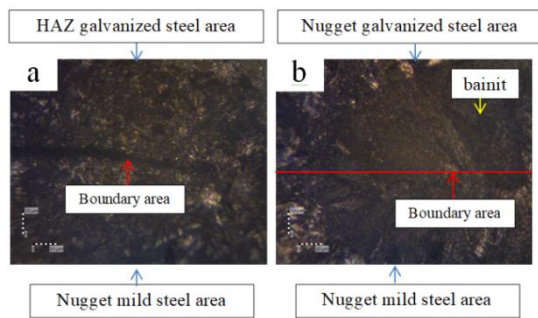
Figure 12. Microstructure 8 kA, 2 sec, 50 Psi (a) HAZ region and (b) nugget region

From the results of microstructural observations, structural changes could be seen between the base metal, the HAZ area, and the welding nugget. In the base metal area, a coarse pearlite microstructure was visible, consisting of layers of black cementite and white ferrite, in the HAZ region there was a structural change to a fine pearlite microstructure, and in the weld nugget area, a fine pearlite microstructure was visible. As the welding current increases, the weld nugget area was dominated by the bainite microstructure, this occurs due to the different heat inputs for each variation of the welding parameters [9]. The bainite structure was formed through the heat treatment process of steel which was heated to reach the austenite temperature and cooled at a high speed moderate [16].

4. Conclusion

From the analysis of Taguchi and Anova, it could be concluded that from the 3 factors and 3 levels of the spot welding parameters used, the increasing welding current and the increasing welding time, the size of the weld nugget also increases. The lowest shear strength was found in the weld nugget size 3.15 mm at a welding current of 4 kA, welding time of 2 seconds, and electrode pressure of 30 Psi, with a shear tensile strength of 300.19 N. As the size of the weld nugget increases, the shear tensile strength increases, and the highest shear tensile strength was found in the weld nugget size of 4.16 mm, with a welding current of 8 kA, a welding time of 2 seconds, an electrode pressure of 50 Psi, with a shear tensile strength of 3383.43 N. From the analysis of ANOVA software Minitab-19 it could be seen from three The spot welding parameter factor that was used as the most influential parameter in the formation of weld nuggets was the welding current with a contribution of 84.86%, followed by welding time with a contribution of 14.86% and electrodes force with a contribution of 0.13%.

Then from the three factors of spot welding parameters that were used the most influential parameter on the maximum shear tensile strength was the welding current with a contribution of 95.86% then followed by welding time with a contribution of 0.52% and electrodes force with a contribution of 0.05%. The results of microphoto observations along with increasing welding parameters in the weld nugget area formed a bainite microstructure.

But this research is still limited so it is suggested to clean the galvanized layer to see the effect on tensile-shear strength and nugget diameter.

References

[1] J. Sim and K. Y. Kim, "Instance selection-based dissimilar weldment design prediction for resistant spot welding," *Adv. Eng. Informatics*, vol. 52, 2022.

[2] J. P. Oliveira, K. Ponder, E. Brizes, T. Abke, A. J. Ramirez, and P. Edwards, "Combining resistance spot welding and friction element welding for dissimilar joining of aluminum to high strength steels," *J. Mater. Process. Technol.*, vol. 273, 2019.

[3] M. L. Saad, M. H. Sar, O. S. Barrak, S. K. Hussein, and A. K. Hussein, "Fuzzy logic model analysis of shear force in aluminium/polyethylene lap joined by hot press," *IOP Conf. Ser. Mater. Sci. Eng.*, vol. 518, 2019.

[4] M. P. Mubiayi, E. T. Akinlabi, and M. E. Makhatha, *Current trends in friction stir welding (FSW) and friction stir spot welding (FSSW)*. Springer International Publishing, 2019.

[5] P. Muthu, "Optimization of the process parameters of resistance spot welding of AISI 316l sheets using Taguchi method," *Mech. Mech. Eng.*, vol. 23, no. 1, pp. 64–69, 2019.

[6] N. Charde, "Effects of Electrode Deformation on Carbon Steel Weld Geometry of Resistance Spot Welding," *Orig. Res. J.*, vol. 1, no. 5, pp. 5–12, 2012.

[7] A. Soetardjo, *Las Listrik dan Otogen*. Jakarta: Ghalia Indonesia, 1997.

[8] M. H. Sar, M. H. Ridha, I. M. Husain, O. S. Barrak, and S. K. Hussein, "Influence of Welding Parameters of Resistance Spot Welding on Joining Aluminum with Copper," *Int. J. Appl. Mech. Eng.*, vol. 27, no. 2, pp. 217–225, 2022.

[9] B. Wang *et al.*, "Microstructure and shearing strength of stainless steel/low carbon steel joints produced by resistance spot welding," *J. Mater. Res. Technol.*, vol. 20, pp. 2668–2679, 2022.

[10] F. Yaghoobi, R. Jamaati, and H. J. Aval, "Resistance spot welding of high-strength DP steel and nano/ultrafine-grained IF steel sheets," *Mater. Chem. Phys.*, vol. 281, 2022.

[11] M. A. Hendrawan, K. A. Ilman, and T. Kunimine, "Effects Of Holding Time On Microstructure And Shear Strength Of Resistance Spot-Welded Joints Between Mild Steel And Aluminum With Zinc Powder Filler," *High Temp. Mater. Process. An Int. Q. High-Technology Plasma Process.*, vol. 27, no. 4, 2023.

[12] ASTM International, *Designation D1002 Standart Test Method For Apparent Shear Strength Of Single-Lap-Joint Adhesively Bonded Metal Specimens By Tension Loading (Metal-To-Metal)*. 2019.

[13] A. S. Baskoro, A. Edyanto, M. A. Amat, and H. Muzakki, "Study on Nugget Growth in Resistance Spot Welding of Thin Aluminum A1100 Using Welding Simulation," *Mater. Sci. Forum*, vol. 929, pp. 191–199, 2018.

[14] Sukarman *et al.*, "Optimization of Tensile-Shear Strength in the Dissimilar Joint of Zn-Coated Steel and Low Carbon Steel," *Automot. Exp.*, vol. 3, no. 3, pp. 115–125, 2020.

[15] S. S. Rao, K. S. Arora, L. Sharma, and R. Chhibber, "Investigations on Mechanical Behaviour and Failure Mechanism of Resistance Spot-Welded DP590 Steel Using Artificial Neural Network," *Trans. Indian Inst. Met.*, vol. 74, pp. 1419–1438, 2021.

[16] W. D. Callister and D. G. Rethwisch, *Materials Science and Engineering: An Introduction*. New York: John wiley & sons, 2007.

Energy-Saving Driving for a Flexible Manipulator by Utilizing Micro Fiber Composite

Akira Abe[a,*]

[a]Department of Systems, Control and Information Engineering, National Institute of Technology, Asahikawa College.
  Email: abe@asahikawa-nct.ac.jp

Abstract

In this paper, we examine a point-to-point motion task of a flexible manipulator with macro fiber composite (MFC) and then propose a new feedforward control method to suppress driving energy and residual vibration simultaneously. For this, we use an MFC attached to one side of the flexible manipulator that has one revolute joint as an actuator. We attempt to express the joint angle in the control technique by combining cycloidal and polynomial functions. On the other hand, the input voltage profile of the MFC is expressed using Gaussian functions. The trajectory of the joint angle and the input voltage profile are dependent upon the coefficients of the polynomial function and the Gaussian functions, respectively. The trajectory and the input voltage profile are optimized simultaneously to cancel the residual vibration under saving energy by tuning the coefficients using the particle swarm optimization algorithm. The effectiveness of the proposed method is verified by performing simulations and experiments. Thus, our findings confirmed that the simultaneous optimization of the trajectory of the joint angle and the input voltage of the MFC saves more energy than only the optimization of the trajectory. Therefore, we could establish an energy-saving feedforward control method by driving two actuators.

Keywords: Feedforward control; residual vibration suppression; energy saving; macro fiber composite actuator

1. Introduction

Lighter structures are generally preferred in industrial machinery, from the viewpoint of high-speed operations to improve production efficiency. In particular, there is an increased demand for such structures for robotic manipulators, which are key components of industrial robot systems. A low-stiffness manipulator induces undesirable vibrations, adversely affecting the accuracy of robotic operations. From this perspective, numerous studies [1]–[6] have focused on the vibration control of low-rigidity robot manipulators, treating them as flexible manipulators. In recent years, vibration control of thin-walled structures using piezoelectric elements as actuators has gained much research attention [7]–[12]. Specifically, macro fiber composite (MFC), which is a piezoelectric element, is more suitable for vibration control of flexible structures due to its flexibility, durability, and higher power compared to conventional piezoelectric ceramic PZT. Some researchers have investigated the vibration control of flexible manipulators using MFC as actuators. For example, Yang et al. [13] investigated the dynamic modeling and adaptive vibration suppression of a flexible macro-micro manipulator, which comprised a macro stage and a flexible MFC micromanipulator. They considered a nonlinearity of the MFC based on the Bouc–Wen hysteresis equation in dynamic modeling. They also

presented a hybrid control strategy consisting of a trajectory planning method of the joint angle of the macro stage and an adaptive variable structure control by the MFC actuator to simultaneously suppress the vibration during and after the positioning. Wang et al. [14] proposed a robust vibration control technique for the MFC micromanipulator based on a macro stage in translational motion. They employed an asymmetric Prandtl–Ishlinskii hysteresis model in their proposed technique to capture the hysteresis nonlinearity of an MFC. They also adopted a perturbation H-infinity controller to compensate for structural uncertainty. Feng et al. [15] developed a model-independent adaptive fuzzy controller (AFC) for suppressing the vibrations of a two-link flexible manipulator system, where a pair of MFC actuators were attached to the root of each flexible link. They also demonstrated the effectiveness of the control performance of the proposed AFC using both simulations and experiments.

However, most of the studies of flexible manipulators have focused only on vibration suppression, and there is a lack of sufficient research on feedforward vibration control that is compatible with energy conservation. Thus, the present authors [16]–[18] have studied the point-to-point (PTP) control problem of mechanical systems consisting of flexible links and have proposed feedforward vibration control methods that simultaneously minimize the driving energy and residual vibration. A previous study

*Corresponding author.
Shunkodai 2-2-1-6
Asahikawa, Hokkaido, Japan
071-8142

[19] established a trajectory planning method for flexible robotic manipulators using a combination of cycloidal and polynomial functions to minimize residual vibration and operating energy simultaneously. The findings of our previous research indicated that the energy saving of flexible manipulators could be further enhanced by actively utilizing their inherent flexibility. Therefore, this paper investigates the feedforward vibration control method of a flexible manipulator with an MFC actuator, and then inquires the possibility of further energy savings from the interaction of the two actuators, a servo motor and the MFC. This paper contributes to presenting a novel energy-saving feedforward control technique for a flexible manipulator by utilizing MFC as an actuator.

2. Experimental Setup and Mathematical Model

The dimensions of the flexible manipulator treated in this study are shown in Fig. 1. A brass beam measuring 510 mm (length, l) × 65 mm (width, b) × 1 mm (thickness, h) is used as the flexible manipulator, and a piezoelectric device is attached to one side of the manipulator at 16 mm from the fixed end. An MFC (M-8557-P1) is used as the piezoelectric device, and its input voltage ranges from −500 to 1500 V.
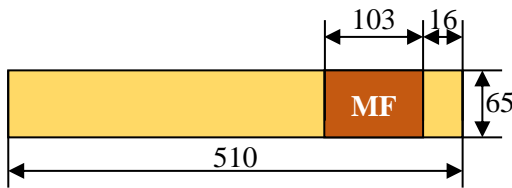
Figure 1. Schematic sketch of the flexible manipulator
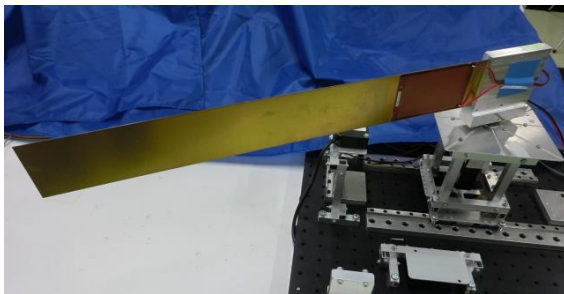
Figure 2. Photograph of the experimental setup
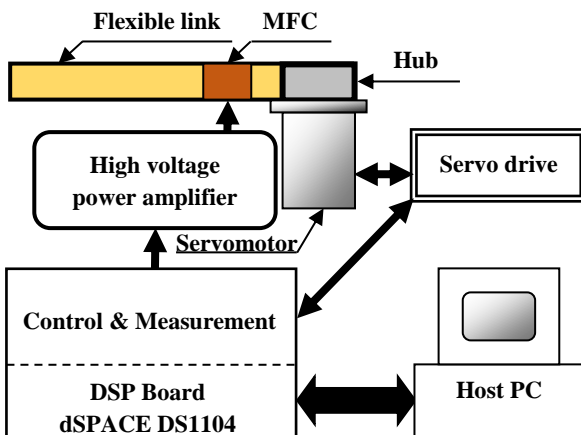
Figure 3. Schematic diagram of the experimental setup
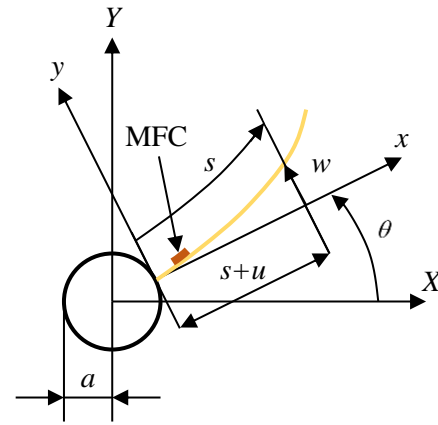
Figure 4. Coordinate systems of flexible manipulator

A photograph and schematic diagram of the experimental setup are shown in Figs. 2 and 3, respectively. Figure 4 depicts the coordinate systems of the flexible manipulator, where the radius of the rigid hub (45 mm) is denoted by a. The joint angle θ of the flexible link is actuated by an AC servomotor (YASKAWA: SGMMJ-A3EAAJ361K), which is operated in the speed control mode using a servo drive (YASKAWA: SGDJ-A3ESY32). The displacement w of the flexible manipulator is measured by attaching a strain gauge to the opposite side of the MFC. The motor torque τ is monitored using the servo drive. The MFC is driven using a power amplifier (TREK: MODEL 2220) for piezo actuators, and its drive voltage is measured from the analog monitor function of the power amplifier. Measurement and control of the experimental setup are implemented on a DSP board (dSPACE: DS1104), which has a sampling rate of 500 Hz. As shown in Fig. 4, the MFC is attached to the upper surface of the manipulator and is stretched since the displacement w is positive upward y. Consequently, the manipulator is deformed in the negative direction when a positive voltage is applied.

Based on the modeling of flexible manipulators in a previous study [16], we assume that the equations of motion are as follows:

$$\ddot{W} + 2\varsigma\omega\dot{W} + \omega^2 W + \alpha_1\ddot{\theta} + \alpha_2\dot{\theta}^2 W = -\alpha_3 u \qquad (1)$$

$$\beta_1\ddot{\theta} + \beta_2\ddot{W} + c_\theta\dot{\theta} = \tau \qquad (2)$$

where W denotes the modal amplitude of the first vibration mode, u denotes the control input from the MFC, and ζ and c_θ denote the viscous damping and friction coefficients, respectively. A dot denotes the derivative with respect to time t. Note that the flexible manipulator is approximated as a uniform beam because the thickness of the MFC is very thin (0.3 mm). The characteristic of the MFC is approximated by the following first-order system

$$\dot{u} = \beta u + v \qquad (3)$$

where v denotes the input voltage of the MFC.

Table 1. Identified parameters

Parameter	Value	Unit
α_1	2.708×10^{-1}	m
α_2	2.176×10^{-1}	-
α_3	3.062×10^{-2}	m/(Vs³)
ζ	1.366×10^{-2}	-
β_1	2.232×10^{-2}	kgm²
β_2	8.258×10^{-2}	kgm
c_θ	2.989×10^{-2}	Nms/rad
β	-83.23	1/s

Since the proposed method belongs to a feedforward controller, its performance depends on the accuracy of the controlled object. Thus, the values of the coefficients in equations (1)-(3) are determined from parameter identification experiments in order to obtain an accurate mathematical model [18]–[20]. These values are determined in the identification technique so that the simulation and experimental results are in good agreement with each other. The obtained values are listed in Table 1. The validity of the values will be shown by experimental results in a later section.

3. Feedforward Control Method

In this section, we deal with the PTP motion of the flexible manipulator and present a feedforward control technique for suppressing residual vibrations with minimum driving energy consumption.

We attempt to express the joint angle profile of the flexible manipulator as the following cycloidal function [19]

$$\theta(t) = \theta_E \left\{ U(t) - \frac{\sin[2\pi U(t)]}{2\pi} \right\}, \quad t \in [0, T_E] \quad (4)$$

where θ_E and T_E denote the target angle and traveling time of the PTP motion, respectively. The input function $U(t)$ of the cycloidal function is defined as [19]

$$U(t) = \frac{t}{T_E} + (1 - T^2) \sum_{m=1}^{M} a_m T^{m-1} \quad (5)$$

where

$$T = -1 + \frac{2t}{T_E} \quad (6)$$

The input voltage profile of the MFC is represented by using a Gaussian function:

$$v(t) = (1 - T^2) d \exp\left[-\frac{(T - c)^2}{\sigma^2} \right], \quad t \in [0, T_E] \quad (7)$$

where the definition of T is the same as in Eq. (6). Figure 5 indicates the output of Eq. (7) in a graph when $T_E = 1$, $d > 0$, $c = -1$, and $\sigma^2 = 0.1$, in which the maximum value is

normalized to 1. As shown in Fig. 5, the Gaussian function outputs a pulse-like waveform, whose voltage we will attempt to apply to the MFC in this study. The parameter c in Eq. (7) is set to $c = -3$. The value of the parameter d is adopted so that the maximum value of v is 1000 V.

The trajectory $\theta(t)$ and the input voltage profile $v(t)$ depend on the coefficients a_m in Eq. (5) and σ in Eq. (7), respectively. Hence, the coefficients need to be tuned in order to suppress the residual vibration under the saving energy. An overview of the parameter tuning method is given below.
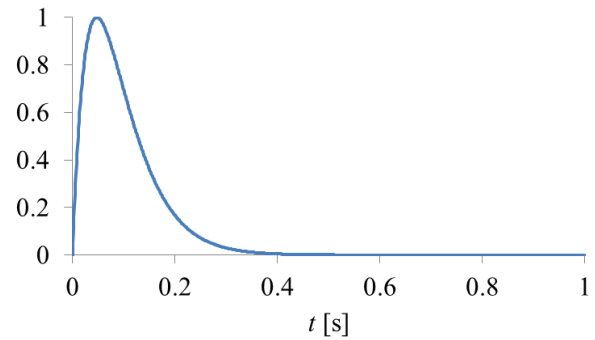

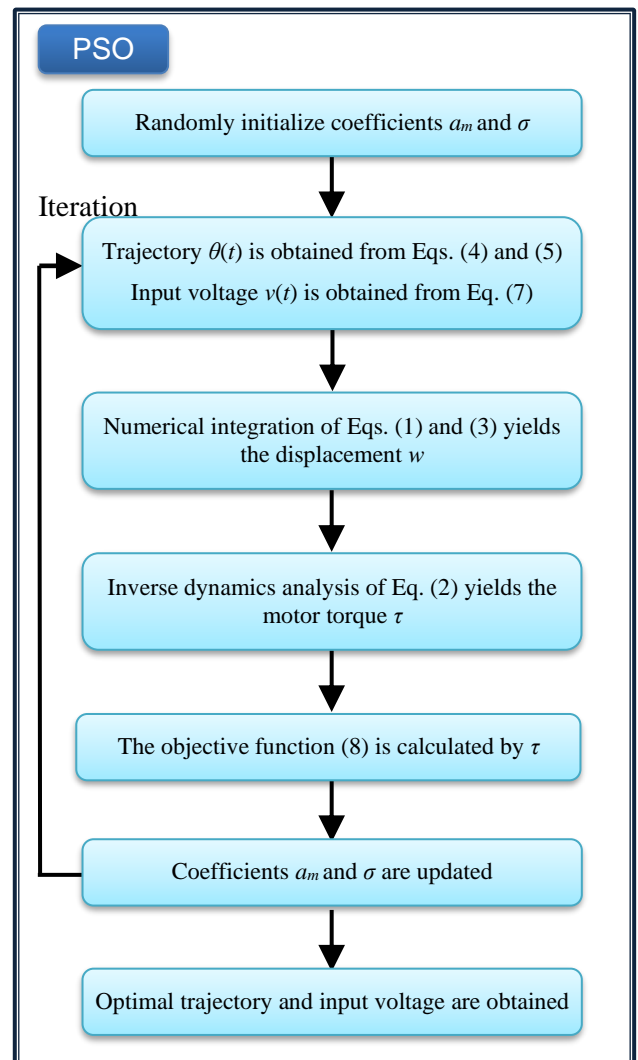
Figure 5. Shape of the Gaussian function

Figure 6. Schematic algorithm of the proposed method

Figure 6 shows the algorithm of the proposed method. First, we give a driving condition (θ_E and T_E). The coefficients a_m and σ are set as optimization parameters, and then we generate the trajectory $\theta(t)$ and the input voltage profile $v(t)$ from Eqs. (4), (5), and (7). The numerical integrations of Eqs. (1) and (3) yield the displacement w of the flexible manipulator. We then determine the motor torque τ from the inverse dynamics analysis of Eq. (2) using the obtained accelerations $\ddot{\theta}$ and $\ddot{w}$. To simultaneously minimize the residual vibration and driving energy, we define the objective function F as follows [21]:

$$F = F_1 + F_2 = \sum_{i=1}^{I} |\tau_i| + \sum_{i=I+1}^{I+J} |\tau_i| \qquad (8)$$

where τ_i denotes the torque at sampling time $\Delta t = 2$ ms and $I = (T_E+1)/\Delta t$. The function F_1 denotes the total sum of the torques until the positioning of the PTP motion. The function F_2 represents the sum of the torque for 1 s after the positioning, where $J = 1/\Delta t$. Minimization of F_1 and F_2 can suppress the driving energy and the residual vibration, respectively. The particle swarm optimization (PSO) algorithm [22] tunes the optimized parameters to minimize the objective function (8). Finally, the optimal trajectory and input voltage are obtained. Note that the residual vibration can be suppressed with energy savings when the flexible manipulator is driven using optimal trajectory and input voltage, and the proposed method belongs to the feedforward vibration control scheme.

4. Simulation and Experimental Results

Numerical simulations and experiments are performed to verify the validity of the proposed energy-saving feedforward vibration control method. The below simulations involve 50 particles and 400 iterations (maximum) in the PSO algorithm. The number of terms in Eq. (5) is adopted as $M = 6$, and the ranges of the optimization parameters are defined as

$$\begin{aligned} a_m &\in [-0.2, 0.2], (m = 1, 2, \cdots, 6) \\ \sigma^2 &= 10^{-q}, q \in [-1, 0] \end{aligned} \right\} \qquad (9)$$

Figure 7 shows a comparison of the simulation results obtained by the present method and a cycloidal motion, in which the driving condition is set as $\theta_E = -\pi/4$ rad and $T_E = 1.0$ s. The cycloid motion is obtained as $U(t) = t/T_E$ in Eq. (4). Here, note that the MFC is not driven for the results of the cycloid motion. The time histories of the joint angle, angular velocity, tip displacement, input voltage, and motor torque are depicted in Figs. 7 (a)–(e), respectively. The cycloidal motion induces the residual vibration after the positioning ($t > 1$ s), and this residual vibration causes torque to keep the joint angle at the target angle θ_E, as shown in Fig. 7 (e). After the positioning, the vibration and torque are perfectly canceled in the present method. Thus, this indicates that the proposed method, which is based on minimizing the drive torque defined in Eq (8), can suppress the residual vibration.

Figure 7. Comparison of simulation results obtained using the present method and a cycloidal motion ($T_E = 1.0$ s and $\theta_E = -\pi/4$ rad): (a) joint angle, (b) angular velocity, (c) tip displacement, (d) input voltage, and (e) motor torque

Figure 8 illustrates a comparison of the simulation and experimental results obtained by the present method, where the driving conditions are the same as in Fig. 7. As shown in the figure, the simulation and experimental results are in good agreement with each other, thus validating the modeling of the flexible manipulator with the MFC. As shown in Fig. 8 (b) that depicts the time history of tip displacement, the proposed method also suppresses the residual vibration in the experiment. This confirms the effectiveness and feasibility of the feedforward vibration control technique through the simultaneous optimization of the two actuators. For comparison, the results obtained by the previous study [19], in which the trajectory of the joint angle is only optimized without using the MFC, are shown in Fig. 9. As shown in this figure, residual vibration suppression can be achieved in both simulation and experiment. Figure 10 presents a comparison of the simulation results obtained by the present and previous studies shown in Figs. 8 and 9, respectively. Figures 10 (a) and 10 (b) indicate tip displacement and motor torque, respectively. As shown in Fig. 10 (a), the maximum value of displacement at $t = 0.18$ s in the present study is less than that in the previous study [19]. This reduction in the maximum displacement is caused by MFC actuation whose input voltage has a peak at around $t = 0.25$ s as shown in Fig. 8 (d). Due to this

113

deformation suppression effect, the maximum value of the torque is also slightly lower in the present method than in the previous study [19].

Regarding the energy-saving effect of the present method, Table 2 shows a comparison of the driving energy calculated by the experimental data under three driving conditions ($\theta_E = -\pi/4$ rad and $T_E = 0.9$ s), ($\theta_E = -\pi/4$ rad and $T_E = 1.0$ s), and ($\theta_E = -\pi/2$ rad and $T_E = 1.1$ s). The values in parentheses are obtained from the simulation results. The driving energy *Ene* is defined as follows:

$$Ene = \int_0^{\theta_E} |\tau| \, d\theta \tag{10}$$

The vibration control performance of both methods was also checked under driving conditions ($\theta_E = -\pi/4$ rad and $T_E = 0.9$ s) and ($\theta_E = -\pi/2$ rad and $T_E = 1.1$ s). The time history data comparing simulation results with experimental results are presented in the Appendix. The experimental results tend to have larger values than the simulation results probably due to the frictions of the motor, which are not considered in the mathematical model. As demonstrated in Table 2, under all drive conditions, the values for the present method are smaller than those for the previous method, and the energy-saving effect of the proposed method can be confirmed by actuating the MFC. On the other hand, the driving energy of the MFC is not considered, as shown in Eq. (10). Figure 11 shows the displacement obtained from the simulation when the joint angle of the manipulator is fixed, and the input voltage shown in Fig. 7 (d) is applied to the MFC. By using this displacement data, the driving energy of the MFC can be calculated from the maximum potential energy as follows:

$$U_{\max} = \max\left[\frac{EI}{2} \int_0^l \left(\frac{\partial^2 w}{\partial s^2} \right)^2 \right] \tag{11}$$

where *EI* represents the flexural rigidity of the flexible manipulator. Note that the maximum amplitude of the tip displacement is only about 0.8 cm and the calculated energy of the MFC is about 1×10^{-4} J, which is significantly less than that of the motor and can be ignored. Therefore, this finding shows that the proposed method enables further energy savings under residual vibration suppression.

Figure 9. Comparison of simulation and experimental results obtained using the previous method ($T_E = 1.0$ s and $\theta_E = -\pi/4$ rad): (a) angular velocity, (b) tip displacement, and (c) motor torque

Figure 8. Comparison of simulation and experimental results obtained using the present method ($T_E = 1.0$ s and $\theta_E = -\pi/4$ rad): (a) angular velocity, (b) tip displacement, (c) input voltage, and (d) motor torque
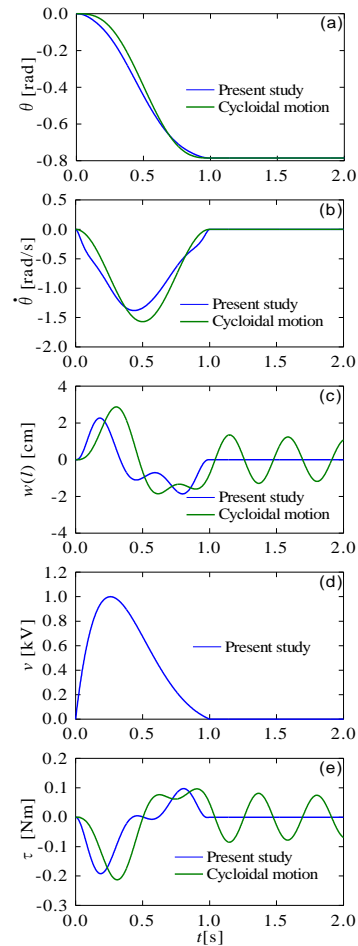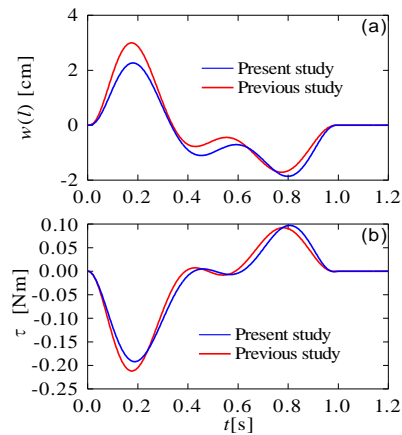

Figure 10. Comparison of simulation results obtained using the present method and the previous method ($T_E = 1.0$ s and $\theta_E = -\pi/4$ rad): (a) tip displacement and (b) motor torque

Table 2. Comparison of driving energy *Ene* [J]

θ_E [rad]	T_E [s]	Present study	Previous study [19]
$-\pi/4$	0.9	5.85×10^{-2} (5.28×10^{-2})	6.23×10^{-2} (5.64×10^{-2})
$-\pi/4$	1.0	5.09×10^{-2} (4.41×10^{-2})	5.35×10^{-2} (4.63×10^{-2})
$-\pi/2$	1.1	1.60×10^{-1} (1.53×10^{-1})	1.73×10^{-1} (1.64×10^{-1})
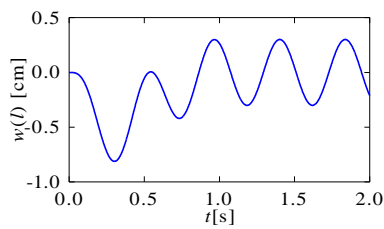
Figure 11. Tip displacement calculated using the input voltage of MFC shown in Fig. 7 (d) when the joint angle is fixed

5. Summary

This study examined the PTP control problem of a flexible manipulator that consists of two actuators, a servo motor and MFC, and proposed a novel energy-saving feedforward control technique. Simulation and experimental results revealed that simultaneous optimization of the input voltage of MFC and the trajectory of the joint angle is more energy-saving than only optimization of the trajectory of the joint angle. To the best of our knowledge, this study presents a novel finding that the driving energy of a flexible manipulator can be reduced by utilizing deflection due to an MFC during a PTP motion.

References

[1] M. Benosman and G. L. Vey, "Control of flexible manipulators: A survey," *Robotica*, vol. 22, no. 5, pp. 533–545, 2004.

[2] S. K. Dwivedy and P. Eberhard, "Dynamic analysis of flexible manipulators, a literature review," *Mech. Mach. Theory*, vol. 41, no. 7, pp. 749–777, 2006.

[3] H. N. Rahimi and M. Nazemizadeh, "Dynamic Analysis and Intelligent Control Techniques for Flexible Manipulators: A Review," *Adv. Robot.*, vol. 28, no. 2, pp. 63–76, 2014.

[4] C. T. Kiang, A. Spowage, and C. K. Yoong, "Review of Control and Sensor System of Flexible Manipulator," *J. Intell. Robot. Syst.*, vol. 77, no. 1, pp. 187–213, 2015.

[5] K. Lochan, B. K. Roy, and B. Subudhi, "A Review on Two-Link Flexible Manipulators," *Annu. Rev. Control*, vol. 42, pp. 346–367, 2016.

[6] E. A. Alandoli and T. Lee, "A Critical Review of Control Techniques for Flexible and Rigid Link Manipulators," *Robotica*, vol. 38, no. 12, pp. 2239–2265, 2020.

[7] R. Rimašauskienė, V. Jūrėnas, M. Radzienski, M. Rimašauskas, and W. Ostachowicz, "Experimental analysis of active–passive vibration control on thin-walled composite beam," *Compos. Struct.*, vol. 223, p. Article 110975, 2019.

[8] J. Gawryluk, A. Mitura, and A. Teter, "Dynamic control of kinematically excited laminated, thin-walled beam using macro fibre composite actuator," *Compos. Struct.*, vol. 236, p. Article 111898, 2020.

[9] X. Wanga, W. Zhoub, Z. Zhanga, Jianga, and Z. Wu, "Theoretical and Experimental Investigations on Modified LQ Terminal Control Scheme of Piezo-Actuated Compliant Structures in Finite Time," *J. Sound Vib.*, vol. 491, p. Article 115762, 2021.

[10] J. Zhou, J. Zhou, W. Chen, J. Tian, J. Shen, and P. Zhang, "Macro Fiber Composite-Based Active and Efficient Suppression of Low-Frequency Vibration of Thin-Walled Composite Beam," *Compos. Struct.*, vol. 299, p. Article 116019, 2022.

[11] G. Zhiyuan, W. Yiru, S. Muyao, and Z. Xiaojin, "Theoretical and Experimental Investigation Study of Discrete Time Rate-Dependent Hysteresis Modeling and Adaptive Vibration Control for Smart Flexible Beam with MFC Actuators," *Sensors Actuators A Phys.*, vol. 344, p. Article 109332, 2022.

[12] Q. Lu, P. Wang, and C. Liu, "An Analytical and Experimental Study on Adaptive Active Vibration Control of Sandwich Beam," *Int. J. Mech. Sci.*, vol. 232, p. Article 107634, 2022.

[13] Y. L. Yang, Y. D. Wei, J. Q. Lou, L. Fu, S. Fang, and T. H. Chen, "Dynamic Modeling and Adaptive Vibration Suppression of a High-Speed Macro-Micro Manipulator," *J. Sound Vib.*, vol. 422, pp. 318–342, 2018.

[14] S. Wang, Y. L. Yang, G. P. Li, H. L. Du, and Y. D. Wei, "Microscopic Vibration Suppression for a High-Speed Macro-Micro Manipulator with Parameter Perturbation," *Mech. Syst. Signal Process.*, vol. 179, p. Article 109332, 2022.

[15] C. Feng, W. Chen, M. Shao, and S. Ni, "Trajectory Tracking and Adaptive Fuzzy Vibration Control of Multilink Space Manipulators with Experimental Validation," *Actuators*, vol. 12, p. 138, 2023.

[16] A. Abe and K. Komuro, "Minimum Energy Trajectory Planning for Vibration Control of a Flexible Manipulator Using a Multi-Objective Optimization Approach," *Int. J. Mechatronics Autom.*, vol. 2, no. 4, pp. 286–294, 2012.

[17] A. Abe and S. Nemoto, "An Energy Saving Feedforward Control Technique for a 2-DOF Flexible Manipulator (in Japanese)," *Trans. Japan Soc. Mech. Eng. Ser. C*, vol. 78, pp. 1325–1337, 2012.

[18] A. Abe, "Minimum Energy Trajectory Planning Method for Robot Manipulator Mounted on Flexible Base," in *Proceeding of 9th Asian Control Conference*, 2013, pp. 1–7.

[19] A. Abe, "An Effective Trajectory Planning Method for Simultaneously Suppressing Residual Vibration and Energy Consumption of Flexible Structures," *Case Stud. Mech. Syst. Signal Process.*, vol. 4, pp. 19–27, 2016.

[20] A. Abe, "Trajectory Planning for Flexible Cartesian Robot Manipulator by Using Artificial Neural Network: Numerical Simulation and Experimental Verification," *Robotica*, vol. 29, no. 05, pp. 797–804, 2011.

[21] A. Abe, "Trajectory Panning of a Flexible Manipulator Based on Driving Torque (in Japanese)," *Trans. Japan Soc. Mech. Eng. Ser. C*, vol. 74, pp. 2246–2253, 2008.

[22] M. Clerc and J. Kennedy, "The Particle Swarm-Explosion, Stability, and Convergence in a Multidimensional Complex Space," *IEEE Trans. Evol. Comput.*, vol. 6, no. 1, pp. 58–73, 2002.

Appendix A. Experimental validation

Figures A1–A4 present a comparison of simulation and experimental results obtained using the present and previous methods under the driving conditions ($\theta_E = -\pi/4$ rad and $T_E = 0.9$ s) and ($\theta_E = -\pi/2$ rad and $T_E = 1.1$ s). As shown in Figs. A1–A4, the experimental results are in good agreement with the simulation results. We also demonstrate that the proposed feedforward vibration control technique is effective and feasible.
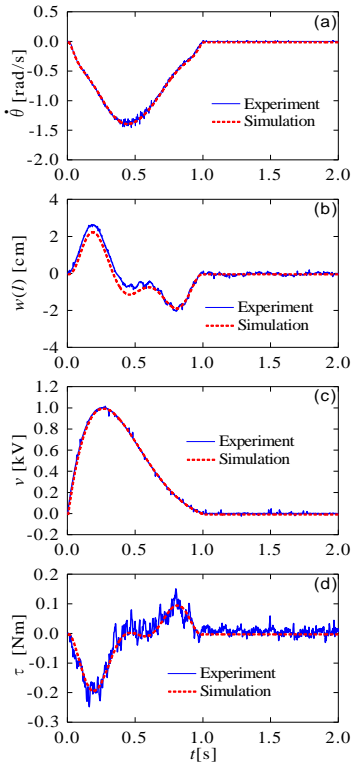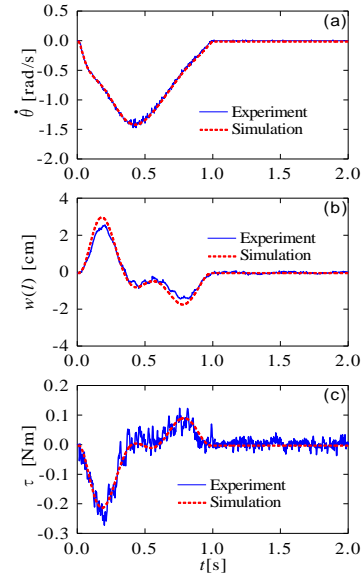
Figure A1. Comparison of simulation and experimental results obtained using the present method ($T_E = 0.9$ s and $\theta_E = -\pi/4$ rad): (a) angular velocity, (b) tip displacement, (c) input voltage, and (d) motor torque.


\Fig. A3 Comparison of simulation and experimental results obtained using the present method ($T_E = 1.1$ s and $\theta_E = -\pi/2$ rad): (a) angular velocity, (b) tip displacement, (c) input voltage, and (d) motor torque.

Fig. A2 Comparison of simulation and experimental results obtained using the previous method ($T_E = 0.9$ s and $\theta_E = -\pi/4$ rad): (a) angular velocity, (b) tip displacement, and (c) motor torque.
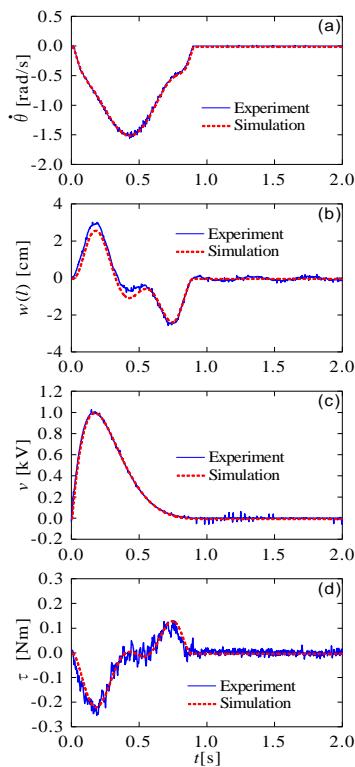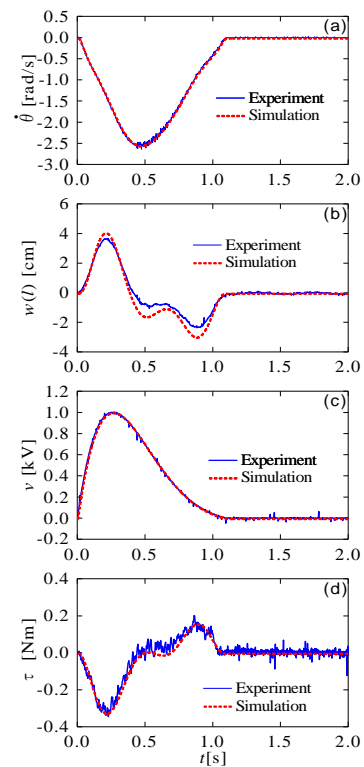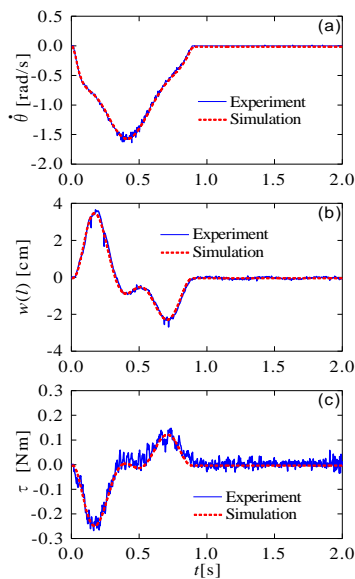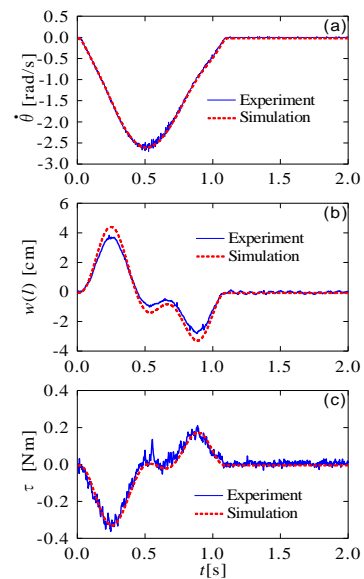

Fig. A4 Comparison of simulation and experimental results obtained using the previous method ($T_E = 1.1$ s and $\theta_E = -\pi/2$ rad): (a) angular velocity, (b) tip displacement, and (c) motor torque.

Development of A Presence System for Students using QR Code Based on Android Application

Mar'atuttahirah[a,*], Mardhiyyah Rafrin[b], Mahdaniar[c], Putri Ayu Maharani[d]

[a]Department of Information System, Institut Teknologi B.J. Habibie. Email: maratuttahirah.ir@ith.ac.id
[b]Department of Computer Science, Institut Teknologi B.J. Habibie. Email: rafrinmardhiyyah@ith.ac.id
[c]Department of Informatics and Computer Engineering Education, Universitas Negeri Makassar. Email: mahdaniarnasar19@gmail.com
[d]Department of Computer Science, Institut Teknologi B.J. Habibie. Email: maharani_putriayu@ith.ac.id

Abstract

The Department of Information System at Institut Teknologi B.J. Habibie still physically records each student's attendance by having them sign a presence sheet for each course. Due to the ease with which fraudulent signatures can be used to manipulate the traditional system, there may be some issues. Additionally, manual presence recapitulation takes more time and could be less precise and effective. This research aims to develop a prototype of Android-based application of student presence system with QR Code technology in the Department of Information System, Institut Teknologi B.J. Habibie. Following the creation of the presence system prototype, ISO 25010 quality standards were used to evaluate the application. The criteria evaluated are functionality, usability, portability, performance efficiency, and security. The application's functionality was tested by two system experts by using Guttman Scale and it gained 100% yes answer. The usability was tasted from 30 users rating the application usability through a survey using Likert Scale, it achieved the average percentage of positive answers is 91%. The performance efficiency was classified as grade A by *GTmetrix* testing site. Similarly, the security system tested by *sslabs.com* achieved grade A. Furthermore, the portability was tested by using 4 different web browsers for the web version and by installing the application on 4 different smartphones and they showed no errors. Based on the overall assessment result, the Android-based Student Presence System is feasible, efficient, suitable and secure.

Keywords: Android; functionality; portability; presence system; QR Code

1. Introduction

In higher education, the lecture/teaching process is carried out using various methods based on the standards set by the Directorate General of Higher Education as well as by the institution itself. The lectures are an advanced learning process and the presence of students is very important to support the continuity of the teaching and learning process. The students attending lectures are recorded and sometimes it become additional assessments to determine the student grades. In addition, student and lecturer presence system can also be the information about how the student's or lecture's discipline is concerned [1].

Presence refers to the ability to create a learning environment and atmosphere that enables learners to communicate in a friendly and supportive environment, and demonstrate true social and emotional expression capabilities [2]. For presence detection, using multiple technologies, it's very hard to converge and a single platform is not available yet [3]. The old presence system is prone to misuse and data manipulation, so it is necessary

to develop a new presence system based on smartphones [4].

Presence system is one of the important components in the lecture process and student attendance recap is one of the elements in various aspects of lecture assessment. Presence has been carried out by signing students. The use of telecommunications technology which is now growing rapidly is the smartphone where one of the operating systems used in smartphones is the Android operating system, Android provides an open platform for users to create their own applications that have been used if various mobile devices [5].

Presence system is a crucial process in campus that involve students [6]. Presence system for a fairly number of participants, this situation is a wasting of time as well as reduces convenience for participants [7].

The technology is currently developing very fast wherein the industrial era 4.0 all activities can be connected and accessed by using the internet and smartphone [8].

With the advent of new mobile technologies, the Mobile application industry is advancing rapidly. Consisting of several operating systems like Symbian OS, iOS, blackberry, etc., Android OS is recognized as the most widely used, popular and user-friendly mobile

*Corresponding author. Tel.: +62-813-4052-6411
Jl. Balai Kota No.1, Kota Parepare
Sulawesi Selatan, Indonesia
91122

platform. This open-source Linux kernel-based operating system offers high flexibility due to its customization properties making it a dominant mobile operating system. Android applications are programmed in java language. Google android SDK delivers a special software stack that provides developers an easy platform to develop android applications. Moreover, developers can make use of existing java IDEs which provides flexibility to the developers. Java libraries are predominant in the process of third-party application development. Cross-platform approaches make sure that developers do not have to develop platform-dependent applications. With the help of these approaches, an application can be deployed to several platforms without the need for changes in coding [9].

A Quick Response (QR) code is a two-dimensional barcode of black and white squared modules that is traditionally used for inventory tracking. QR Code technology is also used as a media to store student attendance data. QR Code is a medium used to store information quickly and get fast response without manually inputting by typing. The information encoded in the QR Code can be in the form of a URL, telephone number, SMS message, V-Card, or any text. The use of the QR Code is easily scanned and the data can be directly identified [10]. QR codes are being used increasingly to share data for different purposes. In information communication, QR code is important because of its high data capacity [11].

After direct observation of the Department of Information System, Institut Teknologi B.J. Habibie, one of the problems found related to the student presence process is that practice was still done manually by using signatures on the absence sheet for each course. Carrying out manual presence may ease the students to manipulate the presence by writing down the name of a friend listed in the course (entrust presence) who is actually absent. In addition, manual presence requires time to recapitulate the presence of students and lecturers, and it becomes less effective and less accurate.

Due to the problematic implementation of manual presence in this modern era, therefore an innovative technology system development is needed. One of technological developments that can be utilized is QR code. The QR code is used as presence method that is directly integrated with the presence system in the Department of Information System, Institut Teknologi B.J. Habibie which validate and recapitulate student presence more accurately and more effectively.

2. Proposed Method

The prototype of the developed model in this study, as shown in Fig. 1. The initial stage in this research was gathering needs which was carried out by direct observation and interviews in the department of Information System, Institut Teknologi B.J. Habibie.
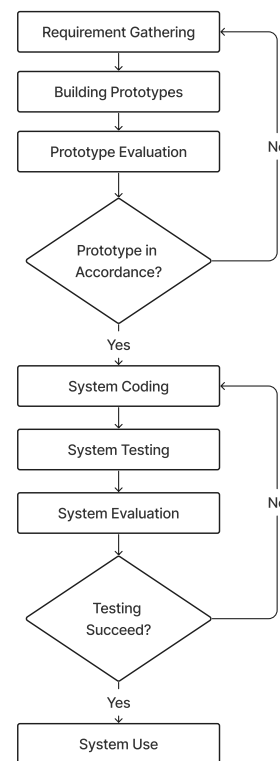
Figure 1. Stages of the prototyping method

The correspondences of the interview were the staffs/admins in the Department Information System. The aim was to collect information about current presence system and its obstacles as well as to gather required data to the presence system such as the list of students, the lecturers, the courses of the Information System program.

The second stage of this research is to build the prototype. This is done by creating a simple design consisting of flowcharts and activity diagrams.

2.1. Flowchart

One of the flowcharts in this study is the admin flowchart, as shown in Fig. 2.

2.2. Activity Diagram

The activity diagram in this study, as shown in Fig. 3.
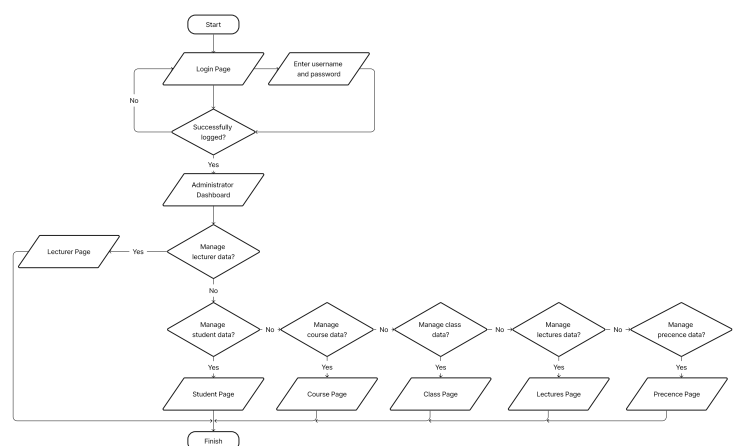
Figure 2. Admin flowchart
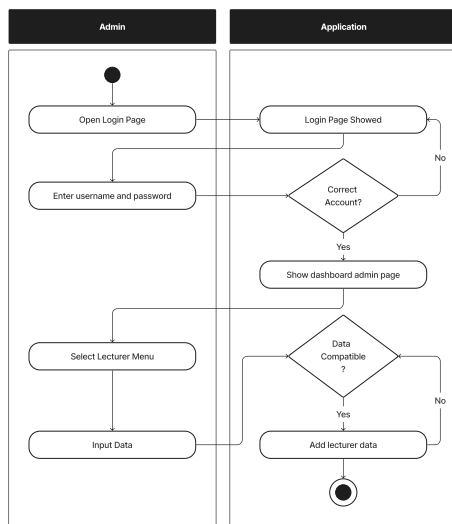
Figure 3. Activity diagram

The third stage is the evaluation of the prototype. In this stage, the client and developer identify the format that has been made according to the needs as a whole, including the software to be used and the features to be made. If the software developed is appropriate then it would be proceeded to the next stage, otherwise the prototype stage will be repeated from the first stage.

The fourth stage is the system coding. In this stage, the prototype that has been mutually agreed upon will then be translated into PHP programming language for web application and into Dart programming language for mobile application. Other technologies used are Laravel as the framework for web version, Fluter framework as the framework for mobile, MySQL as the database and Visual Studio Code as a code editor.

The final stage is the application testing using the indicator feasibility test based on ISO 25010 to fulfill several criteria. These criteria are the functionality, the usability, the portability, the performance efficiency and the security system. The ISO/IEC 25010 software quality model is an international standard for assessing software quality from two points of view which are the quality in using the application and the product quality [12].

2.3. Data analysis technique

2.3.1. Guttman scale

Guttman Scale is used to rate each feature. Guttman scale is a type of scale to get clear (firm) and consistent answers, usually the answers are yes-no or success-failure or true-false. The answer to this test can be in the form of a tick with an assessment of 1 as the highest value and 0 as the lowest value. The test cases are tested by 2 system experts [13]. Then the results of the test are calculated by [14].

Table 1. Guttman scale

Answer	Score by validator	
	Validators 1	Validators 2
Yes	-	-
No	-	-
Total	-	-

Table 2. Likert scale

Answer	Score
Strongly agree	5
Agree	4
Somewhat Disagree	3
Disagree	2
Strongly Disagree	1

Presentation for all grades is:

$$Yes = (\sum \frac{Score}{Item\ Question}) \times 100 \qquad (1)$$

2.3.2. Likert scale

The application usability is assessed through a survey of user's attitudes, opinions and perceptions by using Likert scale. This scale is ranging of 5 options that had gradations from very positive to very negative, namely strongly agree (SS), agree (A), somewhat disagree (SD), disagree (D), and strongly disagree (StD) [15]. The scale of the options can be seen in the Table 2.

The result of this survey is collected and accumulated. Only percentage of strongly-agree answer is counted and considered to scale the usability of the application. This percentage is described in the Table 3.

3. Experimental and Results

The result of this study is a development system by utilizing QR code technology. The QR code is used as presence method that is directly integrated with the Android presence system in the Department of Information System, Institut Teknologi B.J. Habibie.

This section presents the system interface design and the system testing result.

3.1. The system interface design

The followings are the interface design of each page of the system.

3.1.1. Login page

This page displays the application logo and application name as well as the login form. Users (students) are given access to the system by entering their registered student number (NIM) as the initiate username as well as the password.

3.1.2. Aplication main menu

The page that appears after the user (students) successfully login is the page of the application main menu where 4 menu options in the form of buttons are displayed. The first button is to start presence, the second button is to view the presence history, the third is about menu, and the last is an exit button to end the access to this application.

Table 3. The Scale of Likes

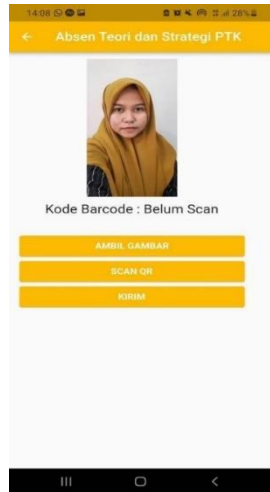| Percentage (%)	Score
81-100%	Very satisfied
61-80%	Satisfied
41-605	Neutral
21-40%	Dissatisfied
<21%	Very dissatisfied

Figure 4. Course schedule page

Figure 5. Image capture page

3.1.3. Course schedule page

The course schedule page is the page that shows the information about courses currently being held. Below the information, there is a take-a-picture button to take a real photo selfie. The course schedule page is shown in Fig. 4.

3.1.4. Image capture page

This page is used to take a selfie photo using cellphone's camera. This page will not allow students to upload a photo from the phone gallery.

The image capture page, as shown in Fig. 5. Beside taking photos, the page provides a button to scans the QR code of the course that is currently conducted. A barcode is displayed before the class so the student can scan the barcode from the presence application in their phone.

The example of the barcode and QR code scanning page, as shown in Fig. 6.
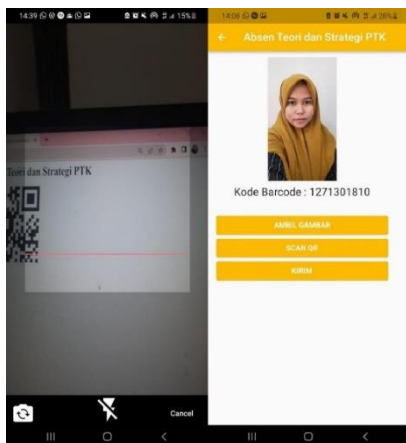
Figure 6. Scan QR code page

Table 4. System expert testing results

Answer	Score by validator	
	Validators 1	Validators 2
Yes	73	73
No	-	-
Total	100%	100%

After successfully scanning the barcode, the page will return to the main page and at the bottom of the page there will be a message to notify the user that the system successfully records their presence.

3.2. System testing

The entire system will be tested based on the software quality standards at ISO 25010 standard with four aspects: functionality, usability, portability, performance efficiency and security. Then the user will give feedback which will be used to improve system requirement specifications. The followings describe the testing result of each aspect.

3.2.1. Functionality testing

The functionality test instrument consists of 73 statements related to the functions developed into the system. Each function was assessed by 2 (two) system experts. The summary of the functionality testing results by the experts are shown in the Table 4.

Based on the calculations in the Table 4 above, the score of the yes answer is > 50% so that the system can be accepted or considered appropriate and therefore, it is fulfilled the functionality aspects.

3.2.2. Usability testing

This testing is done through a survey using Likert Scale to collect users' response regarding the student presence application. From over 30 respondents, the average percentage of strongly agree answers was 91%. This number showed that the application usability is very satisfied based on the scale of likes.

3.2.3. Portability testing for the web version

Portability testing for the web version was done by using a web browser testing tool called browserstack.com. This tool supports cross browser testing. In this test, 4 different types of browsers were used and analyzed. The results of the portability testing can be seen in the following Table 5.

Table 5. Portability Testing Result for The Web Application

No.	Browser type	Type	Operating system	Hasil
1	Microsoft Edge	Desktop	Windows 11	No errors found
2	Mozilla Firefox	Desktop	Windows 11	No errors found
3	Opera Browser	Desktop	Windows 11	No errors found
4	Google Chrome	Desktop	Windows 11	No errors found

Table 6. Portability testing result for the mobile application

No.	Device type	Android Version	Installation process	Application Running process
1	Smartphone Samsung J7 Pro	9	Succeed	Runs fine without any glitches
2	Smartphone Vivo Y33S	12	Succeed	Runs fine without any glitches
3	Smartphone Samsung A50S	11	Succeed	Runs fine without any glitches
4	Smartphone Vivo 1820	8.1.	Succeed	Runs fine without any glitches

3.2.4. Portability testing for the mobile applications

In order to perform this testing, the application was installed on 4 (four) smartphones with different specifications of hardware and different versions of the Android OS. The results of the testing are shown in the Table 6.

3.2.5. Performance efficiency

Performance efficiency testing was carried out by utilizing a site called GTmetrix. The following figure is the result obtained from performance efficiency testing using GTmetrix. The image performance efficiency, as shown in Fig. 7.

Figure 7 shows the performance efficiency using GTmetrix is 93% and the structure is 95%. The load time is much faster or only 1.6 seconds (load time must be less than 10 seconds). The grade A category in the testing result proves that the performance efficiency is excellent.

3.2.6. Security testing

This test was carried out using a web security testing tool named sslabs.com and the results, as shown in Fig. 8.
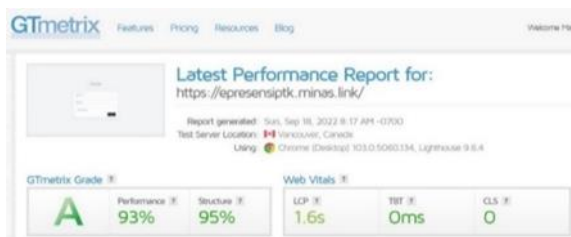

Figure 7. Performance efficiency

Figure 8. Security testing results using *sslabs*

Based on the result, the security grade is A, indicating that the presence system developed is stated very well in terms of security system.

4. Conclusions

Based on the results of research, the development of presence system for students using QR Code on Android OS was created using a prototype development model. This presence system is an application for students to take presence without having to record on a sheet of paper manually. This system is developed using Dart programming language with Flutter framework for mobile application and PHP, HTML, and CSS with Laravel framework for the web application.

The application was assessed based on ISO 25010 on 5 criteria. They are the functionality, the usability, the portability, the performance efficiency and the security system. A variety of testing tools and human evaluation were used to assess the system's quality while examining its functionality, performance efficiency, security, and portability. The application's functionality was tested by two system experts by using Guttman Scale and it gained 100% yes answers over 73 test cases. The usability was tasted from 30 users rating the application usability through a survey using Likert Scale, it indicated that the application is very satisfied with the average percentage of positive answers is 91%. The performance efficiency was classified as grade A by *GTmetrix* testing site. Similar to the security system tested by using sslabs.com testing site, the application achieved an A grade too. Furthermore, the portability was tested for both web and mobile version. For the web version, 4 different browsers were used with the help of browserstack.com testing site and no error was found. This result was as satisfied as the mobile version result which installed on four different smartphones. Based on the overall assessment result, the Android-based Student Presence System is feasible, efficient, suitable and secure. Therefore, it can be developed and implemented in the Department of Information System, Institut Teknologi B.J. Habibie.

References

[1] R. Arif, "Design and Development of Presence System for Students Using QR Code Technology Based on Android," *J. Ilm. Elektron. DAN Komput. Vol14 No1 Juli 2021 Pp 47 - 58*, vol. 14, no. 1, p. 12, 2021. [in Bahasa]

[2] Honghua wenyu, "The Presence Design of Online Teaching based on CoI Models," in *2020 IEEE 2nd International Conference on Computer Science and Educational Informatization (CSEI)*, Xinxiang, China: IEEE, 2020. doi: 10.1109/CSEI50228.2020.9142498.

[3] S. Sidhardhan, D. Das, and K. Park, "Intelligent Human Presence Detection and Identification," in *2020 International Conference on Computer Communication and Informatics (ICCCI)*, Coimbatore, India: IEEE, Jan. 2020, pp. 1–6. doi: 10.1109/ICCCI48352.2020.9104178.

[4] F. K. Chuah and S. S. Teoh, "Thermal Sensor based Human Presence Detection for Smart Home Application," in *2020 10th IEEE International Conference on Control System, Computing and Engineering (ICCSCE)*, Penang, Malaysia: IEEE, Aug. 2020, pp. 37–41. doi: 10.1109/ICCSCE50387.2020.9204940.

[5] N. Nandang, "Implementation of QR Code and Imei on Android and Web-Based Student Presence Systems," in *2020 IEEE 2nd International Conference on Computer Science and Educational*

Informatization (CSEI), Xinxiang, China: IEEE, 2020. doi: 10.1109/ICITISEE.2018.8721009.

[6] M. Abdurohman, D. T. Murdiansyah, J. Halomoan, and Estananto, "Secure Smart Card Reader for University Presence System," in *2018 Third International Conference on Informatics and Computing (ICIC)*, Palembang, Indonesia: IEEE, Oct. 2018, pp. 1–5. doi: 10.1109/IAC.2018.8780545.

[7] M. S. Qusyairi, M. Abdurohman, and A. Mulyana, "Seamless Presence System in Classroom," 2017.

[8] A. S. Shahab and R. Sarno, "Android Application for Presence Recognition based on Face and Geofencing," in *2020 International Seminar on Application for Technology of Information and Communication (iSemantic)*, Semarang, Indonesia: IEEE, Sep. 2020, pp. 208–213. doi: 10.1109/iSemantic50169.2020.9234253.

[9] A. Sarkar, A. Goyal, D. Hicks, D. Sarkar, and S. Hazra, "Android Application Development: A Brief Overview of Android Platforms and Evolution of Security Systems," in *2019 Third International conference on I-SMAC (IoT in Social, Mobile, Analytics and Cloud) (I-SMAC)*, Palladam, India: IEEE, Dec. 2019, pp. 73–79. doi: 10.1109/I-SMAC47947.2019.9032440.

[10] K. Pena-Pena and G. R. Arce, "Channel Coding Optimization for Visually Pleasant QR Codes : Invited Presentation," in *2019 53rd Annual Conference on Information Sciences and Systems (CISS)*, Baltimore, MD, USA: IEEE, Mar. 2019, pp. 1–4. doi: 10.1109/CISS.2019.8692837.

[11] Md. S. Ahamed and H. Asiful Mustafa, "A Secure QR Code System for Sharing Personal Confidential Information," in *2019 International Conference on Computer, Communication, Chemical, Materials and Electronic Engineering (IC4ME2)*, Rajshahi, Bangladesh: IEEE, Jul. 2019, pp. 1–4. doi: 10.1109/IC4ME247184.2019.9036521.

[12] F. H. Wattiheluw, S. Rochimah, C. Fatichah, and K. Z. Abidin, "Development of a Quality Model Based on ISO 25010 Using Fuzzy and PSO for E-commerce Websites," in *2020 17th International Conference on Electrical Engineering/Electronics, Computer, Telecommunications and Information Technology (ECTI-CON)*, Phuket, Thailand: IEEE, Jun. 2020, pp. 250–254. doi: 10.1109/ECTI-CON49241.2020.9158323.

[13] L. Yulia and W. Setianingsih, "Studies of Online Marketing Manajemen (Case on SMEs of Furniture Production in Tamansari Babakan Muncang I, Tasikmalaya City," vol. 9, no. 1, 2020. [in Bahasa]

[14] S. N. Asmah and D. Setyowati, "Analysis of Student Responses to Online Learning in Mathematics at SD Negeri 29 Sanggau," 2022. [in Bahasa]

[15] H. Hornbeck and U. Alim, "UofC-Bayes: A Bayesian Approach to Visualizing Uncertainty in Likert Scales," in *2019 IEEE Conference on Visual Analytics Science and Technology (VAST)*, Vancouver, BC, Canada: IEEE, Oct. 2019, pp. 130–131. doi: 10.1109/VAST47406.2019.8986935.

Effect of Mg and Zn Composition Variations on Surface Characteristics and Flexural Strength of Biodegradable Mg-Zn-Ca Alloys by Powder Metallurgy Method

Yuliana Simons[a], Onny S. Sutresman[b], Hairul Arsyad[c,*]

[a]Mechanical Engineering Department, Physic Metallurgy Laboratory, Faculty Engineering, Hasanuddin University.
  Email: Yulianasimons86@gmail.com
[b]Mechanical Engineering Department, Physic Metallurgy Laboratory, Faculty Engineering, Hasanuddin University.
  Email: Onny.sutresman@gmail.com
[c]Mechanical Engineering Department, Physic Metallurgy Laboratory, Faculty Engineering, Hasanuddin University.
  Email: arsyadhairul@yahoo.com

Abstract

This study aims to determine the Mg-Zn-Ca alloy's surface characteristics and flexural strength using powder metallurgy methods. The Mg-Zn-Ca alloy was prepared by powder metallurgy method with three composition variations (89Mg-10Zn-1Ca, 93Mg-6Zn-1Ca and 97Mg-2Zn-1Ca). The Mg-Zn-Ca powder alloy was mixed with the dry milling process for 60 minutes. After mixing, the compaction process is carried out with a load of 200 MPa. Then, the sintering process was carried out at a temperature of 500 °C and held for 3 hours with a furnace fed with argon gas. The sintering results were characterized by the microstructure of the Mg-Zn-Ca alloy using SEM and XRD. After that, it was carried out to test the flexural strength of the Mg-Zn-Ca alloy. SEM results obtained that the 89Mg-10Zn-1Ca alloy sample has less porosity and a smaller pore diameter compared to the 93Mg-6Zn-1Ca alloy sample and the 97Mg-2Zn-1Ca alloy sample, which has more porosity and has a smaller diameter. Bigger pore. The results from XRD had the highest peak in the 89Mg-10Zn-1Ca alloy sample, seen from a crystalline spectrum of 82.4%. The results of the bending test, the most optimal flexural strength occurred in the 89Mg-10Zn-1Ca alloy sample, which was 0.579 Mpa.

Keywords: Powder metallurgy, Mg-Zn-Ca alloys, bone implant

1. Introduction

Biodegradable metals are considered the most superior materials for implant manufacturing. These materials degrade progressively after implementation, preventing the need for postoperative recovery [1]. Due to the acceleration of the human population, the need for orthopedic biomedical devices is also increasing. Among metals, magnesium offers biodegradable and biocompatible properties for use as implants [2].

Magnesium alloys can be selected as bone implants because Young's modulus of elasticity (40-45 GPa) is quite close to that of natural human bone (10-20 GPa) compared to other commonly used materials (stainless steel, titanium and cobalt-chromium-based alloys) [3]. As a result, magnesium can reduce the risk of stress-protective effects during the healing process after implementation caused by a mismatch between the implant and natural bone [4].

Magnesium being an implant means no further surgical procedures need to be performed to remove the implant from the body after the tissue has healed. This advantage can reduce health risks, including human pain and also the cost of surgery. In addition, magnesium plays an important role in the bone healing process, making it more useful for use as a bone implant material [2]. Although magnesium has many advantages as an implant, its use as an implant material has been limited due to its low corrosion resistance, reactivity in electrochemical solutions and rapid dissolution in body fluids [4]. In addition, the mechanical properties of magnesium are also lower than expected for load-bearing applications.

Therefore, alloying elements were selected to improve the basic properties of pure magnesium for further application as medical devices [5]. Zinc (Zn) is an important element for human nutrition after iron. Zn in the human body is found in the kidneys, liver, pancreas, tissues, muscles and bones. Zn element is also one of the best potential materials to improve the mechanical properties and corrosion resistance of Mg alloys [6]. Zn can also improve magnesium alloys' corrosion resistance and mechanical properties. Calcium (Ca) is a major element present in the body and is important in terms of chemical signalling to cells [7] and one of the elements that can control the corrosion rate of Mg. Ca is also a major component in bones that can enhance the healing process

*Corresponding author. Telp: +62823-5337-5042
Jalan Poros Malino, km. 6 Gowa
Sulawesi Selatan, Indonesia
92171

of bone tissue [8]. In addition, the addition of Zn can help reduce the damaging effect of metal impurities, namely Fe and Ni. Therefore, Mg alloys containing Zn are being further demonstrated and developed as promising materials for biomedical applications [9].

One of the magnesium alloys (Mg Alloy) tested is the Mg-Ca-Zn combination which was studied with three variations of Mg-Ca-Zn content. The test results showed that all alloys had no significant side effects on blood cell viability within 24 hours [10]. Magnesium and magnesium alloys also have a low density (1.74 – 2.0 g/cm^3) lower than titanium alloys (4.4 – 4.5 g/cm^3) [11]. For bone replacement applications, Ca is an element that can be used in Mg metal alloys; this is because Ca is the main composition in the human body which can shape the wound healing process [12].

Mg-Zn-Ca alloy is a bio-inert implant material that has been developed recently. The human body has an inherent tolerance for Mg, Zn and Ca [8]. A smelting process is generally used to treat the Mg-Zn-Ca alloy, but in this study, a powder metallurgy process was used [5]. The Mg-Zn-Ca alloy exhibits better mechanical and corrosion properties than pure Mg. However, the Mg-Zn-Ca alloy requires further improvisation to make the implant material biodegradable [1]. Calcium dissolved in the magnesium matrix can soften Mg granules and increase strength without reducing the elasticity of Mg. Adding Ca over 1% by weight can cause a brittle intermetallic phase [13].

2. Materials and Methods

2.1. Material preparation

Pure Magnesium (Mg), Zinc (Zn) and Calcium (Ca) (purity > 98% of each powder) were prepared by powder metallurgy method, with the main material of the powder being magnesium (Mg). Powders of different types or different melting points must be mixed evenly. The Mg-Zn-Ca powder alloy was mixed with the dry milling process for 60 minutes. To get the desired sample, it is necessary to compact the powder in the mold as shown in Fig. 1.

The compaction pressure carried out by the compacting process in Fig. 2 with a load of 200 MPa. The solidification process at room temperature does not have adequate atomic bonding. The Fig. 3 show the sintering process that carried out at a temperature of 500°C and a holding time of 3 hours, and the furnace is supplied with argon gas in the sintering process to prevent oxidation. After sintering, as shown in Fig. 4 the desired sample in the furnace before discharge. The composition of the sample is in Table 1.

Figure 1. Sample mold

Figure 2. 200 Mpa compaction process using Universal Testing Machine

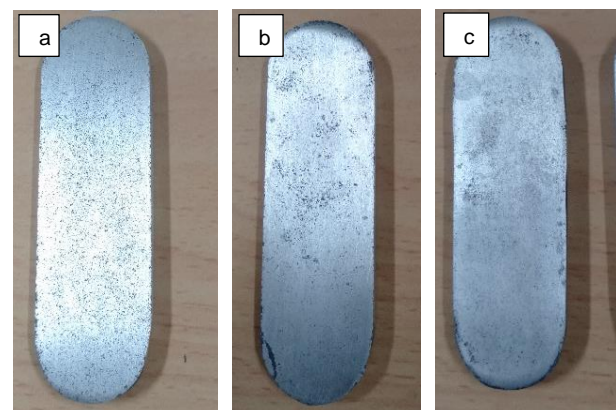Figure 3. The sintering process takes 3 hours with a temperature of 500°C, and the furnace is supplied with argon gas

Figure 4. Mg-Zn-Ca alloy samples with sintering temperature 500°C: (a) 89Mg-10Zn-1Ca, (b) 93Mg-6Zn-1Ca and (c) 97Mg-2Zn-1Ca

Table 1. Sample composition

Sample Code	Weight (%)		
	Mg	Zn	Ca
89Mg-10Zn-1Ca	89	10	1
93Mg-6Zn-1Ca	93	6	1
97Mg-2Zn-1Ca	97	2	1

2.2. Material preparation

The microstructure of the Mg-Zn-Ca alloy was observed using SEM (Scanning electron microscopy), which functions to view or analyze the surface of the Mg-Zn-Ca alloy sample by shooting high-energy electrons at the sample. The JEOL JCM 6000 plus test kit carried out the SEM test. The sample to be tested was previously mounted and sanded the surface until smooth using sandpaper size 3000.

2.3. XRD (X-Ray Diffraction)

XRD (X-Ray Diffraction) analysis was used to determine the phase and degree of crystallinity of the Mg-Zn-Ca alloy, which had been sintered for 3 hours. The XRD tool was used using the Shimadzu 700 XRD test tool.

2.4. Bending test

The bending test was carried out to determine the magnitude of the flexural strength of the Mg-Zn-Ca alloy sample. The bending test used was the three-point bending method, using two supports and one press. The flexure test was carried out using a Universal Testing Machine (UTM) test kit. The manufacture of flexural test samples refers to the JIS R 1601 standard.

3. Results and Discussion

3.1. SEM (Scanning Electron Microscopy) analysis

The SEM results show that, in general, the microstructure of the Mg-Zn-Ca alloy after sintering at 500°C and holding for 3 hours, there is an indication that the porosity of the resulting powder will differ with variations in composition and sintering temperature. Alloy sample 89Mg-10Zn-1Ca (Fig.5a) has less porosity compared to alloy sample 93Mg-6Zn-1Ca (Fig. 5b) and alloy sample 97Mg-2Zn-1Ca (Fig. 5c). The 89Mg-10Zn-1Ca alloy sample has a smaller pore diameter than the 93Mg-6Zn-1Ca and 97Mg-2Zn-1Ca alloy samples with a larger pore diameter.
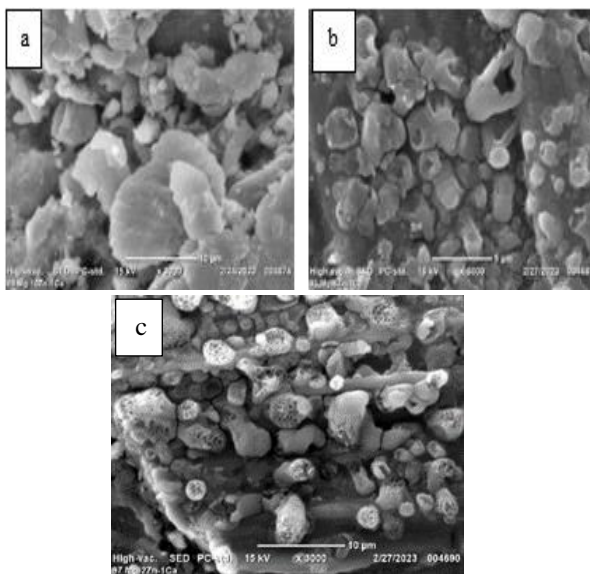

Figure 5. SEM photo magnification of 3000x Mg-Zn-Ca alloy sample sintered at 500°C holding time of sintering 3 hours with the alloy; (a) 89Mg-10Zn-1Ca, (b) 93Mg-6Zn-1Ca and (c) 97Mg-2Zn-1Ca

Adding Ca and Zn elements to Mg alloys can affect the corrosion rate. Adding Zn to Mg alloys can increase the potential for corrosion because Zn has a fairly high electronegativity. Conversely, the presence of Zn can reduce corrosion resistance [8]. It can be seen from the SEM results for each variation of the alloy sample that there is little difference in which the sample has a lumpy or irregular morphological shape. This is caused by grain bonding and particle growth in the hydrothermal and sintering processes [14]. Alloy samples have pores or cavities due to the emergence of pores in the powder metallurgy method, so they cannot be avoided even after the sintering process. These pores or cavities trigger oxidation [15].

Figure 6 shows the cross-sectional results of the Mg-Zn-Ca alloy microstructure with 100x magnification. From Fig. 6, it can be seen that the addition of Zinc (Zn) will give a different microstructure from the alloy. Figure 6 shows that the sintering process of alloy samples can produce porosity due to differences in alloy sizes and melting points. Where magnesium (Mg) has a higher melting point compared to Zinc (Zn): (Magnesium 650°C and Zinc 419°C), so the phenomenon of diffusion and change will be faster if more Zinc (Zn) is added to the alloy. t a sintering temperature of 500°C, the pores formed in alloy sample (a) 89Mg-10Zn-1Ca are fewer than in alloy samples 93Mg-6Zn-1Ca and 97Mg-2Zn-1Ca.

The formation of micropores is also caused by the evaporation of Zinc (Zn) due to the influence of temperature. At the sintering temperature of 600 and 650°C, the temperature is too high for Zinc (Zn), thus forming micropores in the Mg-Zn-Ca alloy.
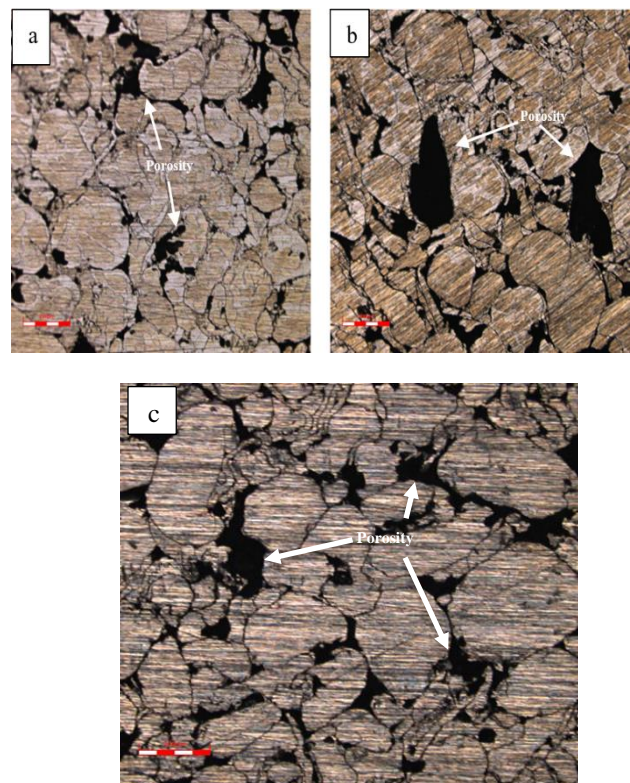

Figure 6. Microstructure photo magnification of 100x Mg-Zn-Ca alloy samples sintered at 500°C holding time of sintering for 3 hours with alloys: (a) 89Mg-10Zn-1Ca, (b) 93Mg-6Zn-1Ca and (c) 97Mg-2Zn-1Ca

For each different composition, the more Mg and Zn reinforcing mixture, the more the spread of the reinforcing powder is seen in the microstructure so that the porosity value is getting smaller [16].

3.2. XRD Analysis

The XRD test in this study was carried out to determine the phases present in the Mg-Zn-Ca alloy, which was sintered at 500°C and held for 3 hours by the powder metallurgy method. Figure 7 shows the diffraction results in the sintering of the Mg-Zn-Ca alloy, where the phases formed have visible differences; the highest peak occurred in the 89Mg-10Zn-1Ca alloy sample seen from a crystalline spectrum of 82.4%. The difference that appears is the peak height of the fraction where the peaks of the Mg phase decrease in each alloy; this indicates more and more bound Zn. The 93Mg-6Zn-1Ca alloy sample has a crystalline spectrum of 78.2%, while the 97Mg-2Zn-1Ca alloy has a crystalline spectrum of 76%.
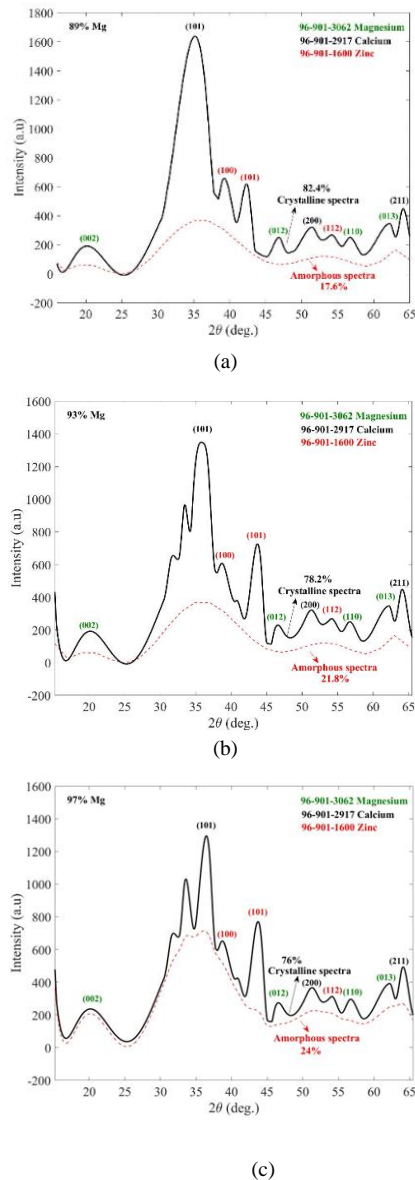

(a)

(b)

(c)

Figure 7. XRD test results for Mg-Zn-Ca alloy sintering temperature 500°C with alloys: (a) 89Mg-10Zn-1Ca, (b) 93Mg-10Zn-1Ca and (c) 97Mg-2Zn-1Ca

This is possible because the more Zn, the porosity decreases due to the densification process, causing the grain surface area to decrease and the reactivity to oxygen to decrease. One of the disadvantages of powder metallurgy is that it has a high surface area, making it reactive to oxidation.

The peaks that appear in the Mg-Zn-Ca alloy samples are areas with Miller indices (002), (102), (100), (101), (012), (200), (112), (110), (013) and (211). Adding Zn powder causes changes in the XRD peaks to become sharper. This is because the more atoms in the order, the better the structure. This indicates the growth of the amorphous phase into a crystalline phase. As a result, the amorphous phase decreased, and the crystalline phase increased, as shown in Figure 7, that the amorphous phase in the 89Mg-10Zn-1Ca alloy sample (Fig.7a) is 17.6%. While the alloy sample 93Mg-6Zn-1Ca (Fig. 7b) has an amorphous phase of 21.8%, and the alloy sample 97Mg-2Zn-1Ca (Fig. 7c) has an amorphous 24%.

The Zn alloy in the Mg-Zn intermetallic phase is a thermally unstable phase with increasing strength and creep resistance properties. The Mg-Zn phase will form intermetallic and will affect the mechanical properties of the Mg alloy, which is known to increase the hardness of the Mg-Zn-Ca alloy [16]. However, this intermetallic phase can also cause galvanic corrosion and brittleness so that, in certain amounts, it can reduce the corrosion rate of Mg alloys.

3.3. Bending test

From the results of the bending test in Fig. 8, the most optimal flexural strength occurred in the 89Mg-10Zn-1Ca alloy sample, which was 0.579 MPa, while the lowest was in the 97Mg-2Zn-1Ca alloy sample, which was 0.506 MPa. From the bending tests that have been carried out, it can be seen in the 89Mg-10Zn-1Ca alloy that the more Zn powder added to the alloy, the more flexural strength properties of the alloy will increase. This means that more Zn powder added to the Mg-Zn-Ca alloy sample can increase the flexural strength of the alloy.

Adding Zn as much as 1-4% by weight to magnesium (Mg) can improve the Mg-Zn-Ca alloy's mechanical properties and corrosion resistance [8]. Figure 8 shows a decrease in the porosity value caused by an increase in the porosity formed in the alloy sample.
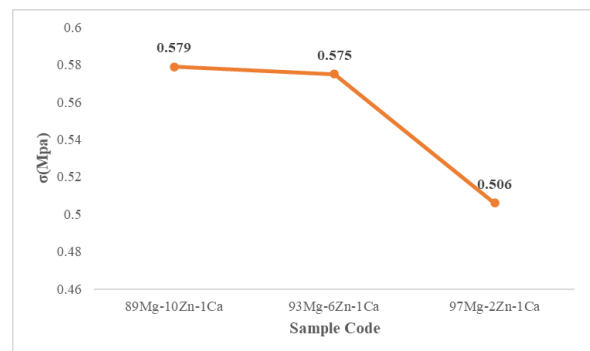

Figure 8. Graph of Mg-Zn-Ca alloy bending test results with the sintering temperature of 500°C

The 89Mg-10Zn-1Ca alloy sample has high flexural strength compared to other alloy samples. The decrease in The decrease in the flexural strength value was caused by the formation of the oxide, in this case, the MgO phase. The MgO, ZnO or CaO phases due to the oxide process formed during sintering can reduce the value of the mechanical strength of the resulting alloy sample [6].

4. Conclusion

a. The SEM results show that the 89Mg-10Zn-1Ca alloy sample has less porosity compared to the 93Mg-6Zn-1Ca alloy sample and the 97Mg-2Zn-1Ca alloy sample. The 89Mg-10Zn-1Ca alloy sample has a smaller pore diameter than the 93Mg-6Zn-1Ca and 97Mg-2Zn-1Ca alloy samples with a larger pore diameter.

b. From the results of diffraction in the sintering of the Mg-Zn-Ca alloy where the phases formed, there are visible differences; the highest peak occurred in the 89Mg-10Zn-1Ca alloy sample seen from a crystalline spectrum of 82.4%. The difference in the peak height of the 93Mg-6Zn-1Ca alloy has a crystalline spectrum of 78.2%, while the 97Mg-2Zn-1Ca alloy has a crystalline spectrum of 76%.

c. From the flexural test results, the most optimal flexural strength occurred in the 89Mg-10Zn-1Ca alloy sample, which was 0.579 MPa, while the lowest was in the 97Mg-2Zn-1Ca alloy sample, which was 0.506 MPa.

References

[1] A. Kumar and P. M. Pandey, "Development of Mg based biomaterial with improved mechanical and degradation properties using powder metallurgy," *J. Magnes. Alloy.*, vol. 8, no. 3, pp. 883–898, 2020, doi: 10.1016/j.jma.2020.02.011.

[2] D. Annur, P. Franciska, A. Erryani, M. I. Amal, L. S. Sitorus, and I. Kartika, "The synthesis and characterization of Mg-Zn-Ca alloy by powder metallurgy process," *AIP Conf. Proc.*, vol. 1725, 2016, doi: 10.1063/1.4945486.

[3] G. Lin *et al.*, "Preparation and characterization of biodegradable Mg-Zn-Ca/MgO nanocomposites for biomedical applications," *Mater. Charact.*, vol. 144, June, pp. 120–130, 2018, doi: 10.1016/j.matchar.2018.06.028.

[4] M. I. Amal, D. Annur, F. P. Lestari, C. Sutowo, and I. Kartika, "Processing of porous Mg-Zn-Ca alloy via powder metallurgy," *AIP Conf. Proc.*, vol. 1778, October, 2016, doi: 10.1063/1.4965744.

[5] D. Annur, F. P. Lestari, A. Erryani, and I. Kartika, "Study of sintering on Mg-Zn-Ca alloy system," *AIP Conf. Proc.*, vol. 1964, May, 2018, doi: 10.1063/1.5038311.

[6] F. P. Lestari, B. A. Saputra, A. Erryani, I. Mulyati, M. S. Dwijaya, and I. Kartika, "Analisis Variasi Temperatur Sintering dan Ukuran Agen Pengembang Dolomit terhadap Fabrikasi Paduan Logam Mg-Ca-Zn Berpori Tertutup dengan Proses Metalurgi Serbuk," *Teknik*, vol. 42, no. 2, pp. 128–136, 2021, doi: 10.14710/teknik.v42i2.36978.

[7] I. Kartika, M. I. Amal, C. Sutowo, S. G. Sukarso, and B. Sriyono, "Pengaruh Variasi Berat Foaming Agent CaH2 terhadap Karakteristik Paduan Mg-Ca-Zn Metal Selular Berbasis Sistem Mg-Zn-CaH2," *Metalurgi*, vol. 29, no. 2, p. 145, 2018, doi: 10.14203/metalurgi.v29i2.286.

[8] A. Erryani, F. P. Lestari, D. Annur, M. I. Amal, and I. Kartika, "Corrotion Rate and Morphology of Porous Metal Alloy Mg-Ca-Zn with CaCO3 as foaming Agent," *Widyariset*, vol. 4, no. 1, p. 9, 2018, doi: 10.14203/widyariset.4.1.2018.9-20.

[9] L. F. Guleryuz, R. Ipek, I. Arltman, and S. Karaoglu, "Effect of Ca and Zn additions on the mechanical properties of Mg produced by powder metallurgy," *AIP Conf. Proc.*, vol. 1809, February, 2017, doi: 10.1063/1.4975434.

[10] A. D. Putra, M. Rohman, and M. Sulaiman, "Simulasi Pengaruh Waktu dan Gerak Terhadap Desain Implan Sendi Pinggul," *J. Pendidik. Tek. Mesin Undiksha*, vol. 9, no. 1, pp. 23–31, 2021, doi: 10.23887/jptm.v9i1.28885.

[11] I. B. Setiawan, D. H. Prajitno, and R. H. Mulyani, "Ketahanan Korosi pada Paduan Mg – 1Mn – HA Sebagai Bahan Biomaterial Hasil Proses Mechanosynthesis dalam Media Ringer Lachtate Corrosion Resistance in Mg-1Mn-Ha Alloy as Biomaterial from Mechanosynthesis Process in Ringer Lachtate Media," *J. Kartika Kim.*, vol. 4, no. 1, pp. 42–50, 2021.

[12] Franciska P. L., D. Annur, I. N. G. P. A., A. Erryani, and I. Kartika, "Proses Sinter Logam Berpori Paduan Magnesium dengan Kalsium Hidrida Sebagai Agen Pengembang," *Semin. Nas. Sains dan Teknol.*, no. November, pp. 1–5, 2017.

[13] I. Kartika, A. M. Ashari, A. Trenggono, F. P. Lestari, and A. Erryani, "Analisis Struktur Pori dan Sifat Mekanik Paduan Mg-0,5Ca-4Zn Hasil Proses Metalurgi Serbuk dengan Variasi Komposisi Foaming Agent CaCO3 dan Temperatur Sintering," *Teknik*, vol. 40, no. 3, p. 142, 2019, doi: 10.14710/teknik.v40i3.25327.

[14] B. Priyono *et al.*, "Sintesis Lithium Titanat Dengan Metode Hidrotermal Dan Efek Suhu Sintering Pada Karakteristik Nanostrukturnya," *J. Sains Mater. Indones.*, vol. 17, no. 1, pp. 1–9, 2015.

[15] R. Hasanah, Aminatun, and D. Hikmawati, "Kajian Transformasi Fasa Sintesis Paduan Kobalt Sebagai Implan Tulang Prosthesis Melalui Metode Metalurgi Serbuk, 2017.

[16] F. P. Lestari, F. Hidayat, A. Erryani, M. Satrio, Y. N. Thaha, and I. Kartika, "Fabrikasi Paduan Magnesium Berpori dengan Partikel Garam NaCl sebagai Space Holder," *Metalurgi*, vol. V, pp. 125–134, 2019.

Study Experimental the Effect of Normalizing Treatment and Galvanic Pack Carburizing Process on Mechanical Properties of Low Carbon Steel

Citra Wahyu Annisa[a],*, Ilyas Renreng[b], Lukmanul Hakim Arma[c], Willian Pian[d]

[a]Department of Mechanical Engineering/Physic Metallurgy Laboratory, Faculty of Engineering, Hasanuddin University.
 Email: citrawahyuannisar@gmail.com
[b]Department of Mechanical Engineering/Physic Metallurgy Laboratory, Faculty of Engineering, Hasanuddin University.
 Email: ilyas.renreng@gmail.com
[c]Department of Mechanical Engineering/Physic Metallurgy Laboratory, Faculty of Engineering, Hasanuddin University.
 Email: armalh@yahoo.com
[d]Department of Mechanical Engineering/Physic Metallurgy Laboratory, Faculty of Engineering, Hasanuddin University.
Email: yuyuncitto@gmail.com

Abstract

Steel is the type of metal most often used in engineering. The purpose of this study was to improve the mechanical properties of mild steel in terms of hardness, ductility, and other mechanical properties and to compare the hardness of carburized steel by galvanic treatment with non-galvanic carburizing of the steel. This research was carried out by varying the heat treatment process, namely carburizing with galvanic heat treatment and carburizing without galvanic, where the carburizing process uses activated carbon coconut shell charcoal with a weight percentage of 80% and 20% of K_2CO_3 (Potassium Carbonate) at a temperature of 900^0C with a holding time of 60 minutes, 120 minutes and 180 minutes. The results obtained from this study indicate that the mechanical properties (hardness) of carbon steel increase at a temperature of 900^0C with a holding time of 1 hour on the galvanic heating method with a better hardness value than the hardness of steel on the non-galvanic method. The hardness value obtained in the galvanic method is 94.06 HRB, while in the non-galvanic method, it is 76.4 HRB and the pearlite phase is formed, resulting in an increased hardness value on the surface of the specimen.

Keywords: Carbon Steel, heat treatment, carburizing, galvanic, hardness

1. Introduction

Steel is a type of metal that is widely used in the engineering field because it has many properties and types so its use can contain several alloying elements. Carbon steel is a Fe alloy steel and the carbon content ranges from 0.3 – 0.17%, where the functions of the carbon as a hardener greatly influence the mechanical properties of the steel [1].

The properties of carbon steel are influenced by the percentage of carbon which greatly influences the mechanical properties, while the microstructure of the steel itself is affected by the heat treatment process [2]. Carbon steel itself can be classified into three parts based on its carbon content including steel with a carbon content of less than 0.3% included in the low carbon steel group, medium carbon steel containing carbon ranging from 0.3 – 0.7%, and steel with high carbon content contains carbon as much as 0.7 – 1.7 carbon [3].

Also, in the manufacturing process, several other chemical elements such as sulfur, phosphorus, silicon, manganese, and other chemical elements are found so that the properties of the steel can be adjusted as needed. The development of industrial technology is very rapid, we often encounter components that experience continuous friction in the process of operation, which can cause components such as gears, pistons, and shafts to experience wear and tear and reduce their service life [4]. To overcome this problem a process is carried out that can increase the hardness of the material, namely by engineering the surface of low-carbon steel which aims to make components that are resistant to friction [1], [4].

This surface engineering process can be carried out using heat treatment methods including normalizing, annealing, hardening, and tempering [2]. The atoms will diffuse into the steel surface through interstitial diffusion where the mechanism of atomic transfer occurs due to the movement of the atoms in the cavity. These atoms experience movement if they have a smaller radius than the parent atom [5] and this carburizing process is also a

*Corresponding Author. Tel.: +62-8521-1696-728
Jalan Poros Malino, km. 6 Gowa,
Sulawesi Selatan, Indonesia
92171

method used to control corrosion that occurs in metals in addition to increasing the hardness of the steel surface [6].

The carburizing process itself is divided into three methods, namely pack carburizing, liquid carburizing, and gas carburizing in this study we used the pack carburizing method or also known as powder/solid carburizing [7]. Galvanic corrosion is also known as dissimilar metal corrosion or bimetallic corrosion, where this process occurs when two different metals or alloys that are in the same environment and are interconnected [8]. Metals with electrode values A higher potential will result in an oxidation or anodic reaction, whereas a metal with a lower potential value will result in a cathodic or reduction reaction on its surface [9]. In this study, two metals with different electrode potential values were used, namely stainless steel and mild steel which would be carburized as shown in Fig. 1.

There have been several previous studies using the pack carburizing method by providing variations on the carburizing and energizer media used, as was done by Asrofi [10], which used mahogany wood charcoal mixed with 20% Barium carbonate ($BaCO_3$) as an energizer, which was carburized at a temperature of 850° C and 900°C with a holding time of 1 hour, which resulted in an increase in the hardness value and the formation of a martensite phase in the material.

Sujita [11] carried out a pack carburizing process at a temperature of 900°C with a holding time of 7 hours using bamboo charcoal as a carburizing medium using an energizer made from beef bone powder, with a resultant increase in hardness value of 110% from the raw material.
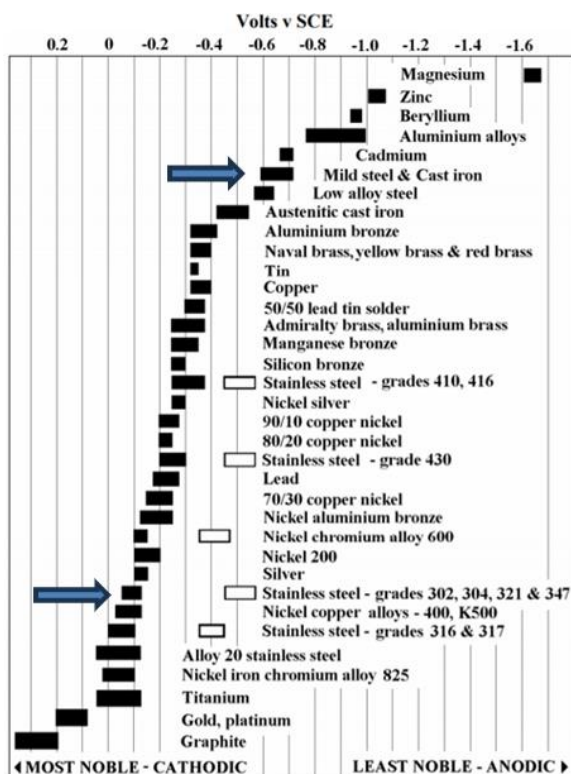
As it is known that the pack carburizing process is a case hardening process which is very dependent on the coefficient of time withholding time and temperature [5].

From some of the studies above, it can be seen that generally, the pack carburizing process is carried out using heat treatment of the material by providing variations on the addition of activated carbon and energizer only without any other treatment. But in this study, it was carried out by giving it a galvanic heating treatment before carburizing. This galvanic treatment is a process in which 2 metals that have different electrode potential values contact each other either directly or by being connected with a salt bridge [12].

2. Experimental Method

2.1. Materials and tools

The tools and materials used in this study are as follows; The tools that will be used in this research are the furnace used during the galvanic heating process and the carburizing pack process, cementation boxes, 250 mesh sieve, thermocouple, hardness test equipment (hardness Rockwell). The materials to be used include steel, charcoal coconut shell, and potassium carbonate (K_2CO_3) which is used as a catalyst.

2.2. Experimental method

Laboratory experiments are carried out by taking data directly on the object to be observed. Recorded directly to get the data needed. The research process was carried out with a procedure starting from the preparation of test specimens with a size (20 x 20 x 10 mm) of 24 pieces, which would be carburized using a ratio of 80% coconut shell charcoal as carbon and mixed with 20% potassium carbonate (K_2CO_3) was used as a catalyst and hardness testing will be carried out to see the increase in the mechanical properties of the low-carbon steel that has been given the treatment.

In this study, the heat treatment process was carried out with variations in the initial heating temperature and galvanic and non-galvanic carburizing pack processes, namely 500°C, 700°C, and 900°C which will be held with variations of 60 minutes, 120 minutes, 180 minutes in the furnace which can be seen in the Fig. 2 where the carburizing galvanic is done by sticking stainless steel and
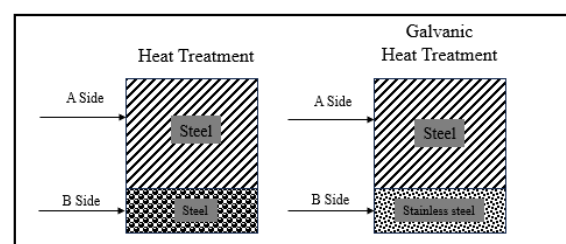
Figure 1. Table of the galvanic series

Figure 2. Heating and galvanic carburizing process

carbon steel specimens into a cementation box that has added carburizing compound in it and then put into a furnace where it will be heated at temperatures of 500°C, 700°C, and 900°C and held for 1 to 3 hours.

3. Results and Discussion

The pack carburizing process is one of the surface hardening processes of low-carbon steel materials by utilizing the diffusion of carbon atoms. With the addition of carbon to steel, the hardness properties will increase by carrying out the galvanic treatment process, and the hardness of the carburizing layer will increase. Adding chemical elements to the carburizing medium will increase the carbon potential which will result in a faster diffusion process and the process of entering the atoms into the steel surface will be deeper [13]. Potassium carbonate will decompose at 900°C into potassium dioxide and produce CO_2 ($K_2CO_3 \rightarrow K_2O + CO_2$). his gas will react with carbon from the carburizing medium to produce CO which then activates carbon atoms to diffuse into the steel surface.

3.1. Hardness test data results

The material surface was tested using Rockwell Hardness, using five points on each sample, with a load (P) of 980 Kg. The increase in the hardness of the carburizing layer was due to the addition of carbon and a structural change from austenite to martensite during the carburizing process. Martensite is the hardest structure with hardness values ranging from 500 – 1000 kg/mm^2 depending on the carbon content.

3.2. Normalizing hardness value

The results of the hardness values obtained with temperature variations of 500°C, 700°C, and 900°C with a holding time of 3 hours can be seen in Table 1.

In Table 1, it can be seen that at temperatures of 500°C and 700°C, there has been no change in the hardness value because the temperature given to the specimen has not reached the critical temperature of the specimen so there has not been a change in mechanical properties, while at a temperature of 900°C, the ministerial hardness value has decreased because at this temperature the specimen has reached the austenite phase and in the austenite phase the

Table 1. Hardness values after normalizing

	Measurement (N)					
	1	2	3	4	5	Average
Raw Materials	**70**	**69.8**	**69.7**	**69.9**	**69.7**	**69.82**
500°C	69.6	69.6	69.4	69.4	69.5	69.5
700°C	69.5	69.5	69.4	69.6	69.4	69.48
900°C	**62.3**	**62.1**	**62**	**62.2**	**62.2**	**62.16**

material undergoes an isothermal transformation into pearlite and ferrite phases due to air cooling so that the hardness of the material decreases[14]. This study proves that heat treatment accompanied by air cooling will cause the hardness value of the material to decrease along with the high temperature of the heat treatment given.

3.3. Hardness data result of pack carburizing specimen

Before carrying out the carburizing process, the usual heating process is carried out first with temperatures of 500°C, 700°C, and 900°C with a holding time of 3 hours. Then the pack carburizing process was carried out at the same temperature with a holding time of 120 minutes.

Table 2 is the hardness value data from the pack carburizing results. From the table, it is clear that the comparison between the different hardness values between normalizing and carburizing where the specimen with the carburizing process is higher than the normalizing temperature of 900°C. The data shows that the carbon atoms of coconut shell charcoal diffuse into the surface of the specimen, causing the carbon present on the surface of the specimen to increase and increase the hardness value of the specimen with the carburizing method carried out.

Table 2. Average hardness values of normalizing and non-galvanic carburizing results

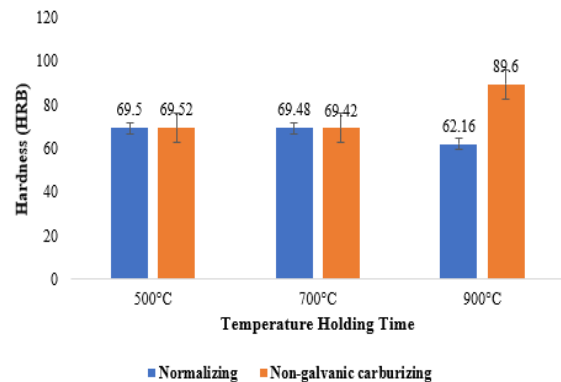| Specimen Treatment	specimen before treatment	Hardness (HRB)		
		500°C	700°C	900°C
Normalizing	**69.84**	69.5	69.48	62.16
Non-galvanic carburizing		69.52	69.42	**89.6**

Figure 3. The average hardness values of normalizing and non-galvanic carburizing results

Table 3. The average hardness values of galvanic carburizing and non-galvanic carburizing

Specimen Treatment	Heating Temperature (°C)		
	500	700	900
Non-Galvanic Carburizing	69.48	69.42	89.46
Galvanic Carburizing	69.42	69.4	90.04

The hardness distribution value that is shown in Fig. 3 where Anwar [15] in his research used coconut shell charcoal that obtained a hardness value of 183 HV (90 HRB).

3.4. Hardness data results of galvanic and non-galvanic carburizing pack

This process is carried out 2 kinds of heat treatment carried out namely galvanic heating and ordinary heating with temperatures of 500°C, 700°C, and 900°C with a holding time of 3 hours and at the same temperature pack carburizing is carried out with a holding time of 120 minutes.

From Table 3, it can be seen that the hardness values between galvanic carburizing and non-galvanic carburizing do not show specific numbers or it can be said that there is no effect experienced by galvanic heating before carburizing. Because at temperatures of 500°C and 700°C, the material and carburizing media have not undergone diffusion because the material has not yet reached the austenite phase where in that phase the material can already experience diffusion so that the carburizing media which has been compounded on the catalyst in the gaseous form will enter the surface of the specimen so that at a temperature of 900°C an increase in the hardness value was obtained [16] as shown in Fig. 4.

3.5. Hardness Data Result of Pack Carburizing at Galvanic 900°C HT Temperature 3 Hours

The temperature of 900°C is used because, in the heat treatment that has been carried out above, a significant change in hardness value is only found at a temperature of 900°C, but in the carburizing process this time the holding time will be varied, namely 30, 30, 120, 180 minutes, while the holding time will be used in the galvanic heating process and the usual heating are used for 3 hours, this is done to further analyze the effect of galvanic heating on pack carburizing.
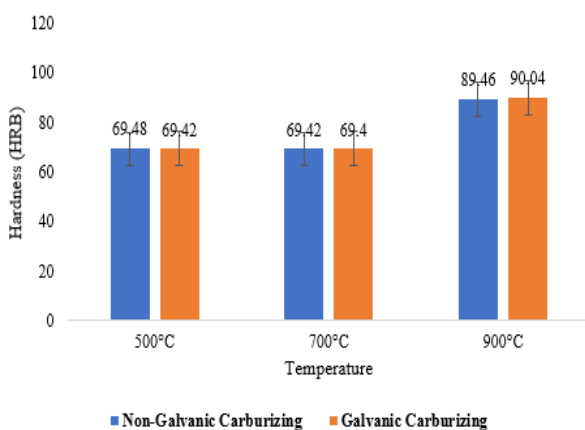

Figure 4. Average hardness values of galvanic and non-galvanic carburizing results

Table 4. Average hardness value data from galvanic heating

No	Holding Time	Galvanic		Non-Galvanic	
		A	B	A	B
1	30 minutes	76.7	74.62	76.4	76.3
2	60 minutes	81.94	75.4	76.16	76.1
3	120 minutes	91.56	91.6	91.54	91.5
4	180 minutes	94.1	94.06	94.02	94.04

Table 4 shows that the results varied at a holding time of 3 hours with a fixed temperature of 900°C. At a holding time of 30 minutes, the average hardness value for the non-galvanic treatment was 76.4 HRB and the average hardness value for the galvanic treatment was 77.3 HRB. In this experiment, it was found that the effect of the pack carburizing treatment which had previously undergone galvanic heating was pack carburizing on the specimen is that there is an uneven distribution of atomic diffusion into the surface of the material.

Furthermore, at a holding time of 60 minutes, the hardness values obtained in the non-galvanic and galvanic treatments were 76.6 HRB and 82.9 HRB from this experiment it can be seen that the effect of the galvanic heating treatment on the carburizing pack gives a high hardness value but this value is only found on the B side of the specimen, while the hardness value obtained on the A side of the specimen is almost the same as the hardness value of the raw material.

In this experiment, the distribution of atomic diffusion was not evenly distributed as in the previous experiment. From the experimental data above can be assumed that the presence of a given galvanic heating treatment will cause cathode and anode areas which cause differences in hardness values and uneven distribution of atomic diffusion in the specimen [9]. So that in the third and fourth experiments, the hardness value of the specimen reached above 90 HRB, and the effect of this galvanic heating treatment has not been experienced by the specimen due to the reconditioning of the specimen. The average hardness value of the non-galvanic in Fig. 5 and galvanic carburizing packs can be seen in Fig. 6.
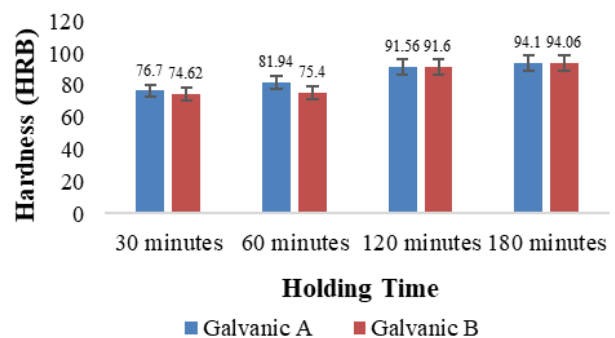

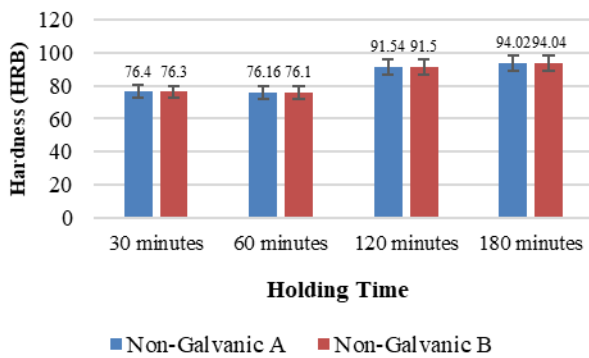Figure 5. Graph of non-galvanic pack carburizing hardness values

Figure 6. Graph of galvanic pack carburizing hardness value

3.6. Result of microstructure observation

Microstructural observation was carried out on HT 60 minutes of pack carburizing specimen with galvanic heating for 3 hours, and non-galvanic pack carburizing at a temperature 900°C as shown in Fig. 7.

Figure 7 shows the result of testing microstructure of the non-galvanic pack carburizing specimen to from dark pearlite and the light ferrite structure. Figure (a) forms fewer pearlite structure than figure (b) on side B, where more pearlite structure is formed than ferrite structures. This pearlite phase causes an increase in the surface hardness value of the specimen with pack carburizing treatment [10]. From the result of microstructural observation, it can be interpreted that the pack carburizing process is going well, in which a pearlite phase is formed, and an increased hardness value is produced on the surface of the specimen [17].
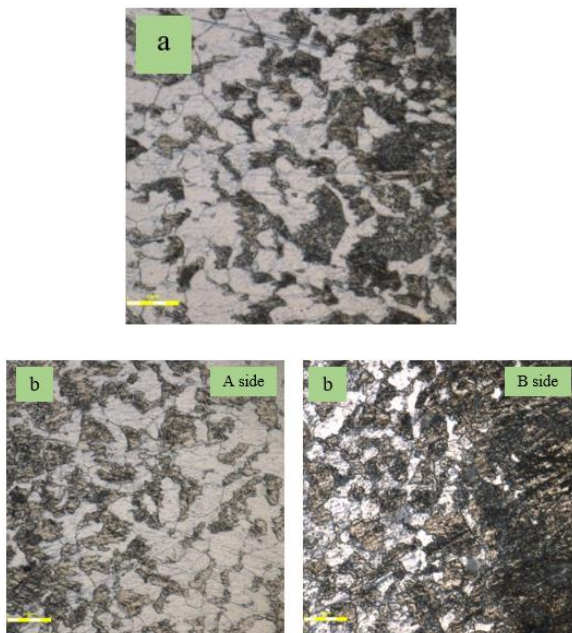

Figure 7. (a) pack carburizing non-galvanic, (b) pack carburizing galvanic

4. Conclusion

Based on the test results and data analysis that has been carried out regarding the effect of heat treatment on low carbon steel after going through the normalizing and heating processes of galvanic carburizing and non-galvanic carburizing, it can be seen that, by carrying out the normalizing and carburizing processes the specimen experienced a decrease in the hardness value of the specimen pack carburizing non-galvanic at a holding time of 30 minutes and 60 minutes at a temperature of 500°C and 700°C, then with galvanic carburizing treatment the specimen will experience a significant increase in hardness at a temperature of 900°C with the highest hardness value obtained in specimens with galvanic carburizing of 94.1 HRB at a holding time of 180 minutes and the lowest was obtained at a holding time of 30 minutes of 74.62 HRB, as shown from the results of the micro structure test where after the galvanic carburizing treatment more pearlite structures were formed which could make the surface of the specimen become harder because the volume of the diffusion rate of carbon increases at a temperature of 900°C, as shown by the increased hardness test results and with the galvanic carburizing process this will improve the mechanical properties of low-carbon steel.

Acknowledgment

References

[1] H. Istiqlaliyah, K. R. H, and M. Baihaqi, "Pengaruh Variasi Media Karburasi Terhadap Kekerasan dan Kedalaman Difusi Karbon Pada Baja ST 42," *Semin. Nas. Inov. Dan Apl. Teknol. Di Ind.*, pp. 138–142, 2016.

[2] S. Rasyid, Y. Mahendra, and R. Hadiana, "Analisis Sifat Mekanik Baja Karbon Rendah Melalui Proses Pack Carburizing (Single Quenching) Menggunakan Arang Sekam Padi dan Barium Karbonat (BaCO3)," pp. 34–39, 2021.

[3] R. E. Smallman and R. J. Bishop, "Ceramics and glasses," *Mod. Phys. Metall. Mater. Eng.*, pp. 320–350, 1999, doi: 10.1016/b978-075064564-5/50010-0.

[4] K. Suarsana, C. I. Putri K, and I. M. Astika, "Pengaruh Perlakuan Temperatur dan Waktu Penahanan Pack Carburizing Terhadap Umur Lelah Baja St 42," *J. Energi Dan Manufaktur*, vol. 11, no. 1, p. 21, 2018, doi: 10.24843/jem.2018.v11.i01.p05.

[5] W. D. Callister and D. G. Rethwisch, *Fundamentals of materials science and engineering : an integrated approach LK - https://tudelft.on.worldcat.org/oclc/798982985*. 2012.

[6] S. A. Sulaiman, S. K. Alias, S. Ahmad, M. H. M. Fauzi, and N. N. Ahmad, "Study on the Effect of Corrosion Behaviour of Stainless Steel before and after Carburizing Heat Treatment," *IOP Conf. Ser. Mater. Sci. Eng.*, vol. 160, no. 1, 2016, doi: 10.1088/1757-899X/160/1/012027.

[7] B. Edenhofer, D. Joritz, M. Rink, and K. Voges, *Carburizing of steels*. Woodhead Publishing Limited, 2015. doi: 10.1533/9780857096524.3.485.

[8] J. Supriadi, I. Pongo, and J. Herdiana, "Pengaruh Korosi Terhadap Plat ST37 Setelah Proses Pengasaman Cuka dan Udara Bebas," vol. 1, no. 1, pp. 12–17, 2020.

[9]   A. Wibowo, "Analisis Sifat Korosi Galvanik Berbagai Plat Logam di Laboratorium Metalurgi Politeknik Negeri Batam," *J. Integr. /*, vol. 144, no. 2, pp. 2085–3858, 2016.

[10] M. Asrofi, M. A. V. Hidayatulloh, G. Jatisukamto, H. Sutjahjono, and R. R. Sakura, "The effect of temperature and volume fraction of mahoni (Swietenia mahogani) wood charcoal on SS400 steel using pack carburizing method: Study of hardness and microstructure characteristics," *AIMS Mater. Sci.*, vol. 7, no. 3, pp. 354–363, 2020, doi: 10.3934/matersci.2020.3.354.

[11] S. Darmo, R. Soenoko, E. Siswanto, and T. D. Widodo, "Study on mechanical properties of pack carburizing SS400 steel with energizer pomacea canalikulata lamarck shell powder," *Int. J. Mech. Eng. Technol.*, vol. 9, no. 5, pp. 14–23, 2018, doi: 10.30574/gjeta.2022.11.2.0087.

[12] A. F. Abidah, "Analisa SS400 Hasil Carburizing Media Arang Tempurung Kelapa-BaCO3 dengan Variasi Temperatur Pemanasan dan Holding Time Ditinjau dari Pengujian Kekerasan dan Struktur Mikro," *Jtm*, vol. 07, no. 02, pp. 1–8, 2019.

[13] D. N. K. Putra Negara, I. D. M. K. Muku, I. K. G. Sugita, I. M. Astika, I. W. Mustika, and D. G. R. Prasetya, "Hardness Distribution and Effective Case Depth of Low Carbon Steel after Pack Carburizing Process under Different Carburizer," *Appl. Mech. Mater.*, vol. 776, pp. 201–207, 2015, doi: 10.4028/www.scientific.net/amm.776.201.

[14] I. M. S *et al.*, "Simulasi Efek Galvanik pada Baja Karbon Sedang Hasil Perlakuan Panas Menggunakan Boundary Element Method (BEM) -3D," vol. 7, no. Juni, pp. 3–6, 2019.

[15] A. Nurharyanto, D. A. Halim, and E. Surojo, "Perbandingan Nilai Kekerasan Baja Karbon Rendah pada Proses Pack Carburizing dengan Media Arang Sekam Padi dan Arang Tempurung Kelapa," *Tek. J. Sains dan Teknol.*, vol. 15, no. 1, p. 39, 2019, doi: 10.36055/tjst.v15i1.6009.

[16] K. Madu and A. E. Uyaelumuo, "Parametric Effects of Carburization Time and Temperature on the Mechanical Properties of Carburized Mild Steel," *SSRN Electron. J.*, 2018, doi: 10.2139/ssrn.3209937.

[17] U. L. Reza Hadi Pratama, Priyagung H, "Analisis Kekerasan dan Strukur Mikro pada Baja A36 dengan Proses Carburizing Menggunakan Batubara," pp. 36–43, 2022.

The Export Potential of Mining Commodities of Indonesia

Rini Novrianti Sutardjo Tui[a,*], Aryanti Virtanti Anas[b], Rizki Amalia[c], Tsuyoshi Adachi[d]

[a]Department of Mining Engineering, Faculty of Engineering, Universitas Hasanuddin. Email: rini@unhas.ac.id
[b]Department of Mining Engineering, Faculty of Engineering, Universitas Hasanuddin. Email: aryantiv@unhas.ac.id
[c]Department of Mining Engineering, Faculty of Engineering, Universitas Hasanuddin. Email: rizkiamalia@unhas.ac.id
[d]Department of Geosciences, Geotechnology, and Material Engineering for Resources, Graduate School of International Resource Science,
Akita University. Email: adachi.t@gipc.akita-u.ac.jp

Abstract

The implementation of the export ban on raw mineral commodities is one of the implications brought by the Mining Law Number 3 of the year 2020 set by the government of Indonesia. The high contribution of the raw mining commodities towards the economy of Indonesia plays dual sides of a coin. First, it is seemingly more beneficial to increase the value of the raw commodities by processing and refining them first domestically. Then, as the raw commodities contribute largely, banning the export surely will bring a change towards the economy. Change in the government's regime initiated the review of the export ban. This research utilizes the Herfindahl Hirschman (HH) Index and Revealed Comparative Advantage (RCA) to investigate how export bans can affect economic growth. In analyzing the impact of the export ban, the very basic foundation is examining the export potential of the mining commodities. Analyzing the ores, metals, and minerals as export commodities, the ores and minerals seemingly are the prominent export commodities. As proved by the RCA index value, the government of Indonesia has a strong foundation for releasing the export ban. Additionally, the HH Index of market concentration indicates that the export trade of Indonesia is relatively independent towards its trading partner. Therefore, as the government of Indonesia sets to implement the export ban policy, this change in trade barriers is unlikely to disrupt the trade relations between Indonesia and its trading partners.

Keywords: Export ban; export concentration; export penetration; mineral commodities

1. Introduction

As Indonesia is facing a change in regime in the year 2024, it is the appropriate time to review the further implementation of the mining commodities export ban. The export ban of the raw mineral commodities is released as a form of export restriction acts as government intervention towards the Indonesia's trade of commodities. Implementing the export ban faces potential loss in export revenue, and export revenue volatility is strongly linked to growth volatility [1], so significant fluctuations in export earnings result in fluctuations in economic growth. Further, losses in export revenues and growth slowdown reflect how an economy may be vulnerable to external economic shocks, but the scale of impact depends largely on the degree of concentration of a country's export portfolio. Despite how resource abundance can positively affect growth, export concentration in resources hurts growth [2]. Therefore, in order to determine how export ban can affect the economy growth, it is necessary to investigate the mining export concentration.

*Corresponding author. Tel.: +62 852 5656 8238
Faculty of Engineering Campus, Universitas Hasanuddin
Gowa Regency, South Sulawesi
Indonesia, 92171

1.1. Literature review

A country's export portfolio represents the diversification of its exports. This diversification makes the country less vulnerable to adverse terms of trade shocks by stabilizing export revenues [3]. The issue is not that exports are concentrated but that they are usually concentrated on homogeneous products. These individual exporting countries are facing a highly inelastic demand curve such that changes in global supply are translated into significant price volatility, and when these countries are low-income countries, they are often suffering terms of trade shocks that adversely affect investment and even consumption [4], [5]. As vulnerability of a country to the economic shocks indicates the dependence of the country to its export, another tool to determine mining export dependence is by measure the export value as percentage of the GDP (Gross Domestic Product) [6].

1.2. Herfindahl Hirschman (HH) index

The degree of export concentration partially can be analyzed using Herfindahl Hirschman (HH) Index and the revealed comparative advantage (RCA) index. Herfindahl Hirschman (HH) Index is originally developed based on trade partner concentration as an indicator of national

Table 1. Concentration level based on HH Index value ([9])

HH Index Value	Concentration Level
< 0.01	Perfect equality
0.01 – 0.15	Low
0.15 – 0.25	Moderate
> 0.25	High

economic and political vulnerability. Basically, this index can be used to measure various contexts of concentration. This index has been prominently used in the context of export concentration, for example when analyzing export partners [7], [8], and when assessing the export concentration for developed, developing, and transition countries [9]. The index is calculated as:

$$HH_{ij} = \frac{x_{ij}/X_{it}}{x_{wj}/X_{wt}} \dots\dots\dots\dots\dots\dots\dots\dots\dots (1)$$

Where x_{ij} and x_{wj} are the values of country i's exports of product j and world exports of product j and where X_{it} and X_{wt} refer to the country's total exports and world total exports. The result of the calculated values of HH Index can be classified as shown in Table 1.

1.3. Revealed Comparative Advantage (RCA)

Another useful tool for analyzing export concentration is the index of revealed comparative advantage (RCA). The RCA Index is originally based on trade flows. The concept of RCA is that a country holds the ability to produce some trade goods or services with higher productivity as well as higher product differentiation than other producing countries in a trade area [10]. The assumption used is that the trade flows can reveal the comparative advantage of the product that is being traded between two entities. Basically, the RCA Index is equal to the proportion of the country's exports divided by the proportion of world exports [11]. A country is said to have a revealed competitive advantage for a commodity or an industry when the RCA Index is > 1.

2. Mining Commodities Export Values

A comparison of the GDP (Gross Domestic Product) value with the total natural resource rent and industry
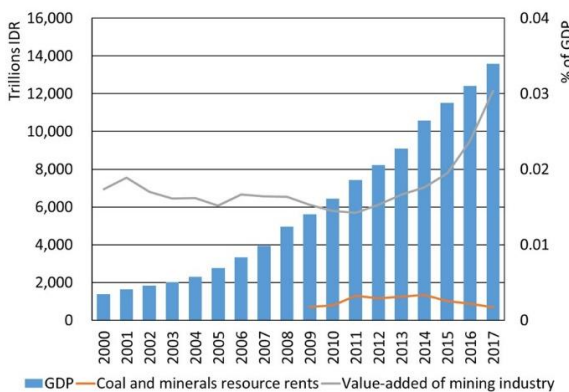

Figure 1. Comparison of Indonesia's GDP, coal and mineral resource rent, and industry value added (calculated from [12] and [13])
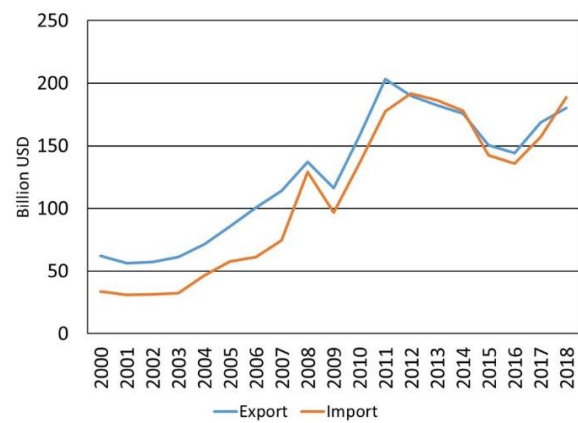

Figure 2. Indonesia's export and import value of the year 2000 – 2018 ([14])

value added, both of which are calculated as a percentage of the GDP, is necessary in analyzing how much Indonesia relies on its natural resources. The mining resource rent includes mining product sales, royalties, and fixed fees. The industry value added includes value added from coal, fossil fuel, nuclear fuel, metals, non-metals, and processed metals. The comparison is shown in Figure 1.

The next step is assessing the value of international trade, as Indonesia is a country that relies largely on its exports. Figure 2 shows both the export and import values. On average, between the years 2000 to 2018, the export value is USD 127 billion, compared to the average import value of USD 110 billion.

Our findings show that the export of raw mining commodities accounts for a large part of Indonesia's exports. The high contribution of raw mining commodities plays a dual role in the coin. First, it is seemingly more beneficial to increase the value of the raw commodities by processing and refining them first domestically. Then, as raw commodities contribute largely, banning exports will surely bring a change to the economy. Therefore, it is important to assess the potential impacts that the export ban will have on Indonesia's economy.

The export ban policy has been determined as indeed a resource nationalist policy, and as a resource nationalist policy, the export ban is deemed beneficial, and therefore, it gains huge public support. As the policy was released, the people and the government of Indonesia presumed that this policy was definitely profitable for the nation. This study is among the first few analyses conducted to academically and empirically prove the potential benefit of the export ban, if any.

3. Export Penetration of Mining Commodities

The next step is examining the export market penetration. This market penetration measures the extent to which a country's exports reach already-proven markets. It is calculated as the number of destination countries to which the exporting country exports a particular product divided by the number of countries that the exporting country imports the product that year. Figure 3 shows that from 2000 to 2018, the market penetration index of Indonesia, on average, was 13.02. Compared to
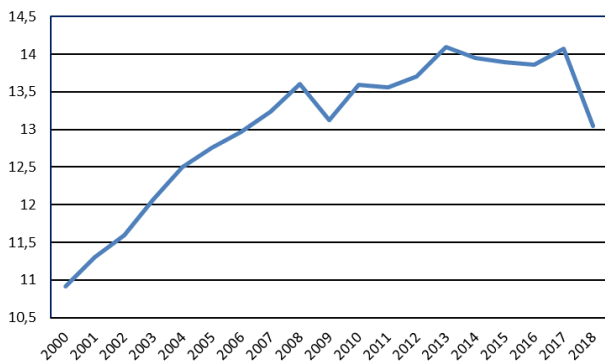
Figure 3. Indonesia's export market penetration index

the world's average market penetration index of 83.37, Indonesia's value is considered relatively low.

Then, using the HH Index, the market portfolio of the exports of Indonesia is examined. The HH Index measures the dispersion of trade value across an exporter's partners. A country with a preponderance of trade value concentrated in very few markets will have an index value close to 1.

Figure 4 shows the change in the HH Index for Indonesia from the year 2000 to 2018. Apparently, the HH Index is in a decreasing trend, indicating that through the years, Indonesia has grown independent from its trading partners.

4. Export Concentration of Mining Commodities

One of the components that contributes to the export value is the export of raw materials. Data from the World Integrated Trade Solution shown in Figure 5 shows that the average share of raw materials exported is 26%. This value highlights the contribution of the export of raw materials to the economy of Indonesia.

Assessing the potential economic impact of the export ban, a calculation of the revealed comparative advantage (RCA) index is needed. The focus of this study is particularly on mineral commodities, and ore and metals commodities. The revealed comparative advantage index indicates whether a country is in the process of extending the products in which it has a trade potential, as opposed to situations in which the number of products that can be competitively exported is static. Comparing the comparative advantage indexes of the commodities against the world trade is carried out using the WITS software provided by the World Bank.
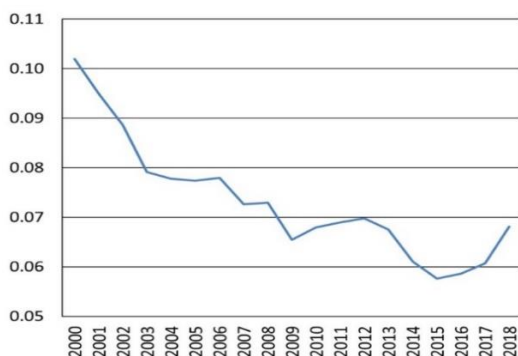

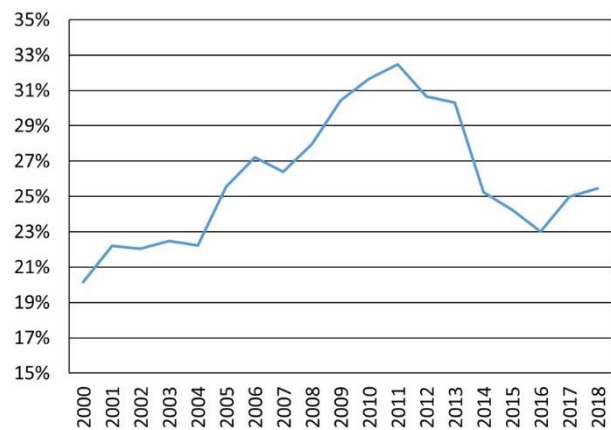Figure 4. HH market concentration index for Indonesia 2000 – 2018

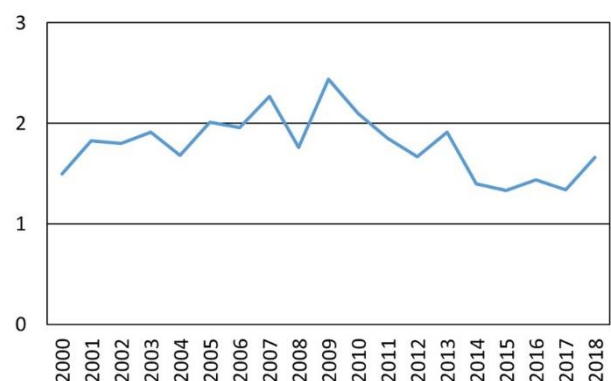Figure 5. Indonesia's raw materials export share of the years 2000 – 2018 ([14])

Figure 6. RCA Index for Indonesia's ore and metal commodities against the world value

Figure 6 shows that despite the volatility, the ore and metal commodities of Indonesia evidently have a revealed comparative advantage. On average, during the period of 2000 to 2018, the RCA Index value for the ore and metal commodities is 1.8. The RCA Index value indicates that the release of the export ban does not affect Indonesia's position as a competitive producer and exporter of ore and metal commodities.

In analyzing the impact of the export ban, the very basic foundation is examining the export potential of the mining commodities. Analyzing the ores, metals, and minerals as export commodities, the ores and minerals seemingly are the prominent export commodities. Proved by the RCA index value, the government of Indonesia has a strong foundation to release the export ban. Additionally, the HH Index of market concentration indicates that the export trade of Indonesia is relatively independent towards its trading partner. Therefore, as the government of Indonesia sets to implement the export ban policy, this change in trade barriers is unlikely will disrupt the trade relations between Indonesia and its trading partners.

5. Conclusions

In analyzing the impact of the export ban, the very basic foundation is examining the export potential of the mining commodities. Analyzing the ores, metals, and minerals as export commodities, the ores and minerals seemingly are

the prominent export commodities. As proved by the RCA index value, the government of Indonesia has a strong foundation for releasing the export ban. Additionally, the HH Index of market concentration indicates that the export trade of Indonesia is relatively independent of its trading partner. Therefore, as the government of Indonesia sets to implement the export ban policy, this change in trade barriers is unlikely to disrupt the trade relations between Indonesia and its trading partners.

Acknowledgments

References

[1] United Nations Development Programme, "Export Dependence and Export Concentration," in *Towards Human Resilience: Sustaining MDG Progress in an Age of Economic Uncertainty*, New York: UNDP Bureau for Development Policy, 2011.

[2] D. Lederman and W. F. Maloney, "Trade Structure and Growth," Washington, DC, 3025, 2003.

[3] A. R. Ghosh and J. D. Ostry, "Export Instability and the External Balance in Developing Countries," *IMF Staff Pap.*, vol. 41, no. 2, pp. 214–235, 1994.

[4] M. Jansen, "Income Volatility in Small and Developing Economies: Export Concentration Matters," Geneva, 2004.

[5] P. Brenton, R. Newfarmer, and P. Walkenhorst, "Export Diversification: A Policy Portofolio Approach," Washington, DC, 2007.

[6] J. Butkiewicz and H. Yanikkaya, "Minerals, Institutions, Openness, and Growth: An Empirical Analysis," *Land Econ.*, vol. 86, no. 2, pp. 313–328, 2010.

[7] J. Kentor and T. Boswell, "Foreign Capital Dependence and Development: A New Direction," *Am. Sociol. Rev.*, vol. 68, no. 2, p. 301, 2003.

[8] S. Babones and R. M. Farabee-Siers, "Indices of Trade Partner Concentration for 183 Countries, 1980-2008," *J. World-Systems Res.*, vol. 18, no. 2, pp. 266–277, 2012.

[9] K. Dumičić, H. Jošić, and B. Žmuk, "Investigating Export Market Concentration for Developed, Developing and Transition Countries," *Int. J. - Vallis Aurea*, vol. 4, no. 1, pp. 5–28, 2018.

[10] R. Stellian and J. Danna-Buitrago, "Revealed Comparative Advantages and Regional Specialization: Evidence from Colombia in the Pacific Alliance," *J. Appl. Econ.*, vol. 22, no. 1, pp. 349–379, 2019.

[11] D. Granabetter, "Revealed Comparative Advantage Index: An Analysis of Export Trade in the Austrian District of Burgenland," *Rev. Innov. Compet. A J. Econ. Soc. Res.*, vol. 2, no. 2, pp. 97–114, 2016.

[12] Badan Pusat Statistik, "Gross Domestic Product Based on Current Prices According to Business Sectors," Jakarta, 2019.

[13] Direktorat Jenderal Mineral dan Batubara, "Minerba dalam Angka Tahun 2011 - 2016," Jakarta, 2017.

[14] World Integrated Trade Solution, "Indonesia's Export and Import Value of The Year 2000 - 2018," 2020.